IN-26
135696
190 P

NASA Contractor Report 182113

Processing, Physical Metallurgy and Creep of NiAl + Ta and NiAl + Nb Alloys

(NASA-CR-182113) PROCESSING, PHYSICAL METALLURGY AND CREEP OF NiAl + Ta AND NiAl + Nb ALLOYS Ph.D. Thesis. Final Contractor Report (Case Western Reserve Univ.) 190 p CSCL 11F G3/26

N88-21295

Unclas
0135696

Viren M. Pathare
Case Western Reserve University
Cleveland, Ohio

April 1988

Prepared for
Lewis Research Center
Under Grant NAG3-387

National Aeronautics and
Space Administration

Acknowledgements

My first and foremost thanks go to my thesis advisor Professor K. M. Vedula who has constantly given me guidance and encouragement, not only on technical matters but life as well. His advice on P/M processing, mechanical testing and the overall direction of the thesis was very helpful. Professor G. M. Michal, who is a co-advisor for this dissertation, is to be thanked sincerely for his guidance on physical metallurgy, TEM and x-ray analysis.

The project was sponsored by NASA Lewis Research Center in Cleveland, OH, under the supervision of Drs. J. R. Stephens and M. V. Nathal. I am thankful to them for making NASA facilities available to me and for their advice about the general direction of the work. I had many fruitful discussions with Dr. J. D. Whittenberger who also did most of the slow compression testing. Sincere thanks are due to him. During the course of this work nearly fifty alloys were extruded. D. J. Gaydosh and his team is thanked for doing the extrusions. Metallographic preperation of these brittle intermetallics

is a challenge in itself. T. A. Leonhard and W. D. McCort are thanked for this painstaking job. J. G. Wagner is thanked for analyzing several DTA samples at a short notice. R. G. Garlick is thanked for his help in the x-ray analysis. S. L. Draper and D. R. Hull are thanked for their help with the SEM at NASA.

The cast alloy was supplied by Dr. Ram Darolia of General Electric, Cincinnati, Ohio.

The list of people to be thanked at Case is equally long. J. Sears and S. Short are thanked for their help with the TEM facilities at Case. Drs. A. Ruiz, P. Lagerlof, V. Lanteri and M. Crimp are thanked for their help in the analysis of TEM micrographs. A. Biswas is thanked for making sense out of VAX. R. Dickerson is thanked for repairing broken instruments.

Table of Contents

1. Introduction.....1

1.1 Intermetallic compounds.....1
1.2 NiAl and its alloys.....2
1.3 Scope of the thesis.....3

2. Processing.....6

2.1 Literature Survey.....6

2.2 Processing of NiAl Based Ternary Alloys.....7

2.2.1 Hot Extrusion of Blended Powders (NiAl+2at.%Ta and NiAl+2at.%Nb Alloys).....7
2.2.2 Hot Extrusion of NiAl + 1 at.% Ta or Nb Alloys.....8
2.2.3 NiAl+4.5at.%Ta Alloy.....10
2.2.4 Vacuum Hot Pressing of NiAl+4.5at.%Ta Powder.....10
2.2.5 Cast NiAl+5at.% Alloy.....11

2.3 Chemical Analysis.....12

3. Physical Metallurgy.....29

3.1 Introduction.....29

3.2 Literature Survey.....30

3.3 Experimental Techniques.....32

3.3.1 Optical Microscopy and Scanning Electron Microscopy.....32
3.3.2 Differential Thermal Analysis (DTA).....33
3.3.3 X-ray Analysis.....35
3.3.3.1 Equipment.....35
3.3.3.2 Computer Analysis of Data.....35
3.3.4 Transmission Electron Microscopy 37

3.4 Results and Discussion.....38

3.4.1 NiAl+1at.%Ta and NiAl+1at.%Nb Alloys.....38
3.4.2 NiAl+2at.%Ta Alloy.....39
3.4.2.1 Analysis.....39
3.4.4 NiAl+4.5at.%Ta Alloy.....44
3.4.4.1 Analysis of the Unknown Phase in NiAl+4.5at.%Ta Alloy.....47

3.4.4.1.1 Chemistry.....47
3.4.4.1.2 Electron Diffraction.....49
3.4.4.1.3 X-ray Diffraction.....51

3.5 Grain Growth.....52

3.5.1 Theory of Grain Growth.....52
3.5.2 Secondary Recrystallization.....53
3.5.3 NiAl+1at.%Ta.....54
3.5.4 NiAl+1at.%Ta with Sieved Powder.....55
3.5.5 NiAl+4.5at.%Ta.....56

4. Creep.....100

4.1 Literature Review.....100

4.1.1 Diffusion Creep 100
4.1.2 Power Law Creep.....101
4.1.4 Creep of Polycrystalline NiAl.....105

4.2 Experimental Procedure.....106

4.2.1 Compression Creep.....106
4.2.2 Slow Compression Test.....108
4.2.3 On the Equivalency of Compression Creep and Slow Compression Tests 109

4.3 Results.....110

4.3.1 NiAl.....110
4.3.2 NiAl+1at.%Ta and NiAl+1at.%Nb.....111
4.3.3 NiAl+2at.%Ta and NiAl+2at.%Nb.....114
4.3.4 NiAl+4.5at.%Ta.....115
4.3.5 Effect of Heat Treatment.....116
4.3.6 NiAl+5at.%Ta Cast Alloy.....117

4.4 Discussion.....117

5. Conclusions.....149

5.1 Processing.....149

5.2 Physical Metallurgy.....150

5.3 Creep.....151

6. References.....153

7. Appendix I.....156

8. Appendix II.....165

1. Introduction

1.1 Intermetallic compounds

Intermetallic compounds (intermetallic phases or shortly intermetallics) are solid solutions or compounds of two or more metals with crystal structures that are different from those of the respective pure components [Cottrell (1967)]. The principal characteristics of the intermetallic compounds were discovered very early: their brittleness, high hardness relative to their components, occurrence at specific atomic ratios, and their ability in certain instances to dissolve appreciable amounts of their components and thus exist over an extended composition range.

The intermetallic compounds are of interest for high temperature applications because of their outstanding high temperature stability which results from the strong bonding between their constituent atoms. This is illustrated by B2 NiAl which has a higher melting point than nickel or aluminum. Intermetallic compounds are also known to have high strength at high fractions of their melting point. Diffusion is believed to be inherently difficult in these ordered alloys. Because of these and

many other attractive properties there has been a revival of interest in developing high temperature materials based on intermetallic compounds. Excellent reviews of current literature on the main characteristics of these materials, the past and present developments and the further prospects are presented by Stoloff (1985) and Sauthoff (1986).

1.2 NiAl and its alloys

Among the intermetallic compounds, one of the most interesting as a potential new high temperature structural material is NiAl. At the stoichiometric composition NiAl has a fully ordered CsCl type (B2) crystal structure upto its congruent melting temperature of 1911°K [Bradley and Taylor (1937)]. It is stable over a wide range of compositions extending from 41.5 to 55 at.% aluminum at room temperature (Figure 1.1). The density of NiAl (5.9 g/cc) is much lower than those of the existing high temperature alloys which have densities as high as 8-9 g/cc. In addition to the high melting point and low density, NiAl forms a hard, electrically resistive Al_2O_3 film that is more protective than the oxidation products on superalloys at elevated temperatures [Pettit (1967) and Doychak (1984)]. This

temperature range suggested by the oxidation resistance, is characterized by creep as the deformation mechanism. However, it was found that NiAl shows poor creep resistance in the unalloyed state relative to that of commercial nickel based superalloys [Stoloff (1985)].

A program was sponsored by the NASA Lewis Research Center, Cleveland, Ohio to develop alloys based on NiAl with improved creep resistance. Selected ternary additions to NiAl at a level of 2-5 at.% were shown to improve compressive creep strength at 1300°K [Pathare (1985), Pathare et al (1984)]. Alloys containing titanium, copper, manganese and iron are solid solution alloys of NiAl at the given level of addition and show a moderate increase in creep strength over NiAl. Ternary additions that form a second phase in the matrix, viz. tantalum, halfnium, tungsten, molybdenum, rhenium and niobium lowered the steady state creep rate of NiAl by orders of magnitude. Alloys containing niobium, halfnium and tantalum showed creep rates comparable to those of commercial wrought superalloys.

1.3 Scope of the thesis

Niobium and tantalum were chosen to be studied in

detail as additions to NiAl because of their promise. Tantalum addition is of more interest as it showed better creep properties between the two. Having selected the ternary additions the main objectives of this study were:

(i) To develop processing routes to obtain 100% dense materials. To develop extrusion parameters, hot pressing parameters for these new alloys.

(ii) To understand the physical metallurgy of these alloys. To identify the phases present at various temperatures. To identify the phase transformations taking place.

(iii) To document the creep properties and compare them with binary NiAl. To explain the improvements in creep properties in terms of the exhisting creep theories.

The next three chapters are devoted to the three key issues in this program: processing, physical metallurgy and creep. They are complete units; each chapter contains its own literature survey, experimental procedure, results and discussion. They are followed by a chapter on conclusions reached at the end of this research program.

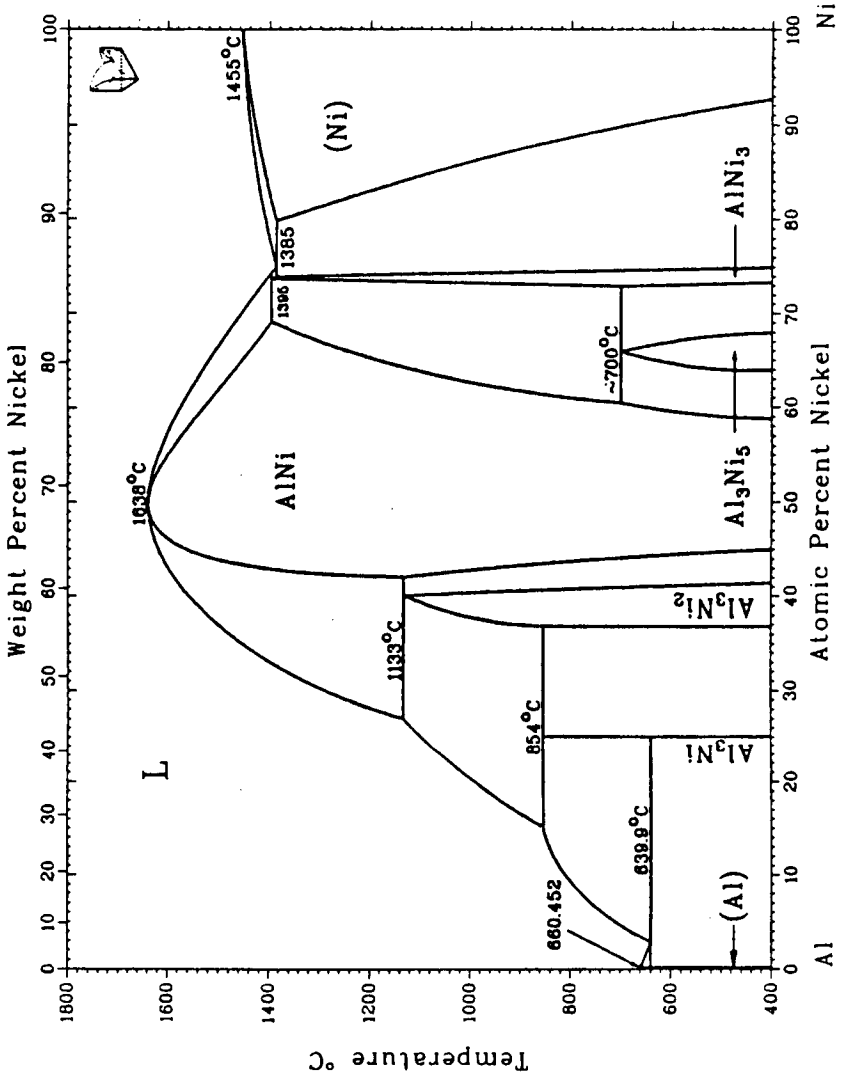

Figure 1.1 Ni-Al phase diagram [Singleton et al (1986).

2. Processing

2.1 Literature Survey

Table 2.1 shows various processing methods used for alloys based on NiAl. This is not a complete list. However, it shows the general trends. In the 1960's and before, almost all NiAl alloys were cast. In the 1970's, there were some which were cast and then extruded. Powder processed alloys appear only in the 1980's.

NiAl powder always has an oxide layer, presumably Al_2O_3, which needs to be disrupted in order to get a complete bonding between particles. Hot extrusion of powders offers a unique way of using the frictional force between the particles to shear the powder particles. Whittenberger (1987a) at NASA Lewis Research Center, Cleveland, OH, has successfully developed the parameters for hot extrusion of binary NiAl powders. Pathare et al (1985) have used hot isostatic pressing and hot extrusion to consolidate NiAl and NiAl with some ternary additions. There is no example of vacuum hot pressing of NiAl powders in the literature.

Baker and Schulson (1984) have characterized the

deformation structure of Ni-rich NiAl extruded at 823°K by TEM and optical microscopy. They observed **b**<100> dislocations in complex networks, tangles and prismatic loops. **b**<110> dislocations, which were rare, were present due to reactions of **b**<100> dislocations. Recovery and recrystallization had taken place in the extruded material. Extrusion was deemed to have been possible by the operation of {hk0}<001> slip systems (often in plane strain flow) plus diffusion assisted processes.

Lloyd and Loretto (1970) have also performed similar analysis. They have, however, not reported the temperature of extrusion. They concluded that in addition to **b**<100> dislocations, **b**<110> and **b**<111> dislocations contribute to the deformation during deformation.

2.2 Processing of NiAl Based Ternary Alloys

2.2.1 Hot Extrusion of Blended Powders (NiAl+2at.%Ta and NiAl+2at.%Nb Alloys)

Alloys containing 2 at.% tantalum or niobium were prepared from blended powders. -100 mesh (<150 μm) NiAl powder was blended with appropriate amounts of -325 mesh (<45 μm) tantalum or niobium powder for 2 hours in a vee-blender. The blended powders were packed in cylindrical

mild steel can (51 mm diameter X 127 mm long X 6.4 mm wall thickness); evacuated and sealed (Figure 2.1). The cans were then extruded at 1400°K using a 16:1 reduction ratio. Figure 2.2 shows the typical microstructure of an as extruded NiAl+2at.%Ta alloy. The white elongated phase is tantalum rich. Direction of extrusion is clear from the elongated second phase and oxide stringers. The grains were equiaxed, suggesting that recrystallization had taken place. Extrusion is deemed to have been possible by the flow of NiAl around tantalum rich areas. A similar structure was observed for NiAl+2at.%Nb alloys.

After extrusion the cans were removed by leaching in HNO_3. An homogenization anneal at 1623°K for 100 hours was given in order to achieve uniform distribution of tantalum or niobium into NiAl matrix. No pure tantalum or niobium was found in the alloys after the homogenization. But the distribution of second phases was quite non-uniform.

2.2.2 Hot Extrusion of NiAl + 1 at.% Ta or Nb Alloys

Since these powders were obtained in the prealloyed form from Alloy Metals Inc., MI, there was no need for blending. Internal structure of the powders can be seen in Figure 2.3. The interdendritic region is richer in the ternary addition and hence looks brighter in the back

scattered electron image. The cell size for both powders was about 5 μm.

It was proposed to hot-extrude the powders first with 8:1 ratio at 1300°K and then re-extrude the solids with 6:1 ratio at 1073°K and 1350°K in order to obtain different grain sizes. The extrusion parameters are listed in Table 2.2. Extrusions with 8:1 reduction ratio were successful, giving a 100% dense material of recrystallized grain size of 7 μm for NiAl+1at.%Nb and 9 μm for NiAl+1at.%Ta. However attempts of re-extrusion with 6:1 ratio did not succeed. The unsuccessful extrusions could be classified into two catagories:

i. No material came through the die
ii. Can material (mild steel) come through the die with unconsolidated chunks of intermetallic. This is illustrated in Figure 2.4.

Prealloyed powders of NiAl+1at.%Ta and NiAl+1at.%Nb were, however, successfully extruded at 1400°K with 16:1 reduction ratio. Figure 2.5 shows the typical microstructure of an extruded alloy. After the extrusion 50 mm long pieces were cut on a high speed saw. The cans were removed by centerless grinding. Cylindrical specimens were used for creep properties evaluation.

2.2.3 NiAl+4.5at.%Ta Alloy

Prealloyed powder of this composition was bought from Alloy Metals, MI. The intended composition was NiAl+3at.%Ta, but due to the difficulty in controlling tantalum level, an alloy with 4.5 at%Ta was obtained, instead. Figure 2.6 shows the interdendritic segregation observed in the as received powder. X-ray analysis showed Ni_2AlTa (Heusler) and NiAlTa (C14 Hexagonal) as second phases. The cell size was about 8.5 μm.

All attempts at extruding this material failed. Table 2.3 shows the various parameters used for these extrusions. The inherent high strength of this multiphase alloy and the limitations of the extrusion process conditions are probably the reasons behind this failure. An alternate processing route was developed to obtain a 100% dense compact.

2.2.4 Vacuum Hot Pressing of NiAl+4.5at.%Ta Powder

The powder was sieved to remove particles larger than 150 μm (+100 mesh) and finer than 45 μm (-325 mesh). Vacuum hot pressing of 50 gm pellets was done at NASA Lewis Research Center, Cleveland, OH, in a unidirectional, graphite die hot press. The maximum pressure available was

21 MPa (3000 psi) and the maximum time available per run was about 6.5 hours. The variable that could be changed was temperature. Table 2.4 shows the various parameters used to achieve a 100% dense compact. % Density was determined by subtracting the pore area observed in a optical micrograph. Figure 2.7 shows a cross-section of a 61% dense compact obtained by vacuum hot pressing at 1523°K for 1 hour using 21 MPa pressure. The structure of fully dense compact can be seen in Figures 2.8 and 2.9. The prior particle boundaries are clearly visible in Figure 2.9. A fully dense compact was obtained at 1723°K using 21 MPa pressure for 6.5 hours. Average grain size of the compact was 8.5 μm which is same as the cell size in the original powder particles.

2.2.5 Cast NiAl+5at.% Alloy

A casting of an alloy with 5 at.% tantalum and 50 mm diameter was provided by the General Electric Corporation, Cincinati, OH. The porosity was less than .5 %. The interdendritic segregation could be easily removed by appropriate heat treatment as discussed later.

2.3 Chemical Analysis

Spectrographic analysis of the powders and the consolidated alloys was performed at NASA Lewis Research Center, Cleveland, Ohio and National Spectrographics, Cleveland, OH. Wet chemical analysis was done at Herron Testing Labs., Cleveland, OH. The results are presented in Table 2.5. The Ni:Al ratio is similar for NiAl, NiAl+1at.%Ta, NiAl+1at.%Nb and NiAl+4.5at.%Ta alloys. In the alloys containing 2 at.% tantalum or niobium the Ni:Al ratio is close to stoichiometry. The amount of oxygen is high in the powders because of the Al_2O_3 layer.

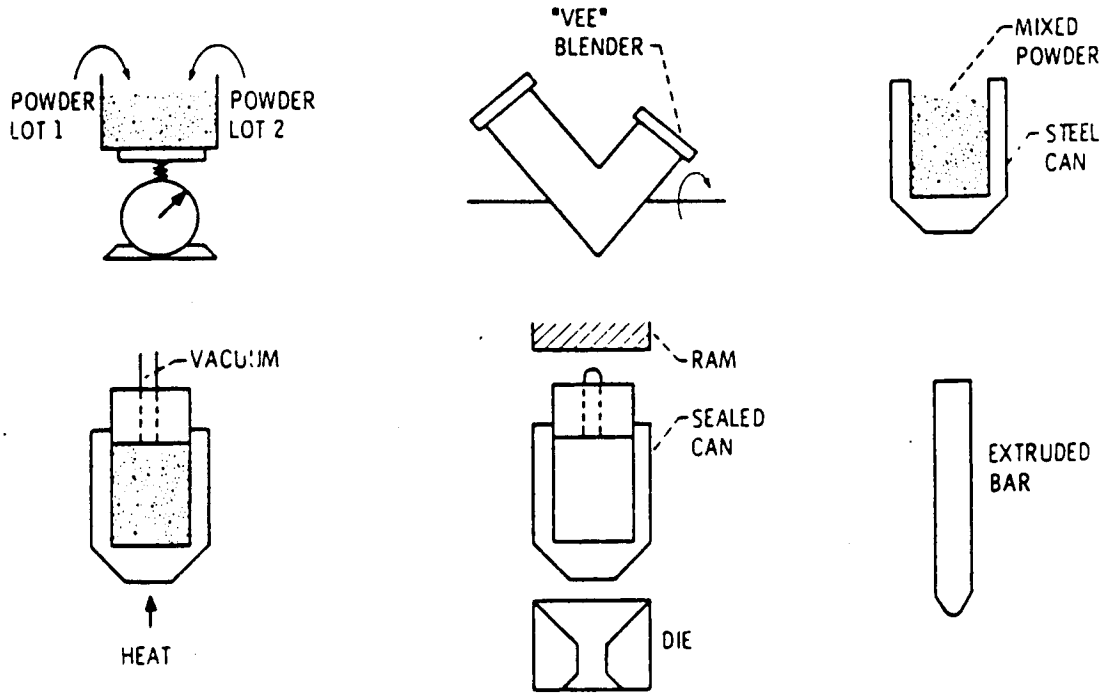

Figure 2.1 Powder processing of NiAl based alloys.

ORIGINAL PAGE IS
OF POOR QUALITY

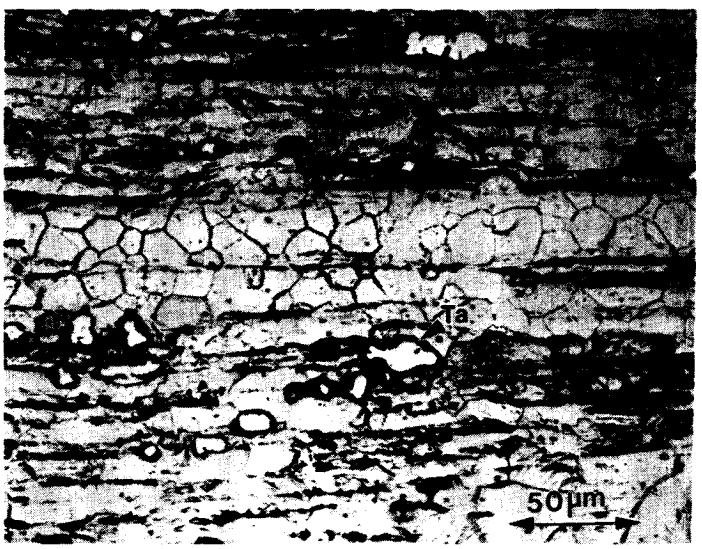

Figure 2.2 Optical microstructure of as extruded NiAl+2at.%Ta alloy.

ORIGINAL PAGE IS
OF POOR QUALITY

Figure 2.3 Back Scattered Electron (BSE) image showing the internal structure of NiAl+1at.%Ta powder particle.

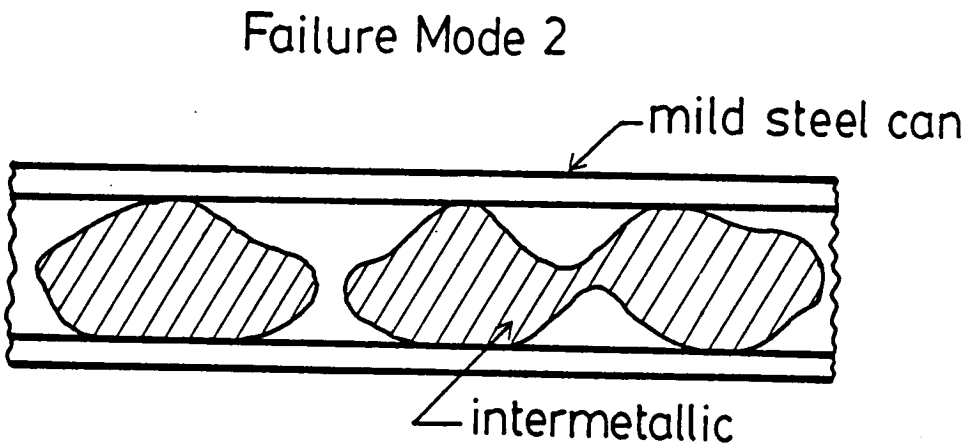

Figure 2.4 Cross section of extrusion with failure mode 2 in which the can material (mild steel) came through the die with unconsolidated chunks of intermetallic.

ORIGINAL PAGE IS
OF POOR QUALITY

Figure 2.5 Longitudinal microstructure of as extruded NiAl+1at.%Ta alloy showing oxide stringers parallel to the extrusion direction.

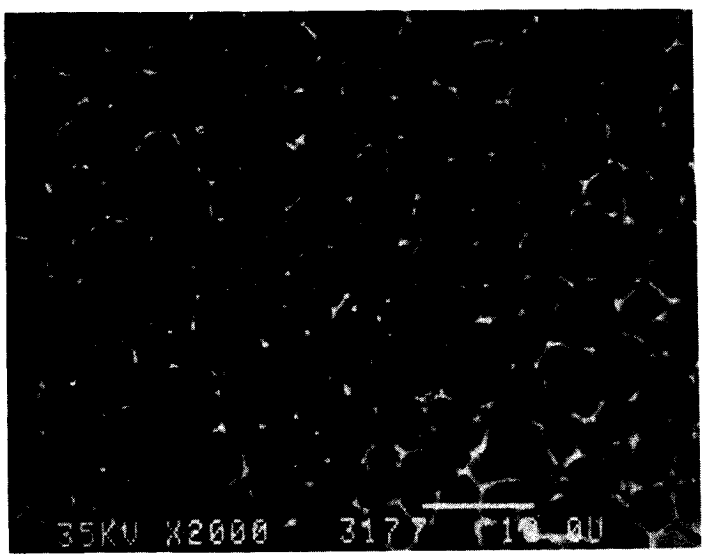

Figure 2.6 Interdendritic segregation observed in the as received NiAl+4.5at.%Ta powder. BSE image.

ORIGINAL PAGE IS
OF POOR QUALITY

ORIGINAL PAGE IS
OF POOR QUALITY

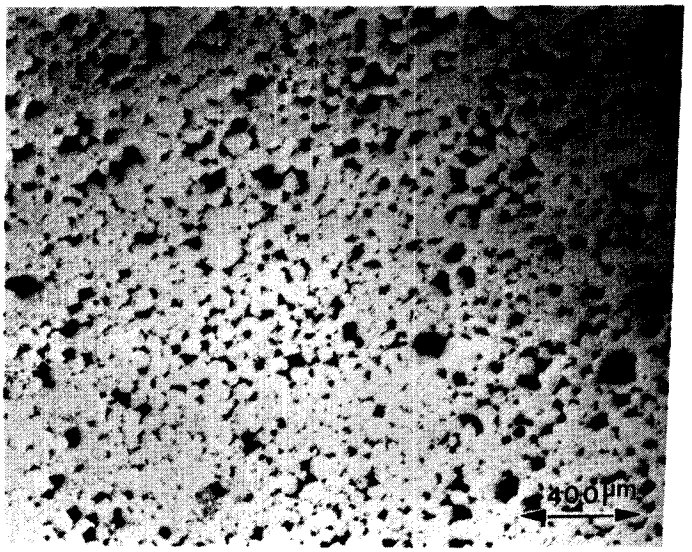

Figure 2.7 Cross-section of a 61% dense compact obtained by vacuum hot pressing at 1523°K for 1 hour using 21 MPa pressure.

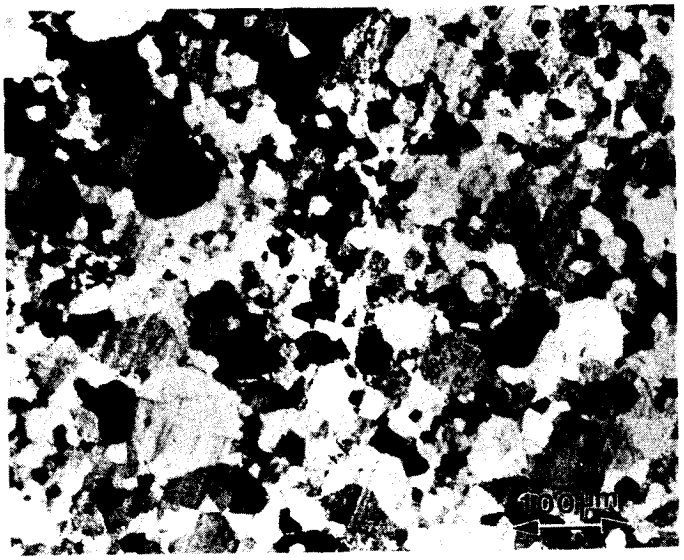

Figure 2.8 Optical micrograph of fully dense Vacuum Hot Pressed (VHP) compact.

ORIGINAL PAGE IS
OF POOR QUALITY

ORIGINAL PAGE IS
OF POOR QUALITY

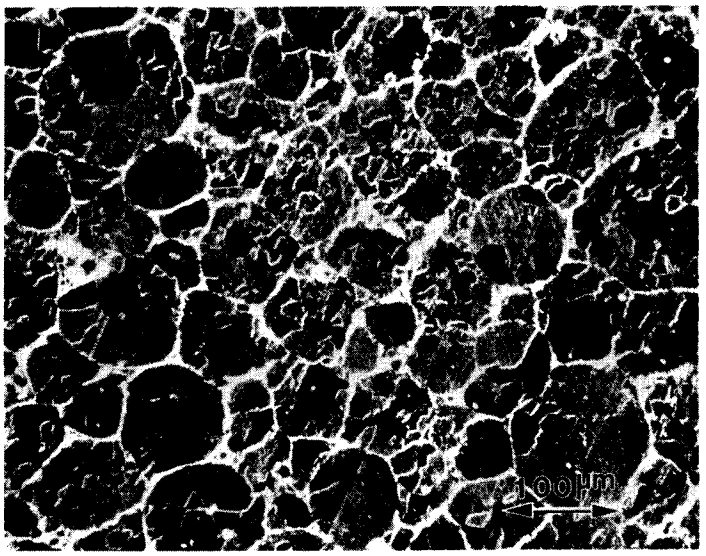

Figure 2.9 Dark field optical micrograph of fully dense Vacuum Hot Pressed (VHP) compact. The prior particle boundaries are clearly visible.

Table 2.1
Processing of NiAl as Reported in the Literature

Approx. Composition	Method	Reference
NiAl with varying composition	Induction melting and casting	Bradley and Taylor (1937)
NiAl+Mo Varying stoichiometry Varying amounts of Mo	Precision cast into tensile bars	Kinsey and Stewart (1951)
NiAl + Cr, Nb, Ti, Zr	--	Grinthal (1960)
NiAl NiAl+ 5 & 10 vol.% Al_2O_3 NiAl+ 3 & 6 vol.% ThO_2	Blended powders cold pressed in can. Sealed at 573 ^oK in 10^{-6}mm vacuum. Soaked at 1373 ^oK for 2 hrs. in H_2. Extruded at 16:1 reduction.	Seybolt (1966)
NiAl	Cast in graphite molds. Extruded at 1423 ^oK with 16:1 reduction ratio.	Rozner and Wasilewski (1966)
NiAl	Induction melting and casting into solid copper molds in gettered helium atmosphere. Canned in mild steel and extruded at 1373 - 1473 ^oK.	Wasilewski (1966)

Table 2.1 (continued)
Processing of NiAl as Reported in the Literature

Approx. Composition	Method	Reference
NiAl Varying stoichiometry	Induction melted and cast in water cooled copper boats.	Vandervoort, Mukherjee and Dorn (1966)
NiAl	Cast; single crystals grown from melt by slow cooling.	Ball and Smallman (1966)
NiAl	Single crystal NiAl rods grown from extruded bar stock by zone melting in purified argon.	Wasilewski, Butler and Hanlon (1967)
NiAl	Polycrystalline: Hot extrusion Single crystal: Modified Bridgeman technique and a strain anneal method.	Pascoe and Newey (1968)
NiAl + Ti	Arc melting in argon atmosphere and cast.	Polvani, Tzeng and Strutt (1976)
NiAl + Ta Various amounts	Argon arc melting, cast in water cooled copper hearth.	Nash and West (1979)
NiAl + graphite (.15 to .20 at.%)	Induction melting	Prakash and Pool (1981)

Table 2.1 (continued)
Processing of NiAl as Reported in the Literature

Approx. Composition	Method	Reference
NiAl	Cast and extruded at 1273 ^{o}K, 7:1; followed by 823 ^{o}K, 8:1; followed by recrystallization anneal at 998 ^{o}K for 1 hr. and then extrusion at 823 ^{o}K with 7:1 reduction ratio.	Baker and Schulson (1985)
NiAl + Ti, Ta, Cu, Nb, Mn, Mo	Blending of NiAl + ternary. Hot isostatic pressing at 1366 ^{o}K with 172.4 MPa pressure.	Pathare, Vedula and Titran (1985)
NiAl + Fe, Mo, W, Re, Mn, Hf	Blending of NiAl + ternary. Hot extrusion at 1366 ^{o}K, 16:1 ratio.	Pathare, Vedula and Titran (1985)
NiAl Varying stoichiometry	Hot extrusion of blended NiAl powders at 1100, 1420 and 1505 ^{o}K.	Whittenberger (1987)

Table 2.2
Extrusion Parameters
NiAl + 1 at.% Ta and NiAl + 1 at.% Nb

Material and ID	Soaking Temp. & Time	Transfer Time	Extrusion Ratio	Breakthrough Pressure	Running Pressure	Successful/ Failed (Fail mode)
NiAl+1at.%Ta DN73E1	1300 ^{o}K 2.4 hrs.	7.2 s	8:1	1217.6MPa (176.4ksi)	973.1MPa (141.1ksi)	Successful
NiAl+1at.%Nb DN41E1	1350 ^{o}K 4.8 hrs.	7.7 s	8:1	1179.3MPa (171.0ksi)	898.6MPa (130.3ksi)	Successful
Re-extrusion of DN73E1	1073 ^{o}K 3.5 hrs.	10.8 s	6:1	1289.7MPa (176.4ksi)	1056.6MPa (153.2ksi)	Failure mode 2
Re-extrusion of DN41E1	1073 ^{o}K 3.75 hrs.	11.3 s	6:1	Full Pressure	--	Failure mode 1
Re-extrusion of DN73E1	1350 ^{o}K 6.0 hrs.	10.0 s	6:1	1035.8MPa (150.2ksi)	528.3MPa (76.6ksi)	Failure mode 2
Re-extrusion of DN41E1	1350 ^{o}K 5.75hrs.	14.5 s	6:1	1225.5MPa (177.7ksi)	718.6MPa (104.2ksi)	Failure mode 2
NiAl+1at.%Ta DN73E4	1400 ^{o}K 3.7 hrs.	11.2 s	16:1	1280.7MPa (185.7ksi)	1140.7MPa (165.4ksi)	Successful
NiAl+1at.%Nb DN41E4	1400 ^{o}K 3.4 hrs.	9.1 s	16:1	1280.7MPa (185.7ksi)	1140.7MPa (165.4ksi)	Successful

Table 2.3
Extrusion Parameters
NiAl+4.5at.%Ta

Material and ID	Soaking Temp. & Time	Transfer Time	Extrusion Ratio	Breakthrough Pressure	Running Pressure	Successful/ Failed (Fail mode)
NiAl+4.5at.%Ta	1400°K 2.6 hrs.	13.1 s	16:1	Full Pressure	--	Failure mode 1
NiAl+4.5at.%Ta	1450°K 3.5 hrs.	6.5 s	6:1	1137.9MPa (165ksi)	827.6MPa (120ksi)	Failure mode 2
NiAl+4.5at.%Ta	1450°K 3.1 hrs.	6.5 s	8:1	Full Pressure	--	Failure mode 1
NiAl+4.5at.%Ta	1450°K 2.3 hrs.	11.5 s	8:1	1206.9MPa (175ksi)	1013.8MPa (147ksi)	Failure mode 2
NiAl+4.5at.%Ta	1450°K 2.4 hrs.	13.2 s	8:1	1186.2MPa (172ksi)	517.2MPa (75ksi)	Failure mode 2
NiAl+4.5at.%Ta	1400°K 2.2 hrs.	12.4 s	8:1	1289.7MPa (187ksi)	1013.8MPa (147ksi)	Failure mode 2

Table 2.4
Vacuum[1] Hot Pressing Parameters
NiAl+4.5at.%Ta

Pressure	Temperature	Time	% Density[2]
21 MPa	1523°K	1 hr.	61 %
21 MPa	1673°K	1 hr.	84 %
21 MPa	1673°K	3 hrs.	97 %
21 MPa	1673°K	6 hrs.	99 %
21 MPa	1723°K	6.5 hrs.	100 %

1 Vacuum of 100 μm
2 % Density = (100 - % Area occupied by the pores)

Table 2.5

Chemical Analysis of Alloys

Alloy Relative Accuracy	Form	Ni at.% 5%	Al at.% 5%	Ta at.% 5%	Nb at.% 5%	O ppm 10%	C ppm 15%	H ppm 20%	N ppm 15%
NiAl[Whittenberger 1987]	Extruded	54.37	45.50			900	110	200	40
NiAl+1at.%Ta	Powder	53.65	45.31	1.03		388	25	12	<10
NiAl+1at.%Nb	Powder	54.09	44.92		0.97	353	23	11	13
NiAl+2at.%Ta	Extruded	50.36	47.49	2.15		640[1]	20[1]	17[1]	40[1]
NiAl+2at.%Nb	Extruded	50.12	47.78		2.10	640[1]	20[1]	17[1]	40[1]
NiAl+4.5at.%Ta	Powder	51.02[2]	44.42[2]	4.56[2]		497	81	3	183
NiAl+4.5at.%Ta	VHP[3]	50.34[2]	45.15[2]	4.51[2]					
NiAl+5at.%Ta[4]	Cast	44.29[2]	50.38[2]	5.33[2]					

1 Interstitial content determined on original NiAl powder.
2 Wet chemical analysis. Metallic elements in all other alloys by spectrographic analysis
3 Vacuum hot pressed
4 Material contained some chromium

3. Physical Metallurgy

3.1 Introduction

Binary NiAl melts congruently at 1911°K [Alexander and Vaughan (1937)]. It does not show any phase transformations upto the melting point. However, with addition of a third element the physical metallurgy of NiAl changes drastically. These ternary alloys had to undergo various thermo-mechanical treatments during processing. It is important to know the phases present, their relative amounts and their distribution during various stages of processing. The size, morphology and distribution of second phases in the matrix can be affected by thermo-mechanical treatments. These second phase parameters have a profound effect on the elevated temperature creep properties of the ternary alloys. Another important parameter is the grain size; it has substantial effect on the creep properties. So the objectives of this investigation were:

(i) To identify all the phases present at various stages of thermomechanical processing.

(ii) To identify the phase transformations in these alloys.

(iii) To document the distribution and morphology of the

second phases.

(iv) To study the grain growth characteristics.

In this chapter the available phase diagram information is described first. The experimental techniques and the results obtained are described following the literature survey. Lastly, the results of grain growth experiments are discussed.

3.2 Literature Survey

Only limited phase diagram information exists about the Ni-Al-Ta and Ni-Al-Nb ternary phase diagrams. At least three possible ternary compounds between nickel, aluminum and tantalum have been reported in the literature. NiAlTa has a hexagonal $MgZn_2$ (C14) type structure with a unit cell containing 4 molecular units [Kusma and Nowotny (1964)]. Ni_2AlTa has the cubic Heusler alloy structure (Cu_2AlMn type) with a_o = 0.5949 nm [Giessen and Grant (1965)]. $(Al_{0.5}Ta_{0.5})Ni_3$ has the hexagonal Ni_3Ti type (DO_{24}) structure with a_o = 0.5112 nm and c_o = 0.8340 nm. Most recent and relatively complete work has been done by Nash and West (1979). They have made an investigation of the constitution of the Ni-Al-Ta system in the composition range ~ 50 - 100

at.% nickel. In this range isothermal sections of the ternary phase diagram have been determined for the temperatures of 1523 and 1273°K. Figure 3.1 shows the isothermal section at 1273°K. The part of the system studied contained all the three ternary intermediate phases described before. They have also obtained evidence of the occurrence of a peritectoid reaction

$$NiAl + NiTa \rightarrow Ni_2AlTa + NiAlTa$$

occuring at a temperature between 1273 and 1573°K.

Three ternary intermediate phases containing nickel, aluminum and niobium which are isostructural with the corresponding compounds in the Ni-Al-Ta system have been reported in the literature. Markiv, Matushevskaya and Kuzma (1966) have reported a large phase width for the nickel and aluminum in the phase $Nb(Ni,Al)_2$, which for simplicity can be denoted as NiAlNb and has the hexagonal $MgZn_2$ type C14 structure. The Ni_2AlNb phase is centered around $Ni_{2.08}Al_{0.92}Nb$ and has the ordered $Cu_2AlMn(L2_1)$ structure [Benjamin, Giessen and Grant (1966)]. A metastable phase Ni_6AlNb has been found to form in splat quenched material [Giessen and Ray (1971)]. Kornilov et al (1965) have presented a psuedo-binary phase diagram between NiAl and niobium (Figure 3.2). Markiv, Matushevskaya and Kuzma

(1966) have presented isothermal sections at 1073 and 1173°K. Recently Nash, Kavishe and West (1980) have presented an isothermal section of nickel-rich region at 1473°K. Structures of some of these phases are shown in Figure 3.3.

3.3 Experimental Techniques

3.3.1 Optical Microscopy and Scanning Electron Microscopy

All the metallographic samples were prepared with the following polishing sequence on Abrapol by Struers.

SiC paper 320 → 400 → 600 grit

SiC slurry 10 μm → 5 μm

Diamond 3 μm → 1 μm

SiO_2 / Al_2O_3 0.05 μm

Optical microscopy was done on a Nikon Epiphot microscope equipped with differential interference contrast (DIC) imaging. It was also possible to do dark field imaging on the same microscope. Since the intermetallic compounds are difficult to etch these techniques are useful to see the second phases, grain boundaries and the prior particle boundaries. Etchants used are listed below:

(i) 33 v/o of H_2O + 33 v/o HNO_3 + 33 v/o acetic acid + 1 v/o HF. This etchant etches grain boundaries preferentially.

(ii) 10 g $CuSO_4$ + 50 ml H_2O + 50 ml HCl Marbel's reagent. This etchant etches grain boundaries, second phases and prior particle boundaries giving rise to a very severe etch.

(iii) 25 v/o HF + 75 v/o H_2O saturated with molybdic acid. This etchant colors entire grains giving different colors depending on orientation.

Scanning Electron Microscopy was done on a Cambridge 100 at NASA Lewis Research Center, Cleveland, OH. Most of the imaging was done with the back scattered electrons as it showed the distribution of heavier elements such as tantalum and niobium.

3.3.2 Differential Thermal Analysis (DTA)

It is a technique of recording the difference in temperature between a substance and a reference material against either time or temperature as the two specimens are subjected to identical temperature regimes in an environment heated or cooled at a controlled rate. The record is a differential thermal or DTA curve; the

temperature difference (ΔT) is plotted on the ordinate with endothermic reactions downwards and time(t) or temperature(T) on the abscissa increasing from left to right.

As the alloy undergoes a phase transformation, in most instances there is evolution or absorption of heat. This heat is evolved or absorbed in the sample itself and hence its temperature with respect to the reference is changed. If the transformation is isothermal a very sharp peak is observed. For a phase transformation taking place over a range of temperature (e.g. liquid + solid region in a phase diagram) the transformation usually begins at the onset point and nears completion at the peak temperature. Because of the changes in thermal conductivity, specific heat and volume of sample during and after transformation the base line can also deviate considerably. For a review of various DTA techniques see Smothers and Chiang (1966).

Analysis was done on a Netzsch Simultaneous Thermal Analyser STA 429 at NASA Lewis Research Center, Cleveland, OH. Samples were held in an alumina crucible. Platinum was used as a standard. Furnace atmosphere was helium. The rate of heating and cooling was 10°K per

minute unless otherwise noted. Figure 3.4 illustrates the terms used in the analysis of scan. All the DTA traces discussed hereon are shown in Appendix I.

3.3.3 X-ray Analysis

3.3.3.1 Equipment

X-ray diffraction anlysis was performed on a Philips Autodiffractometer using a monochromated Cu K_α radiation with an average wavelength of 0.15418 nm. Pulverized samples were scanned from 25 degree 2θ to 85 degree 2θ with .05 degree steps and 10 seconds counting time at each step. Intensity vs 2θ values were collected on an IBM PC interfaced with the diffractometer and later sent to VAX for further analysis.

3.3.3.2 Computer Analysis of Data

Analysis was performed using the SPECPLOT program written by P.C. Gillette of Case Western Reserve University, Cleveland, OH. This program is available for VAX PDP-11 system.

Scaling: The intensity values were scaled to fit between

0 and 100.

Smoothing: Because the arrival of x-ray quanta in the counter is random in time; noise is present in the spectra. To reduce this noise following smoothing function was applied 5 times to the intensity values:

$$I(i) = 1/2\ (1/2\ I(i-1) + I(i) + 1/2\ I(i+1))$$

where $I(i)$ is intensity at a 2θ value,

$I(i-1)$ is the intensity at the previous 2θ value,

and $I(i+1)$ is the intensity at the next 2θ value.

Integrated Intensity Measurements: The program draws a straight line between two points specified by user and measures the area under the curve. An example is shown in Figure 3.5.

Overlapping Peaks: When two or more peaks overlapped they were seperated by fitting the individual peaks to a Lorentzian curve. An example of such deconvolution is shown in Figure 3.6.

Theoretical Intensity Calculations: In order to calculate the volume fractions of the phases present it is necessary to calculate the theoretical intensity for major peaks for each phase present. Examples of such

calculation are given by Cullity (1978). Such calculations were performed for the NiAl+2at.%Ta alloy and the NiAl+4.5at.%Ta as received powder.

Lattice Parameter Calculations: Lattice parameters were calculated using the HERTA program available at NASA Lewis Research Center, Cleveland, OH. This program uses a $\cos\theta\cot\theta$ fit to calculate the parameters and the error. The relatively large values of error are due to the use of low angle peaks in the calculation.

Phase Identification: Phases were identified by comparing the peak intensities and d-spacings to the powder diffraction file for expected phases and to the calculated theoretical intensities wherever applicable.

3.3.4 Transmission Electron Microscopy (TEM)

For TEM examination the diameter of cylindrical samples was reduced to 3 mm by centerless grinding. Specimens were cut perpendicular to the testing direction and then mechanically ground on 600 grit SiC paper to 250 μm thickness. Some discs were cut using electro-discharge machining (EDM). The 3 mm diameter disks were electrochemically thinned to perforation

using the parameters listed in Table 3.1.

3.4 Results and Discussion

3.4.1 NiAl+1at.%Ta and NiAl+1at.%Nb Alloys

No second phase was observed for alloys homogenized at 1300°K. The DTA traces do not show any phase transformation before melting. Also the TEM micrographs showed very little volume fraction of the second phase; of the order of a fraction of a % (see Figure 3.7). Therefore it is reasonable to assume that at 1300°K these 2 alloys are single phase. Nash (1985) has reported solubilities of 5 and > 5.5 at.% for tantalum and niobium in NiAl.

Stoichiometric NiAl melts congruently at 1911°K [Alexander and Vaughan (1937)]. Any deviation from stoichiometry results in incongruent melting and lower melting point. A liquid + solid region of about 62 to 65 °K was observed for all these alloys. Details are shown in Tables 3.2 and 3.3. No other phase transformation was observed in these alloys, suggesting that they were single phase alloys. The liquidus temperature of alloys containing 1 at.% tantalum or niobium were observed to be higher than 1911°K which is the reported congruent

melting point of stoichiometric NiAl. But it would be erronious to conclude that these additions raise the liquidus temperature of off-stoichiometric NiAl. It was assumed that the liquidus occurs at the peak temperature while heating. This assumption may not be correct. Also the amount of impurities in all the alloys is not likely to be the same.

3.4.2 NiAl+2at.%Ta Alloy

NiAlTa is the stable second phase at 1300°K in this alloy. The details of this work are shown here. It should be noted that in this alloy the Ni/Al ratio is closer to stoichiometry than the alloys with 1 or 4.5 at.%Ta.

3.4.2.1 Analysis

The lattice spacings and peak intensities for the precipitate phase, obtained from an X-ray diffractometer scan on a pulverized section of a compression tested specimen of the alloy, are listed in Table 3.4. The observed d-spacings matched well those for the compound NiAlTa as reported by Kusma and Nowotny (1964) and Markiv et al (1964). The d-spacings obtained from the

diffractometer scan were used in a (cos θ cot θ) extrapolation to compute the lattice parameter of the NiAlTa precipitate phase. The calculated lattice parameters were a_o = 0.4900±0.0013 nm and c_o = 0.7929±0.0029 nm. Peak intensities for the NiAlTa phase were also calculated taking into account the structure factor, Lorentz-polarization factor and multiplicity factor. The structure factor and the multiplicities of reflections were computed assuming an ideal $MgZn_2$ type (C14) structure [Kusma and Nowotny (1964)]. The d-spacings obtained from the calculated lattice parameters and the calculated peak intensities are compared with the experimentally determined values in Table 3.4. The good agreement between the observed and corresponding calculated values confirms that the precipitate phase in the alloy was NiAlTa.

Figure 3.8 contains a TEM bright field image of the precipitate phase viewed along a [100] matrix direction. Evidence that complete homogenization of the blended NiAl and tantalum powder did not occur was obtained from the observation of a very non-uniform distribution of precipitates. The precipitates exhibited an irregular plate morphology. The plate edges varied from sharp and facetted to blunt and smoothly curved. Figure 3.8 shows

that the habit plane of the precipitates was close to {012} of the matrix. Chemical microanalysis of the alloy using EDS determined that the matrix was NiAl with a small amount of tantalum in solid solution. The precipitates were found to be considerably richer in tantalum. Typical EDS spectra from the matrix and a precipitate are shown in Figure 3.9.

A single matrix region containing a large precipitate was tilted in the TEM to position its $[\bar{1}11]$, [011] and $[\bar{1}00]$ zone axes parallel to the electron beam. Superimposed single crystal SAD patterns of the matrix and the precipitates were obtained for each of the three orientations. An example is shown in Figure 3.10. The indexing of the precipitate SAD patterns matched well with the d-spacings and interplanar angles predicted for the NiAlTa phase. A consistent precipitate matrix orientation relationship among the three SAD patterns was observed. The orientation relationship can be expressed as $[\bar{1}11]_M//[1\bar{2}16]_{Ppt.}$ and $(01\bar{1})_M//(10\bar{1}0)_{Ppt.}$ It is shown in Figure 3.11. Thus, the prism planes of the hexagonal NiAlTa phase were found to be parallel to the closest packed planes in the B2 structure of the matrix.

3.4.2.2 Discussion

Several different values for the lattice parameters of NiAlTa have been reported. Kusma and Nowotny (1964) determined a_o = 0.4969 nm and c_o = 0.7985 nm for pure NiAlTa. Markiv et al. (1964) have reported a_o = 0.4932 nm and c_o = 0.7980 nm. Recently, Nash and West (1979) have reported a_o =0.5015 nm and c_o = 0.8171 nm for NiAlTa precipitated in an alloy containing 59.3 at.% Ni, 35.8 at.% Al and 4.9 at.% Ta. The lattice parameters of a_o = 0.4903 nm and c_o = 0.7929 nm determined in this study most closely match those of Markiv et al. (1964). The scatter in the reported lattice parameters could be from several sources. The NiAlTa phase may have a range of stoichiometry, and thus lattice parameters. Also the difficulty of analyzing high angle peaks in the NiAlTa phase causes relatively large uncertainties in the determination of its lattice parameters.

A well-defined orientation relationship between the NiAlTa precipitates and the NiAl matrix was observed. The crystal structures of the two phases are quite different. It is very interesting to see how well the atomic densities and locations of atoms match on the precipitate and matrix planes which are parallel to each other. Figure 3.12(a) shows the stacking of $(10\bar{1}0)$

planes of the NiAlTa phases to be ABCDEABCDE. The density of atoms on these planes is quite low. The A, B and E planes have 19.438 x 10^{-20} m^2 per atom and the C and D planes have 12.959 x 10^{-20} m^2 per atom. The {011} planes in NiAl are stacked ABAB. These planes are more densely packed with 5.894 x 10^{-20} m^2 per atom. By combining the E+A+B or C+D planes of the NiAlTa phase, each combination will produce a denser packing of 6.479 x 10^{-20} m^2 per atom which is comparable to the {011} planes in NiAl. The atomic positions on the grouped planes in the NiAlTa phase still do not match very well those on the {011} planes of NiAl. This point is illustrated in Figure 3.12(b) which shows an overlay of a (011) plane of NiAl on the combined E+A+B $(10\bar{1}0)$ planes of NiAlTa. Not the {011} plane of the NiAl, but the lower packing denisty {012} planes were observed to be the habit planes for the NiAlTa precipitates. The {012} planes of the NiAl phase have 18.638 x 10^{-20} m^2 per atom which is comparable to the low atomic densities of planes in NiAlTa.

3.4.3 NiAl+2at.%Nb Alloy

Sherman and Vedula (1986) have shown that hexagonal NiAlNb phase is the second phase at 1300°K. This was

confirmed during this study also.

3.4.4 NiAl+4.5at.%Ta Alloy

Results of the DTA analysis are presented in Tables 3.3 and 3.5. An extra peak at 1800.5°K is observed while heating the as received powder. This peak is not observed in the annealed powder. The as received powder of this alloy shows interdendritic segregation (Figure 2.6). So this peak is most likely to be associated with a non-equillibrium phase which disappears upon annealing. The x-ray analysis showed that the as received powder contained NiAlTa and Ni_2AlTa as second phases. However, the annealed powder contained Ni_2AlTa and an unknown phase with $Ta_5Ni_3Al_2$ composition.

The liquidus of this alloy is lower than the binary NiAl or NiAl+1at.%Ta and NiAl+1at.%Nb alloys. This suggests that the liquidus surface is sloping down from a peak at binary NiAl. X-ray analysis showed that volume fraction of Ni_2AlT decreased with temperature and no Ni_2AlTa was observed at 1773°K. So it must be transforming into a liquid phase at about 1732°K where a DTA peak is observed.

Figure 3.13 shows the solidus projection at 1673°K and 1773°K. This figure has been constructed from the data of Nash and West (1979) and present work. The phase equillibrium near NiAl for Ni-Al-Ta Alloys is very complex. For nickel rich alloys it is possible to obtain Ni_2AlTa or both Ni_2AlTa and $Ta_5Ni_3Al_2$ as second phases. Whereas, for aluminum rich alloys NiAlTa or both NiAlTa and Ni_2AlTa will be the equillibrium second phases depending on exact composition. From the solidus projection at 1673°K, it is clear that Ni_2AlTa and $Ta_5Ni_3Al_2$ are the equillibrium second phases in this alloy. Any heat treatment above 1700°K (e.g. Figure 3.13 b) can result in a liquid phase that can solidify as non-equillibrium NiAlTa and equillibrium Ni_2AlTa upon cooling.

Table 3.6 shows the results of x-ray analysis for the alloys studied. The approximate amounts of different phases present, as indicated by the relative integrated intensities of major peaks are presented in Figure 3.14. All the x-ray diffraction scans used in the analysis are presented in Appendix II. Figure 3.3 shows the structures of some of the phases encountered in this study.

The changes in the lattice parameter for the phases in NiAl+4.5at.%Ta alloy were studied. The lattice parameter of NiAl increases with increasing temprature up to 1673°K. However, the trend is not continued at 1703°K and 1723°K. The DTA analysis showed a phase transformation around 1732°K. It is likely that amount of tantalum in solution with the NiAl increases with increasing temperature and hence the lattice parameter of NiAl increases. When the phase transformation takes place all the tantalum is tranferred to the (presumably) liquid phase and hence the lattice parameter drops back to pure NiAl. A similar drop in the value of the lattice parameters is also observed for Ni_2AlTa and the unknown cubic phase $Ta_5Ni_3Al_2$. But the error in the values is larger than the observed drop. The alloys were heat treated at the given temperature for 24 hours and then quenched using cold argon. The cooling rate obtained was 120°K/min for the alloys homogenized at 1703°K and 1723°K. This quenching resulted in strain that can be apparent from the distorted X-ray peak shapes for these two alloys. It is likely, therefore, that this strain could lead to erroneous values of lattice parameters at 1703°K and 1723°K. It is also important to note that this alloy shows a phase transformation, probably involving the melting of Ni_2AlTa, at 1732°K. The

lattice parameters of phases involved could change abruptly near that temperature. The results are presented in Figures 3.15, 3.16 and 3.17.

3.4.4.1 Analysis of the Unknown Phase in NiAl+4.5at.%Ta Alloy

Figure 3.18 shows a cluster of phases in the heat treated NiAl+4.5at.%Ta alloy. The lighter phase is Ni_2AlTa with an ordered cubic $L2_1$ structure (see Figure 3.3). The darker phase in the center is an ordered face centered cubic phase with lattice parameter of 1.1331±.0091 nm and approximate composition $Ta_5Ni_3Al_2$. The analysis of this previously unreported phase is presented below.

3.4.4.1.1 Chemistry

X-ray Energy Dispersive Spectroscopy was done on a Philips 400T transmission electron microscope equipped with a Tracer Northern 5500 X-ray Analyzer. The detector parameters used are as follows:

Beryllium Window Thickness	14 μm
Silicon Dead Layer Thickness	0.15 μm
Gold Layer Thickness	10 nm

The spectra were collected at 120 KeV excitation energy and analyzed using the Standardless Metallurgical Thin Film Analysis (SMTF) software supplied with the TN-5500 system.

Simultaneous analysis of any alloy containing nickel, aluminum and tantalum poses a great deal of difficulty since there are major overlaps of peaks. There is a complete overlap of Ni-K_β (8.263 KeV) with Ta-L_α (8.145 KeV) and a partial overlap of Al-K_α (1.486 KeV) with Ta-M (1.709 KeV). Therefore the characteristic x-ray peaks used in the analysis were

Ni-K_α	7.471 KeV
Al-K_β	1.486 KeV
Ta-M	1.709 KeV

The effective K-ratios were determined experimentally using the Ni_2AlTa phase as the standard. The Ni_2AlTa phase is easily recognized by its diffraction pattern. The ratios were determined using the following expressions:

$$\frac{C_{Al}}{C_{Ni}} = K_{AlNi} \frac{I_{Al}}{I_{Ni}}$$

$$\frac{C_{Ta}}{C_{Ni}} = K_{TaNi} \frac{I_{Ta}}{I_{Ni}}$$

where C_X is the wt.% of the element in the analyzed volume. The effective K-ratios obtained were:

$$K_{AlNi} = 1.30$$

$$K_{TaNi} = 2.35$$

These ratios were then used in the analysis of the unknown phase. All the spectra collected had approximately the same number of counts for the Ni-K_α peak and the same probe size and dark current. Examples of the spectra for Ni_2AlTa, the unknown phase and the matrix are shown in Figures 3.19, 3.20 and 3.21. The corresponding chemical analyses is given in Tables 3.7, 3.8 and 3.9. According to this analysis the matrix of NiAl+4.5at.%Ta alloy had about 3 at.% tantalum in solution and the unknown phase has a composition of $Ta_5Ni_3Al_2$.

3.4.4.1.2 Electron Diffraction

Figures 3.22 (a),(b) and (c) show electron diffraction patterns for the unknown phase taken with a camera length of 800 mm. These patterns could be indexed

as [$\bar{1}$12], [$\bar{1}$22] and [012] zones of an ordered face centered cubic phase. Figure 3. shows a convergent beam diffraction pattern (CBDP) with [012] zero order Lauve zone (ZOLZ). The first and the second order Lauve zones (FOLZ and SOLZ) can also be seen. Williams (1984) has described a method of determination of interplanar spacing parallel to the electron beam. From that spacing the lattice parameter can be easily obtained.

If R_1 and R_2 are the radii of the FOLZ and the SOLZ on the negative then

$$G_1 = \frac{R_1}{\text{Camera Constant}} \quad \text{and} \quad G_2 = \frac{R_2}{\text{Camera Constant}}$$

where G_1 and G_2 are radii of the higher order Lauve zones in the reciprocal space. Then

$$G_1 = (2KH)^{1/2} \qquad \text{and} \quad G_2 = 2(KH)^{1/2}$$

where $K = 1/\lambda$. Thus by measuring R values, the reciprocal lattice spacing H and hence the crystal repeat spacing parallel to the beam can be determined, if the Miller indices for the direction of H are known. These can be calculated for a specific beam direction UVW since for an fcc crystal

$$H_{UVW} = \frac{p}{a_o(U^2+V^2+W^2)^{1/2}}$$

where a_o is the lattice parameter and p is 1 for (U+V+W)

odd and 2 for (U+V+W) even. Table 3.10 shows the results of such computation.

In summary, the electron diffraction has shown this phase to be an ordered fcc phase, with a lattice parameter of 1.2 nm.

3.4.4.1.3 X-ray Diffraction

Cullity (1978) has described the method used to index patterns of cubic crystals. A cubic crystal gives diffraction lines whose $\sin^2\theta$ values satisfy the following equation,

$$\frac{\sin^2\theta}{(h^2 + k^2 + l^2)} = \frac{\sin^2\theta}{s} = \frac{\lambda^2}{4a_o^2}$$

Since the sum $s = (h^2 + k^2 + l^2)$ is always integral and $\lambda^2/4a_o^2$ is a constant for any one pattern, the problem of indexing the pattern of cubic substance is one of finding a set of integers s which will yield a constant quotient when divided one by one into the observed $\sin^2\theta$ values. Table 3.11 shows an example of such computation. The lattice parameter agrees very well with the one obtained from convergent beam diffraction pattern.

3.5 Grain Growth

In this section the theory of grain graowth and the phenomena of secondary recrystallization are discussed first. The results of grain growth experiments for NiAl+1at.%Ta alloys extruded from unsieved and sieved powder are presented. Their behavior is contrasted with the very sluggish grain growth in NiAl+4.5at.%Ta alloy with larger volume fraction of second phase precipitates.

3.5.1 Theory of Grain Growth

The effect of solid solution and second phases on grain growth is well documented. For example, a fraction of one percent of molybdenum or manganese in solution in iron reduces the grain growth rate at a given mean grain size and temperature by several orders of magnitude [Leslie, Michalal and Aul (1963)]. Here impurities exert their effect through segregation to grain boundaries but without forming precipitates. Again a dispersed phase, even in small quantities, can retard boundary motion and eventually bring grain growth to a halt. In this case the growth law should be controlled by the difference

between current grain size and the limiting grain size at that temperature [Burke and Turnbull (1952)]. Smith (1948) has reported a computation by Zener which indicates that the limiting grain size should be given approximately by the expression

$$D_l = d/f$$

where D_l is the limiting grain size, d is the average diameter of the inclusions and f is their volume fraction. The increase in limiting grain size with increasing temperature may result from either the solution or coalescence of growth inhibiting inclusions [Burke and Turnbull (1952)].

3.5.2 Secondary Recrystallization

When the annealing of an initially deformed sample is continued long beyond the stage when primary recrystallization is complete, the even tenor of grain growth may be interrupted by the sudden very rapid growth of a few grains only, while the rest of the grains remain small and are eventually all swallowed by the large grains. The process has the following general characteristics:

(a) The large grains are not freshly nucleated; they are merely particular grains of the primary structure

grown large.

(b) It occurs readily in materials where normal grain growth is very slow. Inhibition by second phase, solid solution etc. may all play a part.

(c) A well-defined minimum temperature must be exceeded for secondary recrystallization. The largest grains are normally produced just above this temperature; at higher annealing temperatures, smaller secondary grains result.

3.5.3 NiAl+1at.%Ta

Abnormal grain growth or secondary recrystallization seems to occur (Figure 3.24) between 1273°K and 1473°K. There is very little grain growth below 1273°K even after 72 hours anneal. Since the annealing times were very high, the grain size obtained at each temperature is the limiting grain size. The grain size vs. temperature data can be fitted to

$$D_T = A \exp(-Q_G/RT)$$

where D_T is the limiting grain size at temperature T, and Q_G is the activation energy for grain growth. Best fit is obtained if we consider two different activation energies. Below 873°K, Q_G is equal to 0.55±0.15 kJ/mole and above 1473°K, Q_G is equal to 151±21 kJ/mole (Figure

3.25). This change in the activation energy occurs at the temperature at which abnormal grain growth just begins, hence these two phenomena are related. Longitudinal microstructure of as extruded NiAl+1at.%Ta shows (Figure 2.5) oxide stringers parallel to the extrusion direction. These stringers are likely to impede grain boundary motion across them. Some boundaries were found to have crossed them at the higher annealing temperatures (Figure 3.26). Haff and Schulson (1982) have done grain growth studies on cast and extruded NiAl. Since their material did not have any oxide stringers, they have not observed any abnormal grain growth. One more reason for the very small grain growth at lower temperatures is likely to be the solid solution alloying of NiAl with tantalum.

3.5.4 NiAl+1at.%Ta with Sieved Powder

To see the effect of powder particle size on the grain growth charasterics, one extrusion was made with powder particles less than 45 μm in diameter sieved out. Extrusion was done at 8:1 ratio at 1400°K. The as extruded grain size was almost the same as the size obtained from extrusion of unsieved powder. The mean limiting grain size at various temperatures was higher

than unsieved powder, although this could not be said with statistical certainty. Abnormal grain growth was again observed, however, at a lower temperature. The specific surface area in the sieved powder was much less compared to the unsieved powders. The amount of oxide present on the powder would be less in the case of the sieved powder. Therefor grain growth is more rapid and shift to abnormal grain growth occurs at a lower temperature.

3.5.5 NiAl+4.5at.%Ta

No abnormal grain growth was observed in this material even after a 24 hour anneal at 1723°K. As hot pressed microstructure showed tantalum rich precipitates on the grain boundaries and in the matrix (Figure 3.27). These precipitates, especially the ones at grain boundaries would slow down any grain boundary motion, even at high temperatures.

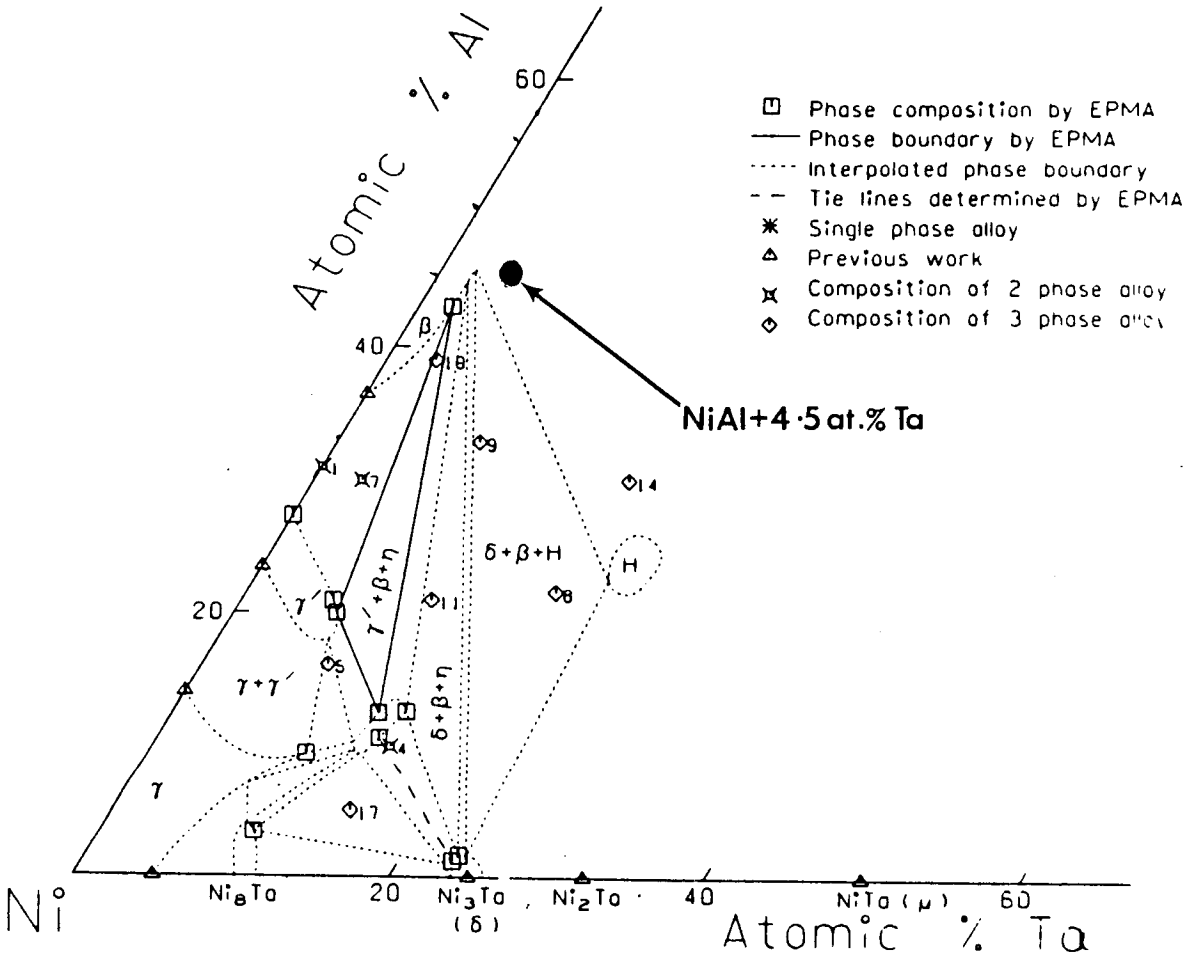

Figure 3.1 Isothermal section of Ni-Al-Ta system at 1273 K [Nash and West (1979)].

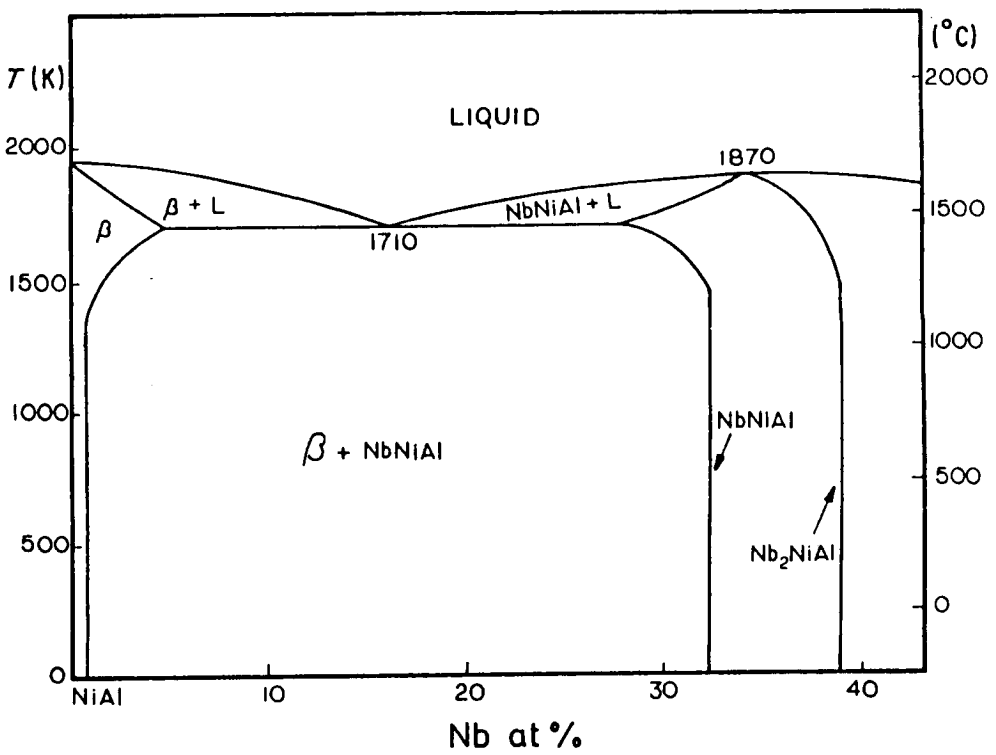

Figure 3.2 A pseudo-binary phase diagram for the NiAl-Nb system [Kornilov et al (1965)].

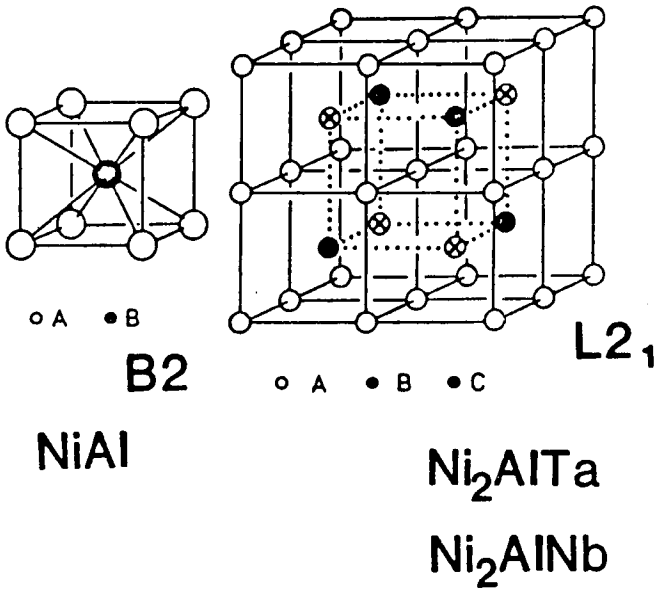

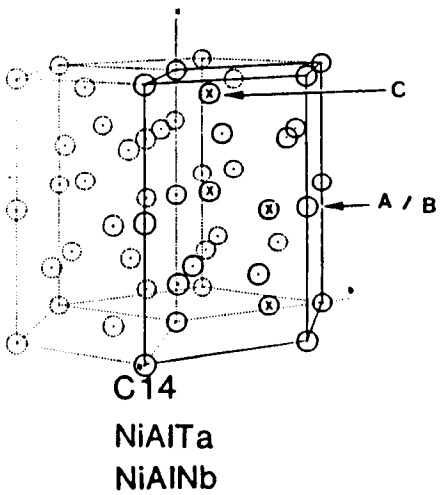

Figure 3.3 Structure of phases of interest

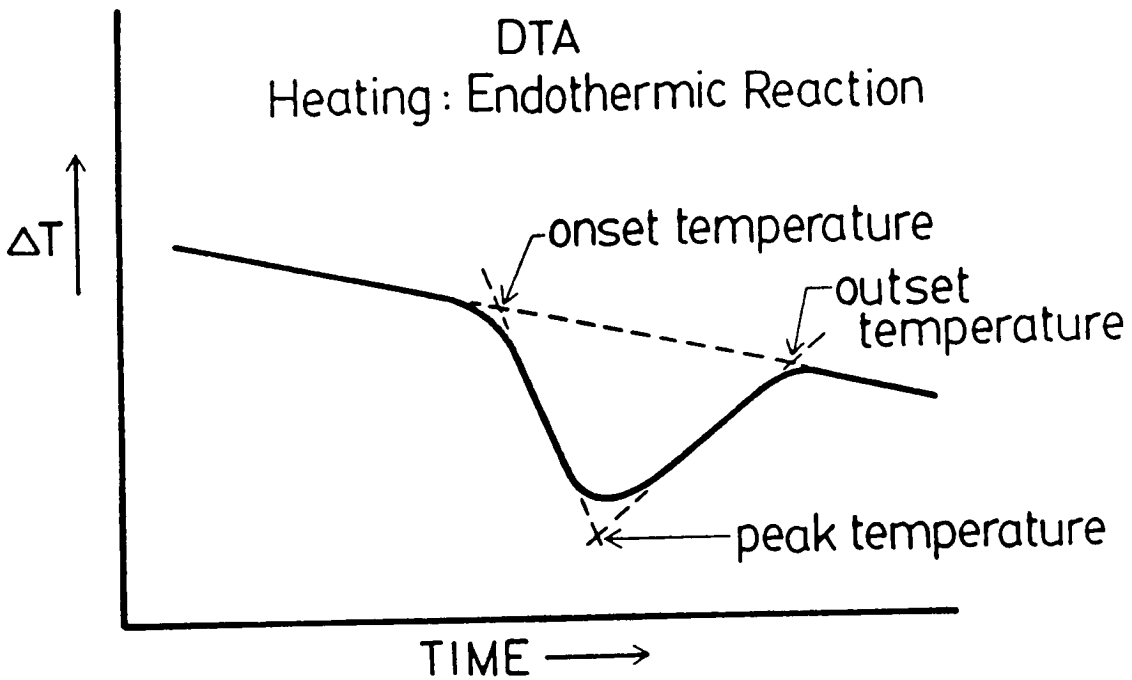

Figure 3.4 The terminology used in the analysis of a DTA scan.

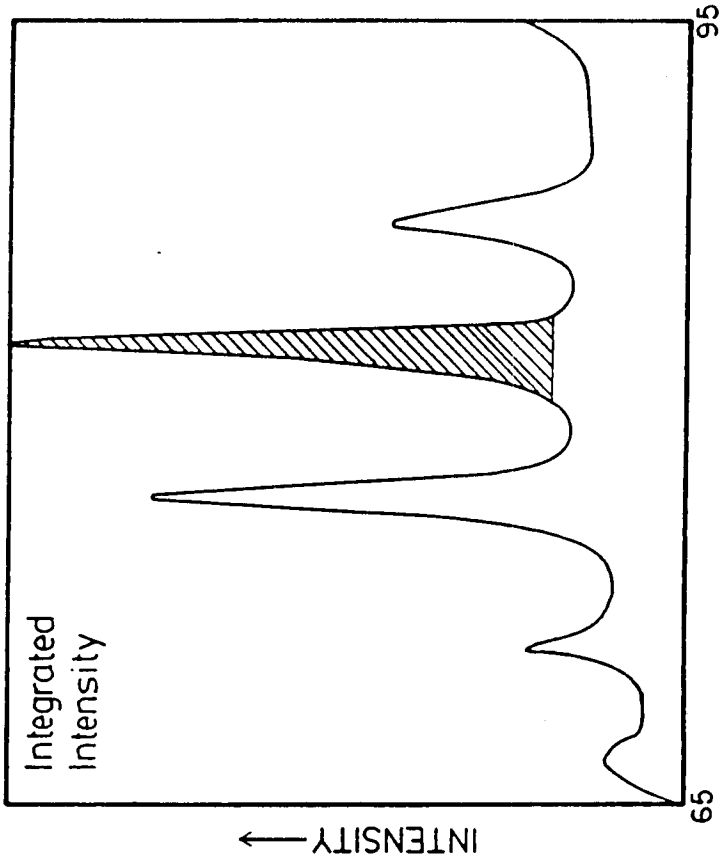

Figure 3.5 Measurement of integrated intensity of an x-ray peak.

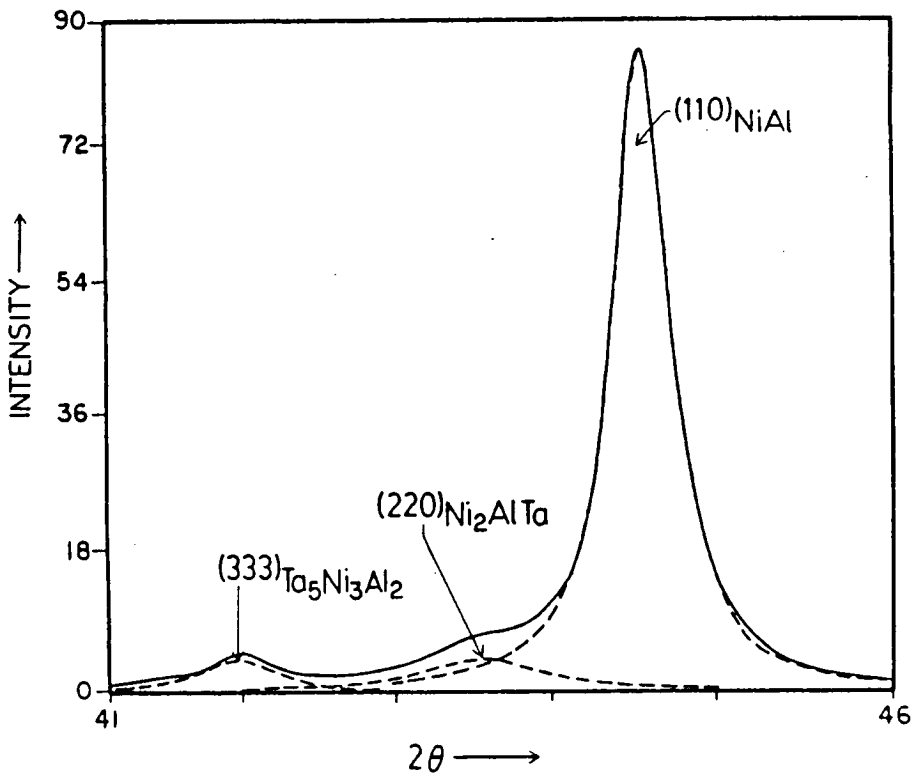

Figure 3.6 Deconvolution of overlapping peaks by Lorentzian fit.

ORIGINAL PAGE IS
OF POOR QUALITY

Figure 3.7 TEM bright field image of an as extruded NiAl+1at.%Ta alloy.

ORIGINAL PAGE IS
OE POOR QUALITY

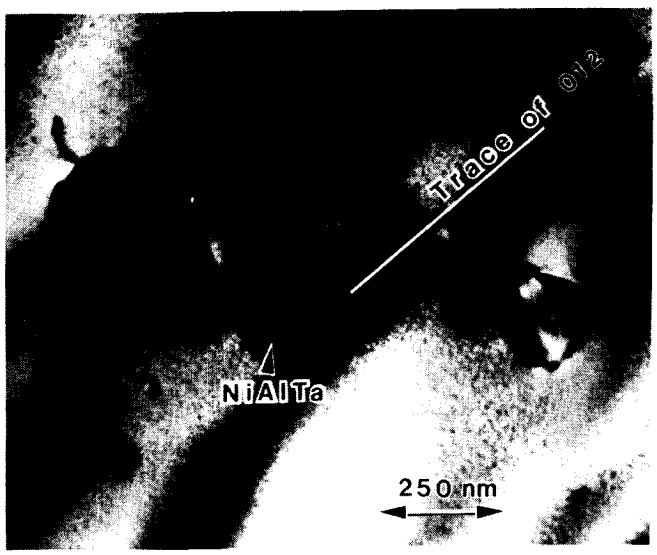

Figure 3.8 A bright field TEM micrograph of a compression tested specimen of NiAl+2at.%Ta alloy, viewed along a [100] direction in the matrix.

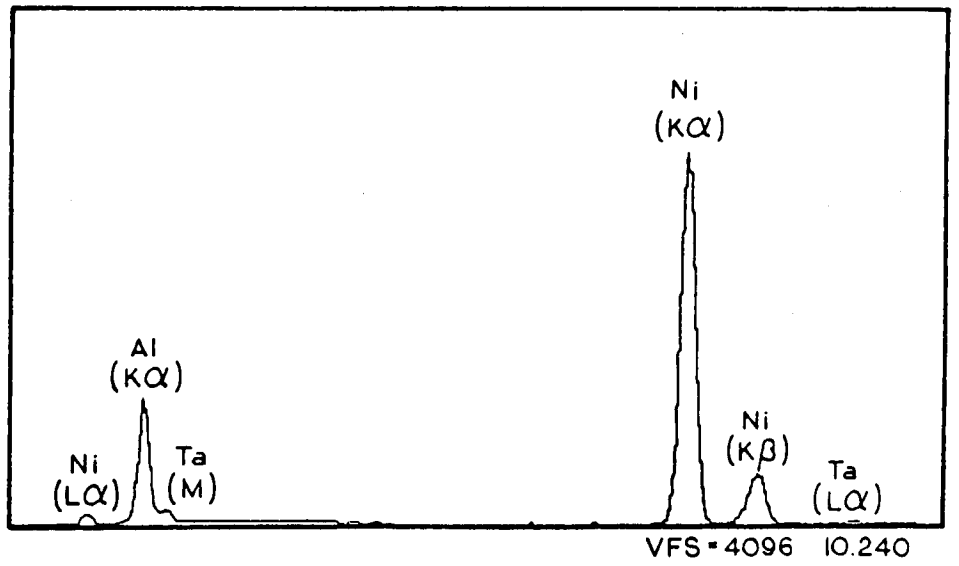

SPECTRUM FROM MATRIX

(a)

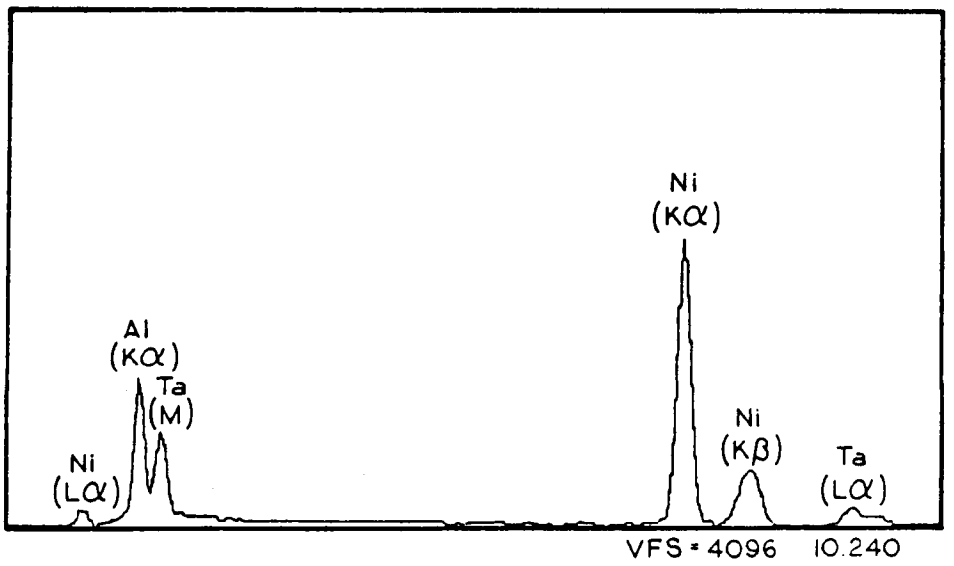

SPECTRUM FROM PRECIPITATE

(b)

Figure 3.9 EDS spectra from (a) the matrix and (b) the precipitate.

ORIGINAL PAGE IS
OF POOR QUALITY

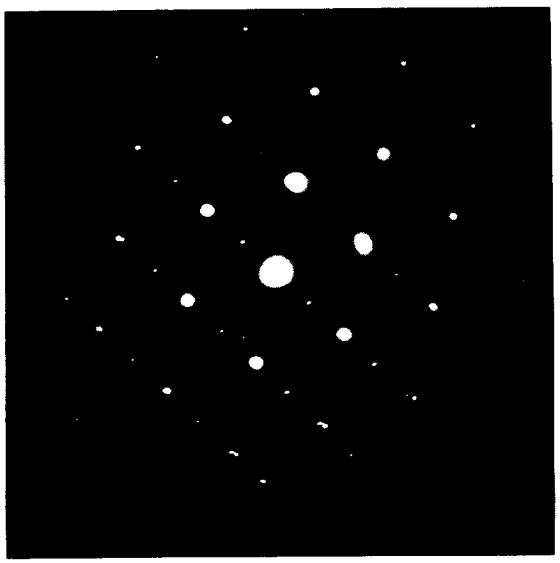

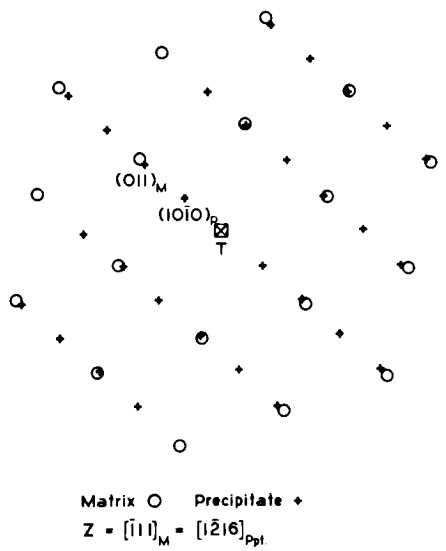

Figure 3.10 Observed and calculated composite SAD's with matrix zone axes parallel to the $[\bar{1}11]$ direction.

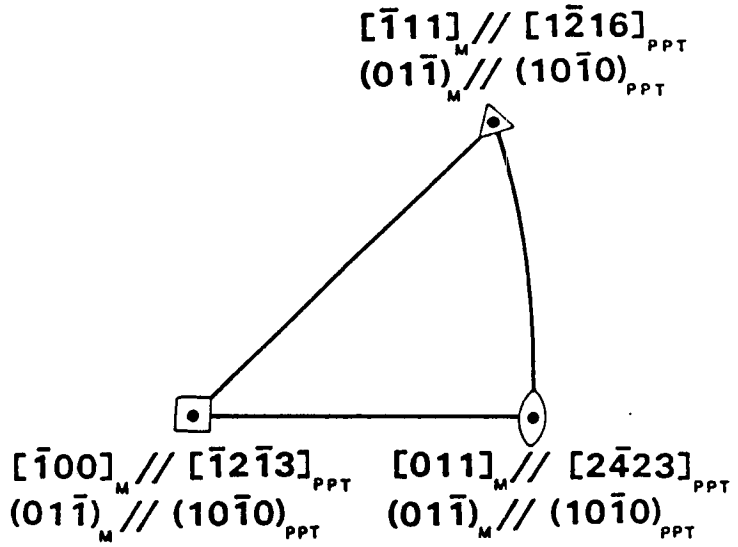

Figure 3.11 Orientation relationship between matrix and precipitate

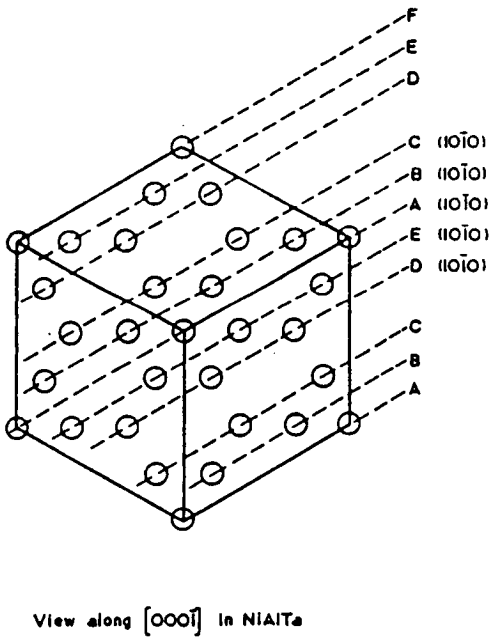

(a)

Figure 3.12 (a) Stacking of {10$\bar{1}$0} planes in NiAlTa and (b) an overlay of (011) planes of NiAl and combined E+A+B (10$\bar{1}$0) planes of NiAlTa.

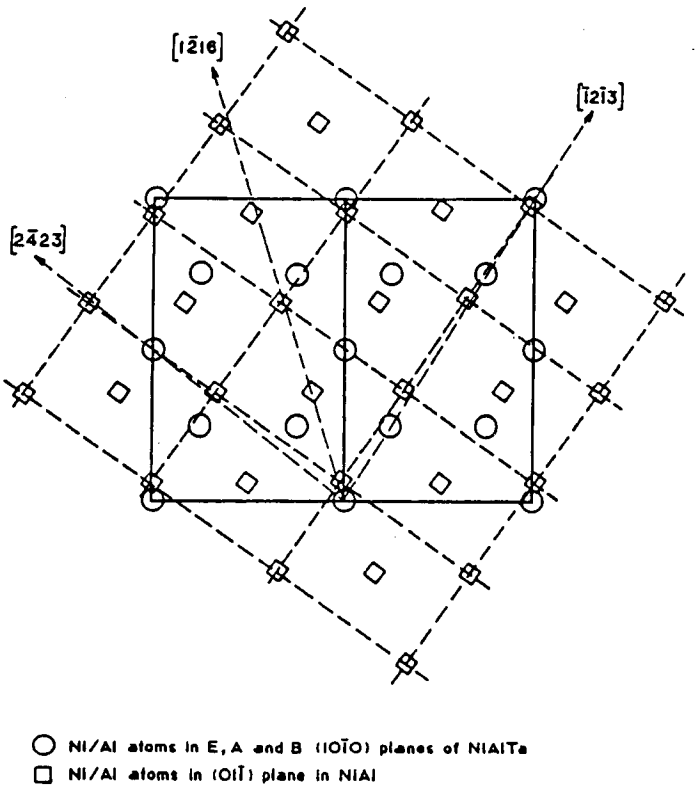

(b)

Figure 3.12 (a) Stacking of {10$\bar{1}$0} planes in NiAlTa and (b) an overlay of (011) planes of NiAl and combined E+A+B (10$\bar{1}$0) planes of NiAlTa.

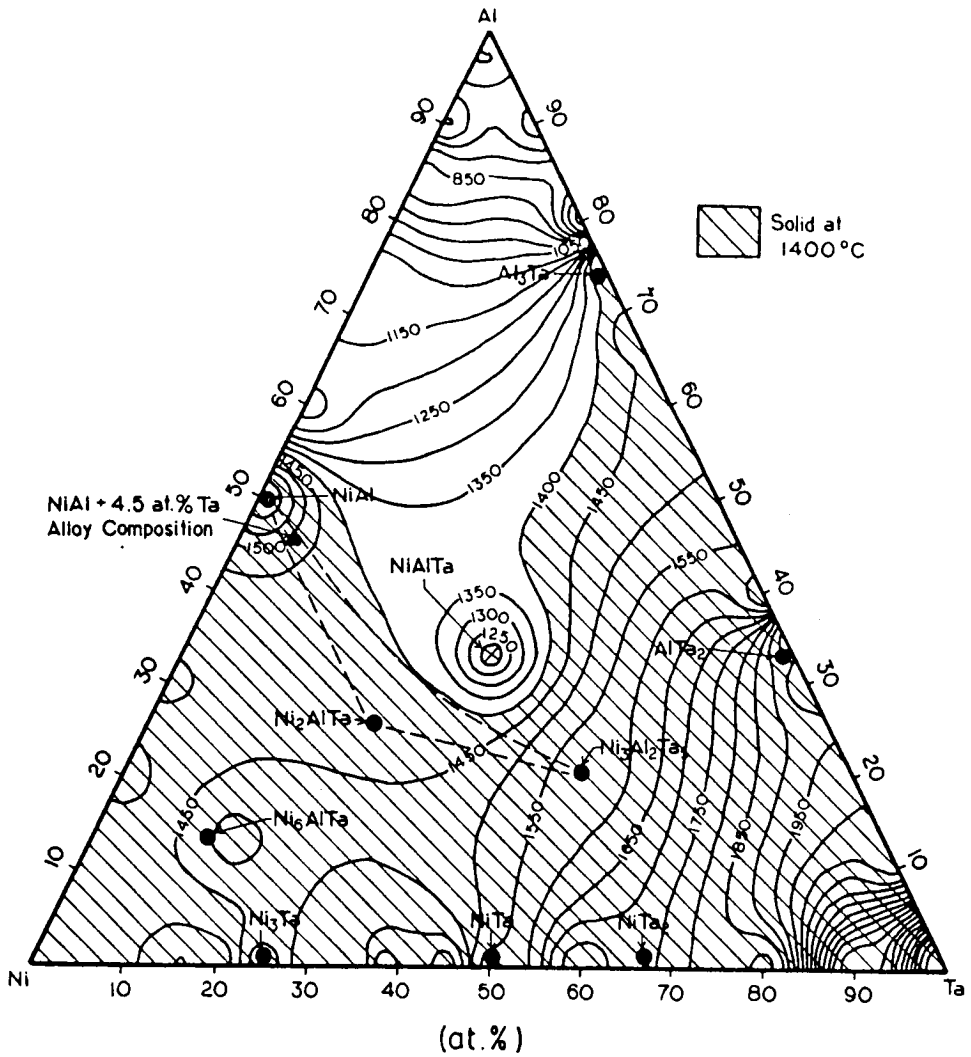

Figure 3.13 Solidus projection in Ni-Al-Ta system at a) 1673°K (1400°C) and b) 1773°K (1500°K).

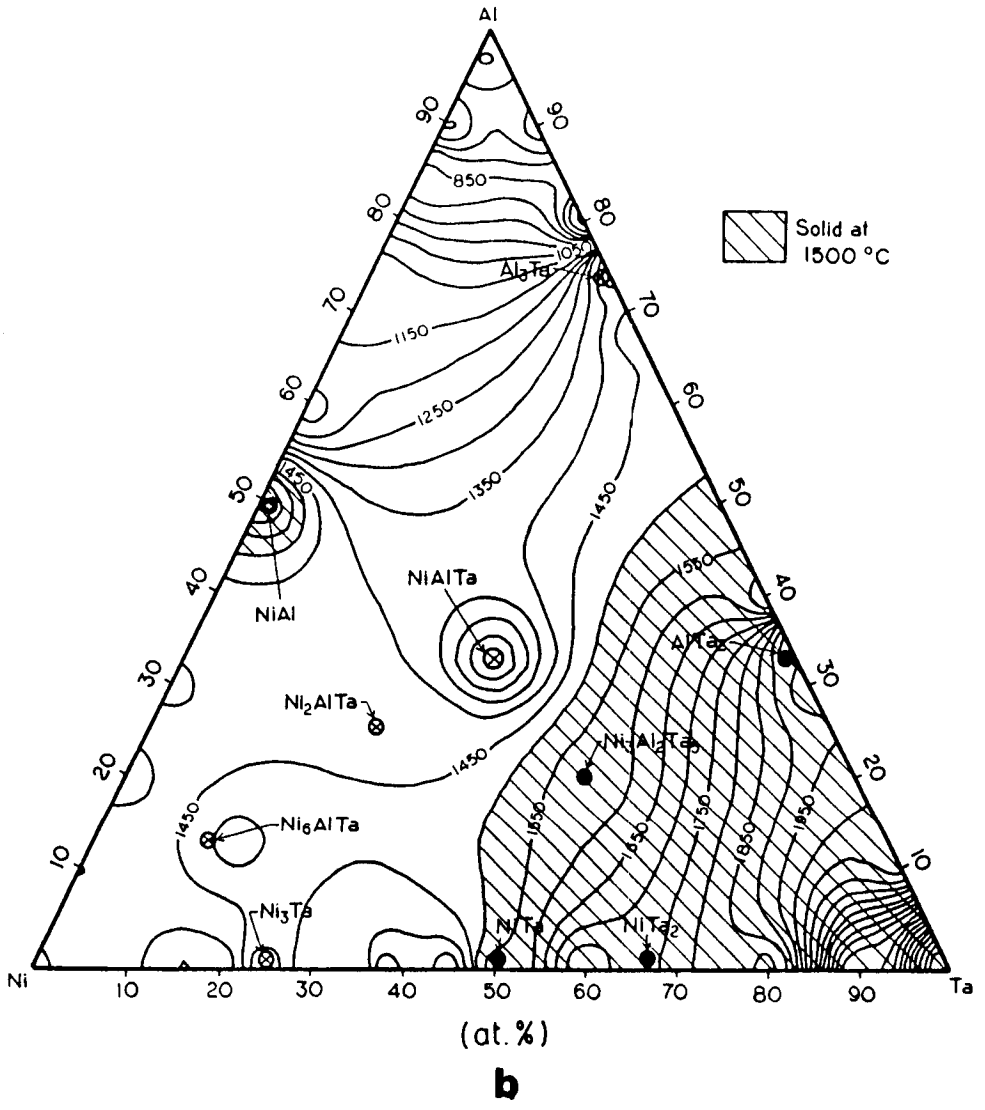

Figure 3.13 Solidus projection in Ni-Al-Ta system at a) 1673°K (1400°C) and b) 1773°K (1500°K).

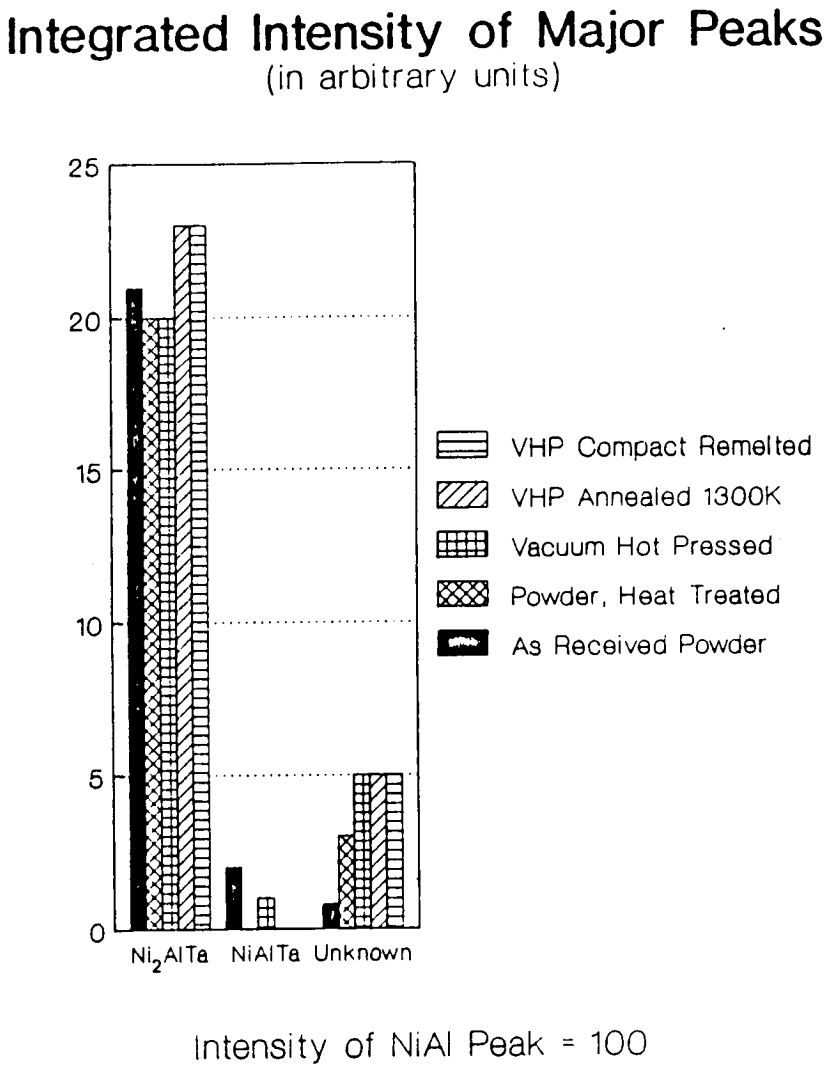

Figure 3.14 Relative integrated intensities of major peaks for NiAl+4.5at.%Ta alloy with different heat treatments.

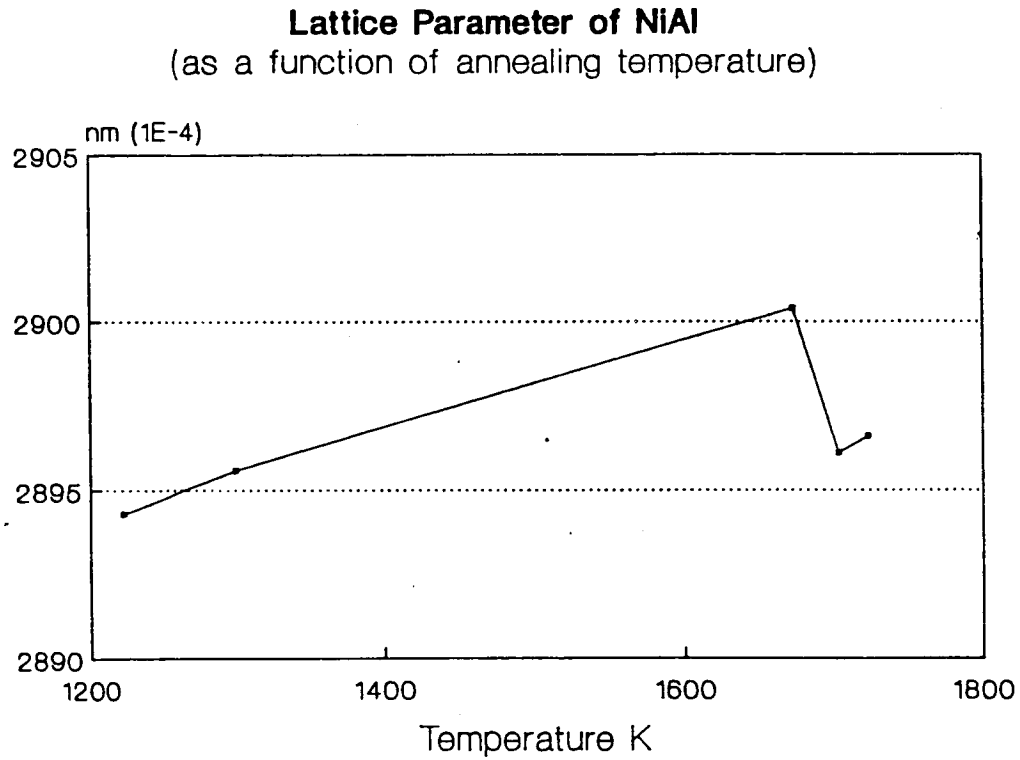

Figure 3.15 Change in the lattice parameter of NiAl as a function of temperature for the NiAl+4.5at.%Ta alloy.

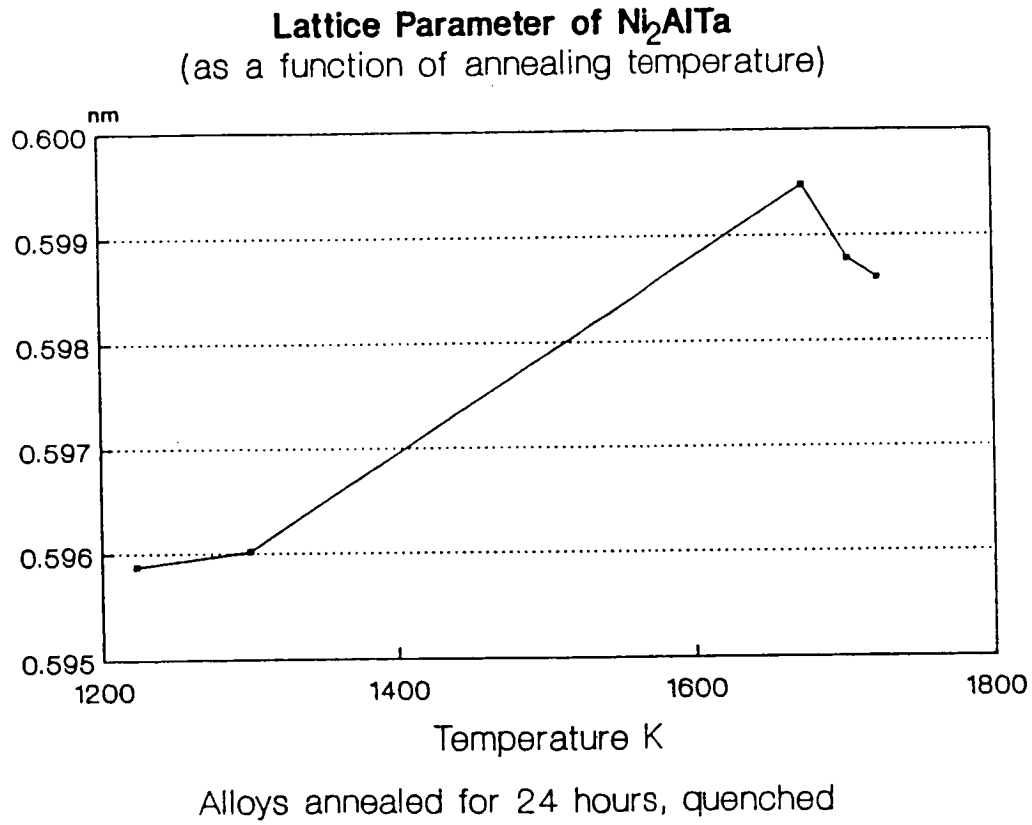

Figure 3.16 Change in the lattice parameter of Ni_2AlTa as a function of temperature for the NiAl+4.5at.%Ta alloy.

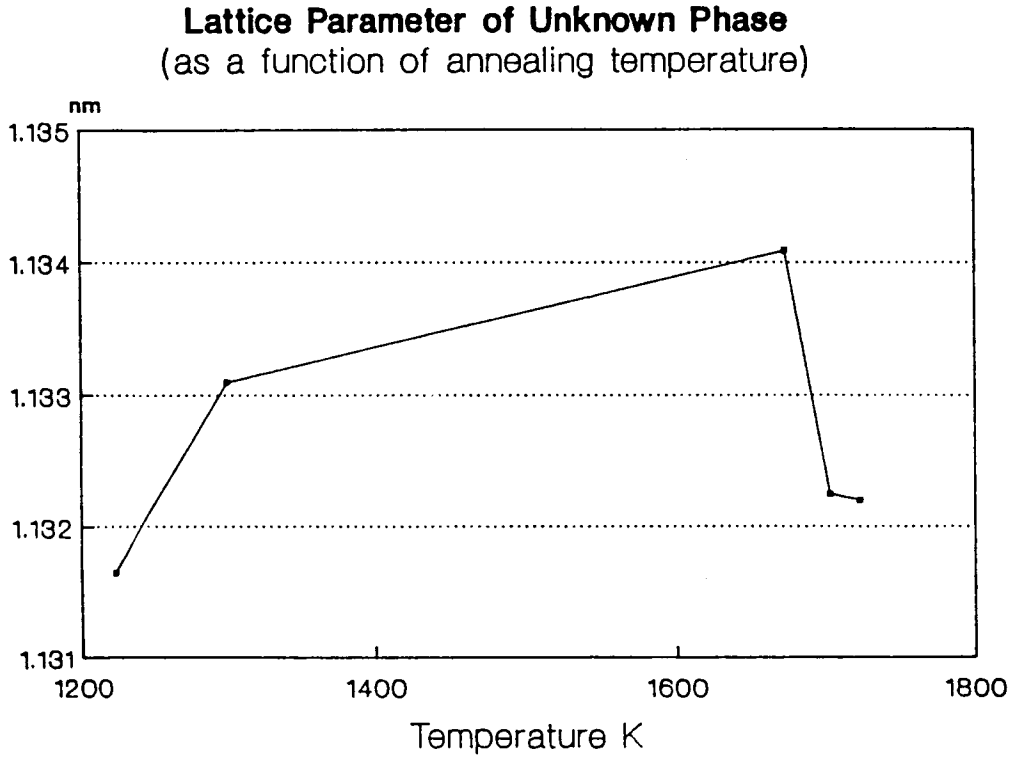

Figure 3.17 Change in the lattice parameter of the unknown phase ($Ta_5Ni_3Al_2$) as a function of temperature for the NiAl+4.5at.%Ta alloy.

ORIGINAL PAGE IS
OF POOR QUALITY

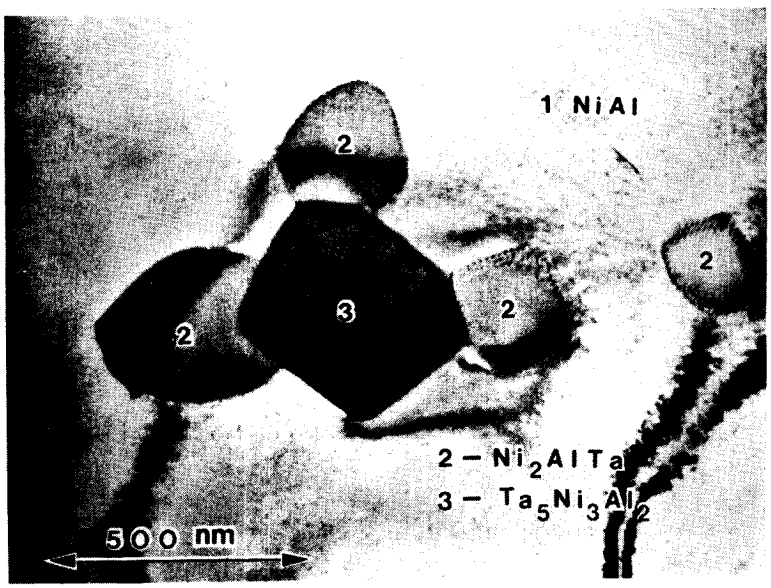

Figure 3.18 Bright field TEM micrograph of a cluster of phases found in NiAl+4.5at.%Ta alloy with heat treatment HT4.

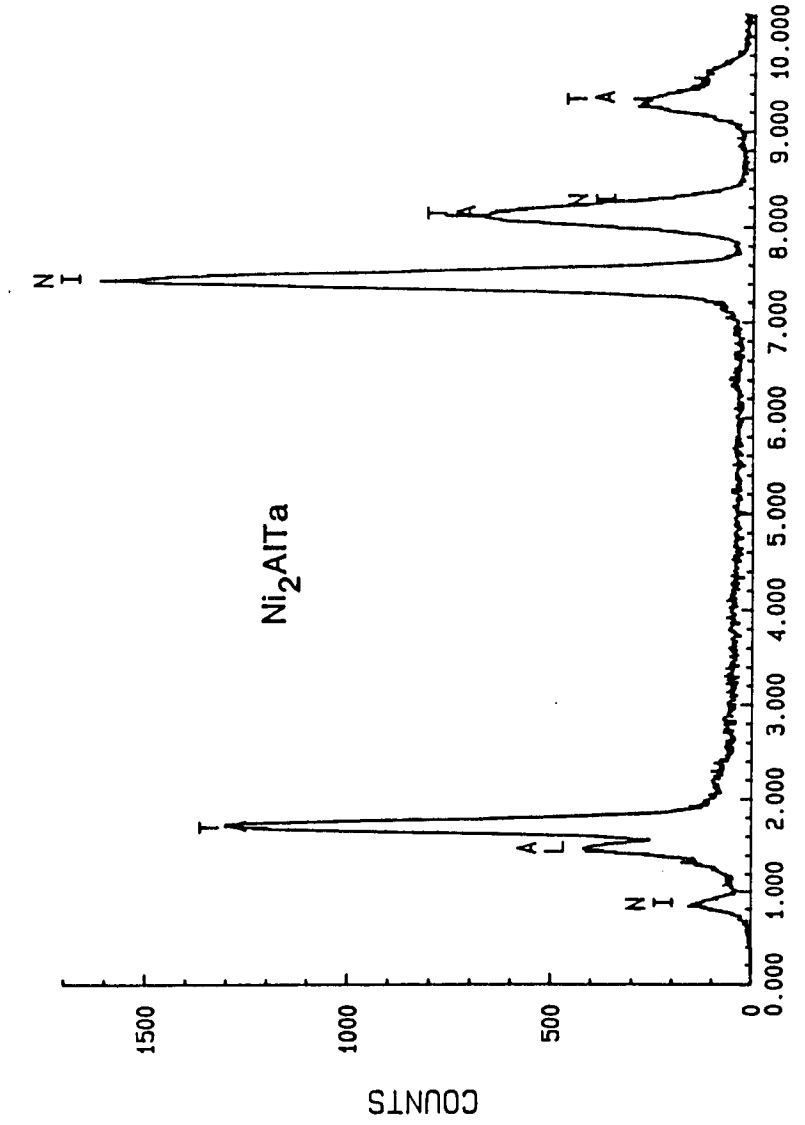

Figure 3.19 Example of an EDS spectrum from the Ni_2AlTa phase in NiAl+4.5at.%Ta alloy.

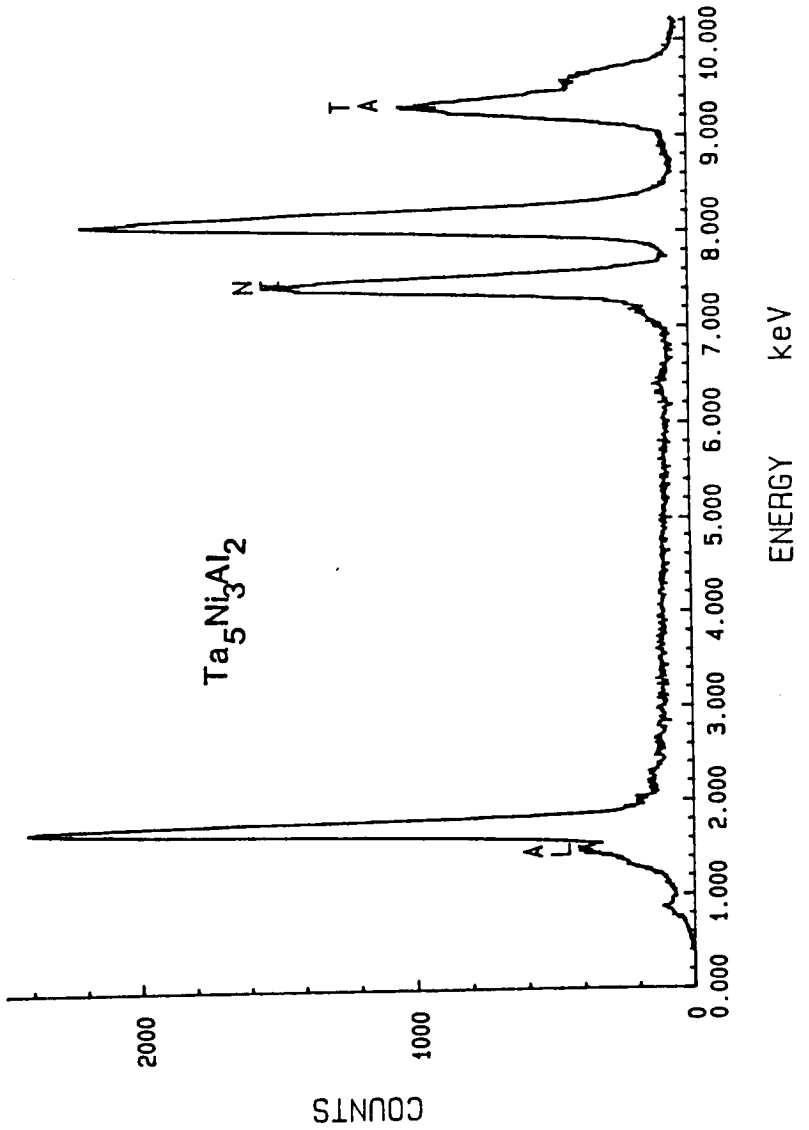

Figure 3.20 Example of an EDS spectrum from the unknown phase in NiAl+4.5at.%Ta alloy.

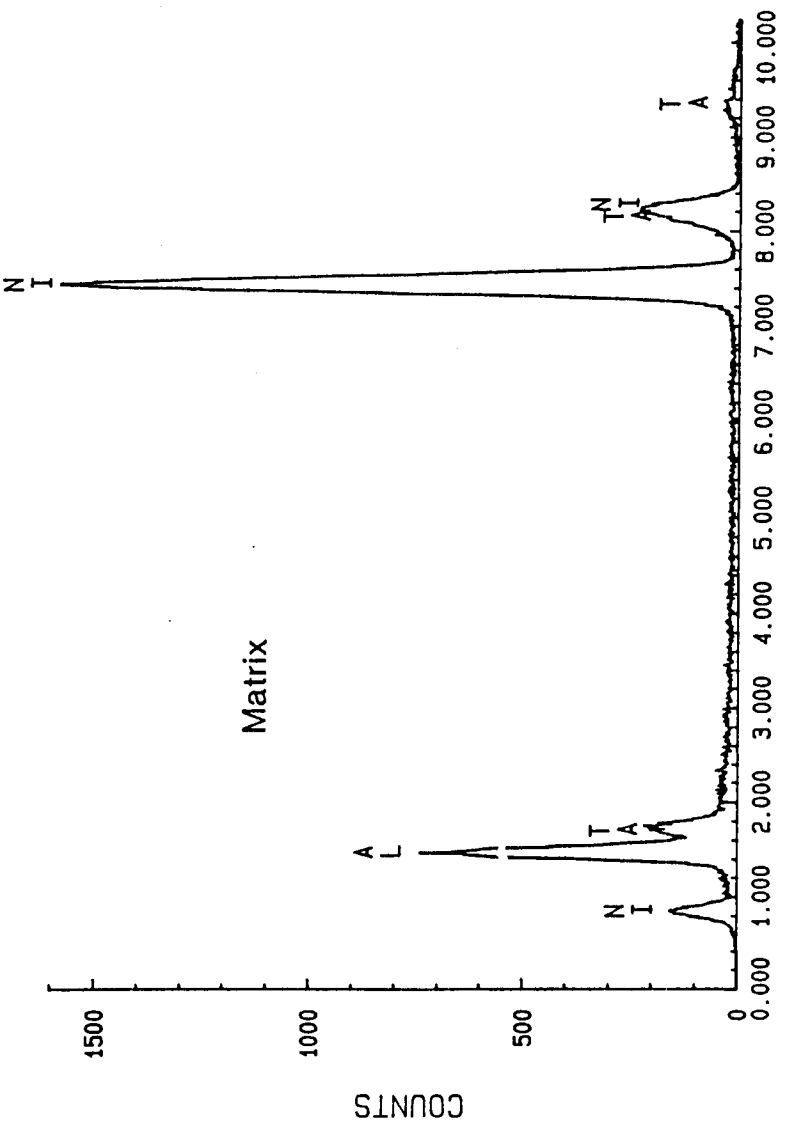

Figure 3.21 Example of an EDS spectrum from the matrix in NiAl+4.5at.%Ta alloy.

Figure 3.22 Electron diffraction patterns for the unknown phase taken with a camera length of 800 mm. These patterns could be indexed as $[\bar{1}12]$, $[\bar{1}22]$ and [012] zones of an ordered face centered cubic phase.

ORIGINAL PAGE IS
OF POOR QUALITY

ORIGINAL PAGE IS
OF POOR QUALITY

Figure 3.22 Electron diffraction patterns for the unknown phase taken with a camera length of 800 mm. These patterns could be indexed as $[\bar{1}12]$, $[\bar{1}22]$ and [012] zones of an ordered face centered cubic phase.

ORIGINAL PAGE IS
OF POOR QUALITY

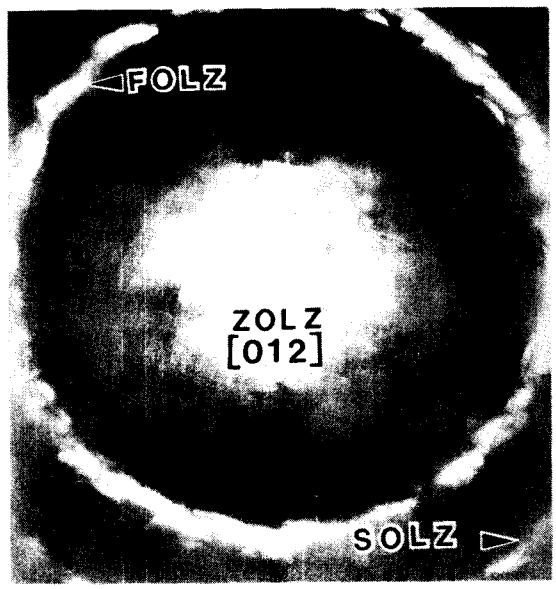

Figure 3.23 Convergent beam diffraction pattern (CBDP) with beam direction parallel to [012] of the unknown cubic phase.

ORIGINAL PAGE IS
OF POOR QUALITY

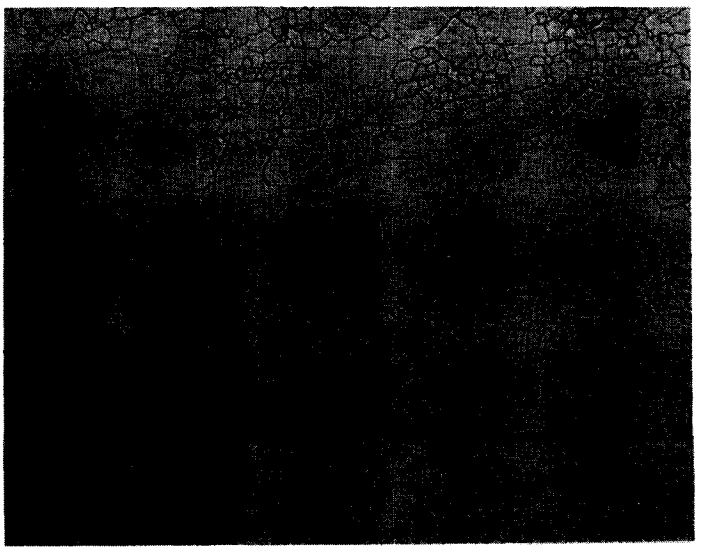

Figure 3.24 Abnormal grain growth in NiAl+1at.%Ta alloy annealed at 1473 ^{o}K for 72 hours.

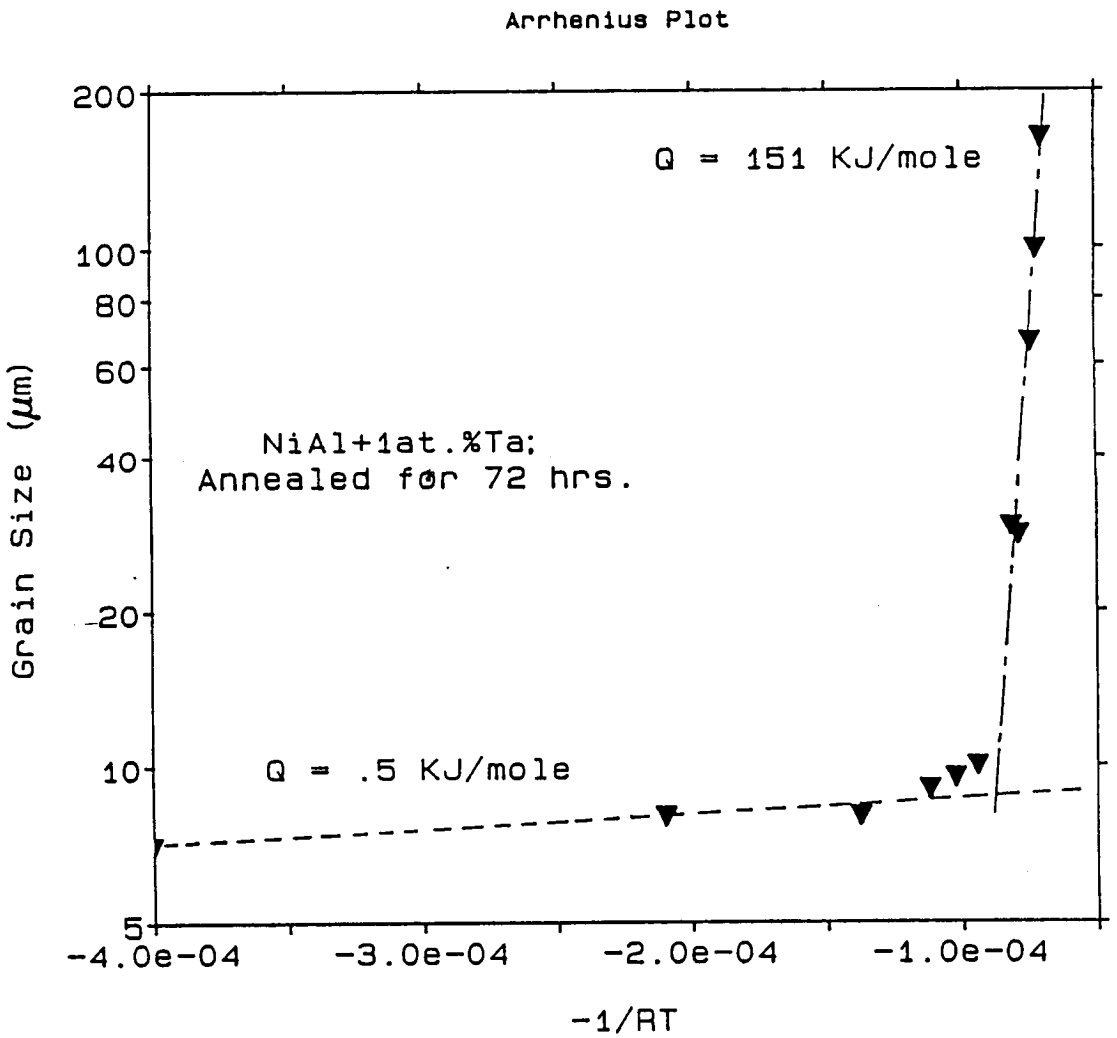

Figure 3.25 Arrhenius plot of grain size vs temperature

ORIGINAL PAGE IS
OF POOR QUALITY

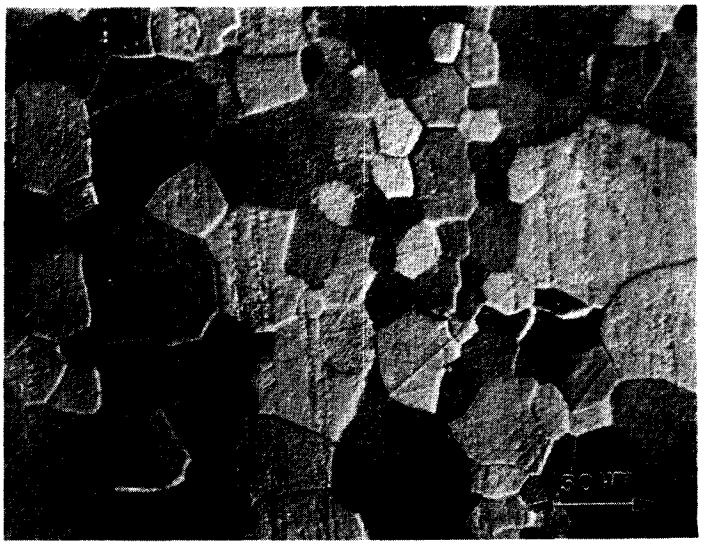

Figure 3.26 Longitudinal microstructure of NiAl+1at.%Ta alloy annealed at 1473 ^{o}K for 72 hours. The grain boundaries have migrated across the oxide stringers.

ORIGINAL PAGE IS
OF POOR QUALITY

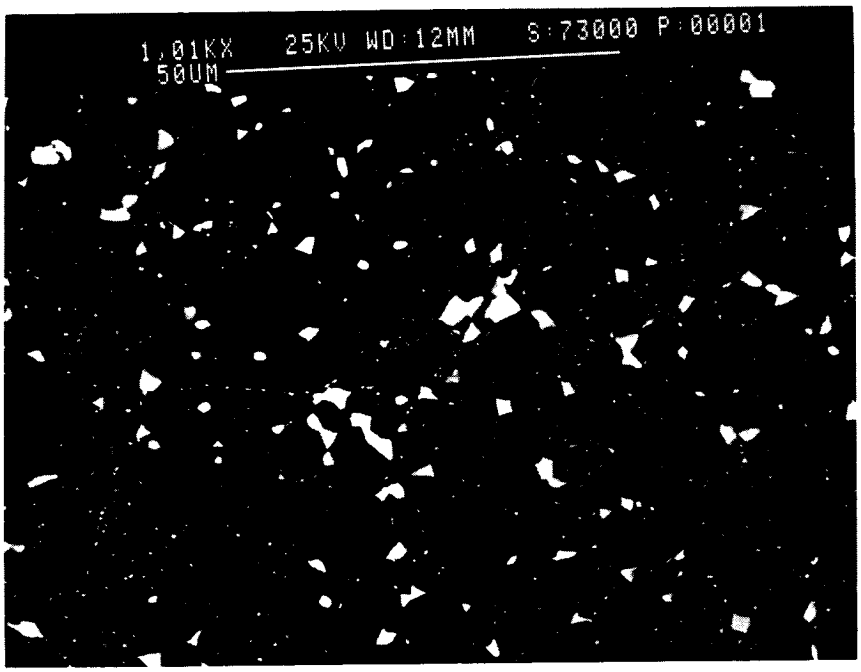

Figure 3.27 BSE image of as hot pressed NiAl+4.5at.%Ta alloy.

Table 3.1
Parameters for Thin Foil Preperation

Alloy	Etchant	Voltage	Temp.
NiAl+1at.%Ta	10% perchloric acid in ethenol	40 V	263 ^{o}K
NiAl+1at.%Ta	10% perchloric acid in ethenol	40 V	263 ^{o}K
NiAl+2at.%Ta	2:1 methenol + HNO_3	12 V	253 ^{o}K
NiAl+2at.%Nb	2:1 methenol + HNO_3	12 V	253 ^{o}K
NiAl+4.5at.%Ta	10% H_2SO_4 in methenol	25 V	268 ^{o}K

Table 3.2
Differential Thermal Analysis
Single Phase Powders
Rate of Heating / Cooling = 10°K / min.

Material	Treatment	Heat/Cool	Peak Temp.	Onset Temp.	Outset Temp.
NiAl	Powder	Heating	1908°K	1843°K	1936°K
		Cooling	1903°K	1914°K	1873°K
NiAl+1at.%Ta	Powder	Heating	1917°K	1855°K	1934°K
		Cooling	1892°K	1914°K	1856°K
NiAl+1at.%Ta	Powder annealed at 1223°K, 2 hrs.	Heating	1912°K	1808°K	1921°K
		Cooling	1887°K	1891°K	1870°K
NiAl+1at.%Nb	Powder	Heating	1914°K	1849°K	1929°K
		Cooling	1891°K	1900°K	1857°K

Table 3.3
Melting Behavior During Heating

Alloy	At.% Ni	Solidus	Liquidus	T
NiAl	54.37	1843°K	1908°K	65°K
NiAl+1at.%Ta	53.65	1855°K	1917°K	62°K
NiAl+1at.%Nb	54.09	1849°K	1914°K	65°K
NiAl+4.5at.%Ta	51.02	1842°K	1895°K	53°K

Table 3.4
NiAlTa Peaks Observed in X-ray Diffraction

Reflection	d nm (obs.)	d nm (cal.)	$I_{relative}$ (obs.)	$I_{relative}$ (cal.)
1 0 . 0	0.4245	0.4246	16	28
0 0 . 2	0.3967	0.3965	9	17
1 0 . 1	0.3744	0.3743	7	21
1 1 . 0	0.2454	0.2452	63	78
1 0 . 3	0.2244	0.2244	100	100
2 0 . 0	0.2119	0.2123	23	16
1 0 . 4	0.1796	0.1796	8	2
2 1 . 0	0.1604	0.1605	6	4
1 0 . 5	0.1487	0.1486	33	17
2 1 . 3	0.1372	0.1372	52	43
3 0 . 2	0.1334	0.1333	43	22
2 0 . 5	0.1273	0.1271	24	26
2 2 . 0	0.1226	0.1226	33	20

Table 3.5
Differential Thermal Analysis
Multi - Phase Powder
Rate of Heating / Cooling = 10°K / min.

Material	Treatment	Heat/Cool	Peak Temp.	Onset Temp.	Outset Temp.
NiAl+4.5at.%Ta	Powder	Heating	1719°K	1709°K	1728°K
		Heating	1801°K	1783°K	1813°K
		Heating	1895°K	1842°K	1915°K
		Cooling	1878°K	1897°K	1846°K
		Cooling	1692°K	1701°K	1671°K
NiAl+4.5at.%Ta	Powder annealed at 1223°K, 2 hrs.	Heating	1732°K	1701°K	1740°K
		Heating	1904°K	1854°K	1916°K
		Cooling	1687°K	1694°K	1675°K
		Cooling	1879°K	1894°K	1847°K
NiAl+4.5at.%Ta	Powder annealed at 1223°K, 2 hrs.	Heating[1]	1721°K	1684°K	1738°K
		Heating[1]	1903°K	1859°K	1911°K
		Cooling[1]	1694°K	1700°K	1684°K
		Cooling[1]	1885°K	1897°K	1858°K

1 Rate of heating and cooling = 5 °K / min.

Table 3.6
Results of X-ray Analysis

Alloy	Treatment[1]	Phases Present	Lattice Parameter (nm)
NiAl+1at.%Ta	As received prealloyed powder	NiAl	a_o = .2881±.0004
NiAl+1at.%Nb	As received prealloyed powder	NiAl	a_o = .2880±.0004
NiAl+2at.%Ta	Extruded at 1400°K and annealed at 1623°K for 100 hrs. Tested at 1300°K.	NiAl NiAlTa	a_o = .2884±.0004 a_o = .4903±.0013 c_o = .7929±.0029
NiAl+2at.%Nb	Extruded at 1400°K and annealed at 1623°K for 100 hrs. Tested at 1300°K.	NiAl NiAlNb[2]	
NiAl+4.5at.%Ta	As received prealloyed powder	NiAl Ni_2AlTa NiAlTa	a_o = .2891±.0001 a_o = .5939±.0011 a_o = .4881±.0013 c_o = .7917±.0022
NiAl+4.5at.%Ta	Powder annealed at 1300°K for 8 hrs. in hydrogen.	NiAl Ni_2AlTa $Ta_5Ni_3Al_2$	
NiAl+4.5at.%Ta	Vacuum hot pressed (VHP) at 1723°K 21 MPa, 6.5 hrs.	NiAl Ni_2AlTa $Ta_5Ni_3Al_2$ NiAlTa	a_o = .2894±.0003 a_o = .5945±.0029 a_o =1.1310±.0018 a_o = .4907±.0008 c_o = .7950±.0011

Table 3.6 (continued)
Results of X-ray Analysis

Alloy	Treatment[1]	Phases Present	Lattice Parameter (nm)
NiAl+4.5at.%Ta	VHP and then remelted.	NiAl	a_o = .2893±.0002
		Ni_2AlTa	a_o = .6035±.0024
		NiAlTa	a_o = .4893±.0021
			c_o = .7948±.0311
		$Ta_5Ni_3Al_2$	a_o =1.1266±.0092
NiAl+4.5at.%Ta	VHP and annealed at 1223°K for 24 hrs., quenched.	NiAl	a_o = .2894±.0001
		Ni_2AlTa	a_o = .5959±.0006
		$Ta_5Ni_3Al_2$	a_o =1.1317±.0007
NiAl+4.5at.%Ta	VHP and annealed at 1300°K for 24 hrs., quenched.	NiAl	a_o = .2896±.0001
		Ni_2AlTa	a_o = .5960±.0008
		$Ta_5Ni_3Al_2$	a_o =1.1331±.0009
NiAl+4.5at.%Ta	VHP and annealed at 1673°K for 24 hrs., quenched.	NiAl	a_o = .2900±.0002
		Ni_2AlTa	a_o = .5995±.0084
		$Ta_5Ni_3Al_2$	a_o =1.1341±.0011
NiAl+4.5at.%Ta	VHP and annealed at 1703°K for 24 hrs., quenched.	NiAl	a_o = .2896±.0002
		Ni_2AlTa	a_o = .5988±.0121
		$Ta_5Ni_3Al_2$	a_o =1.1323±.0009
NiAl+4.5at.%Ta	VHP and annealed at 1723°K for 24 hrs., quenched.	NiAl	a_o = .2897±.0003
		Ni_2AlTa	a_o = .5986±.0119
		$Ta_5Ni_3Al_2$	a_o =1.1322±.0009

Table 3.6 (continued)
Results of X-ray Analysis

Alloy	Treatment[1]	Phases Present	Lattice Parameter (nm)
NiAl+4.5at.%Ta	VHP; annealed at 1473°K, 8 hrs., 1523°K, 24 hrs.; 1300°K, 8 hrs.	NiAl Ni_2AlTa $Ta_5Ni_3Al_2$	
NiAl+4.5at.%Ta	VHP; annealed at 1523°K, 8 hrs., 1573°K, 24 hrs.; 1300°K, 8 hrs.	NiAl Ni_2AlTa $Ta_5Ni_3Al_2$	
NiAl+4.5at.%Ta	VHP; annealed at 1573°K, 8 hrs., 1623°K, 24 hrs.; 1300°K, 8 hrs.	NiAl Ni_2AlTa $Ta_5Ni_3Al_2$	
NiAl+4.5at.%Ta	VHP; annealed at 1623°K, 8 hrs., 1673°K, 24 hrs.; 1300°K, 8 hrs.	NiAl Ni_2AlTa $Ta_5Ni_3Al_2$	
NiAl+5at.%Ta	As cast	NiAl Ni_2AlTa NiAlTa	
NiAl+5at.%Ta	Cast and annealed at 1623°K, 8 hrs.; 1673°K, 24 hrs.; 1300°K, 8 hrs.	NiAl Ni_2AlTa NiAlTa	

1 All heat treatments in argon atmosphere unless otherwise noted.
2 SHERMAN and VEDULA (1987)

Table 3.7
SMTF Analysis of Ni_2AlTa

Element-Line	Intensity	K-Factor	Wt.%	At.%
Ni-K_α	15719	1.00	36.79	50.99
Al-K_α	2610	1.30	7.94	24.05
Ta-M	10046	2.35	55.26	24.96

Table 3.8
SMTF Analysis of the Unknown Phase

Element-Line	Intensity	K-Factor	Wt.%	At.%
Ni-K_α	14615	1.00	15.49	29.92
Al-K_α	3408	1.30	4.69	19.82
Ta-M	32057	2.35	79.82	50.26

Table 3.9
SMTF Analysis of the Matrix

Element-Line	Intensity	K-Factor	Wt.%	At.%
Ni-K_α	16063	1.00	59.22	46.58
Al-K_α	6129	1.30	29.37	50.49
Ta-M	1317	2.35	11.41	2.93

Table 3.10
Calculation of a_o from CBDP

Zone	R mm	G nm^{-1}	H nm^{-1}	a_o nm
FOLZ	37.0	15.0	3.825×10^{-2}	1.169
SOLZ	50.5	20.5	3.572×10^{-2}	1.252

Table 3.11
Indexing Peaks for the Unknown Phase in NiAl+4.5at.%Ta (1300 ^{o}K)

2 θ	$\sin^2 \theta$	s	$\lambda^2/4a_o^2$	a_o nm	h k l
31.42	0.0733	16	0.0046	1.297	4 0 0
34.36	0.0872	19	0.0046	1.295	3 3 1
38.73	0.1099	24	0.0046	1.297	4 2 2
41.25	0.1241	27	0.0046	1.293	5 1 1, 3 3 3
47.25	0.1606	35	0.0046	1.295	5 3 1
58.07	0.2356	51	0.0046	1.287	5 5 1, 7 1 1
67.53	0.3089	67	0.0046	1.289	7 3 3
72.03	0.3457	75	0.0046	1.289	7 5 1, 5 5 5

4. Creep

4.1 Literature Review

4.1.1 Diffusion Creep [Frost and Ashby (1982)]

A stress changes the chemical potential, ϕ, of atoms at the surface of grains in a polycrystal. A stress field with a deviatoric component changes ϕ on some grain surfaces more than the others, introducing a potential gradient, $\Delta\phi$. At high temperatures this gradient induces a diffusive flux of matter through and around the surfaces of the grains, and this flux leads to strain, provided it is coupled with sliding displacements in the plane of the boundaries themselves. Most models of the process [Nabarro (1948), Herring (1950), Coble (1963), Lifshitz (1963), Gibbs (1965), Raj and Ashby (1971)] assume that it is diffusion - controlled. They are in substantial agreement in predicting a rate equation. If both lattice and grain boundary diffusion are permitted, the rate equation for diffusional flow is:

$$\dot{\gamma} = \frac{42\ \tau\ \Omega}{k\ T\ d^2} D_v \left[1 + \frac{\pi\ \delta\ D_b}{d\ \ D_v} \right]$$

where $\dot{\gamma}$ = shear strain rate

τ = shear stress

d = grain size

D_v = volume diffusion coefficient

D_b = boundary diffusion coefficient

and δ = effective thickness of the boundary

At high temperatures, lattice diffusion controls the rate; the resulting flow is known as Nabarro-Herring creep and its rate scales as D_v/d^2. At lower temperatures, grain boundary diffusion takes over; the flow is then called Coble creep, and scales as D_b/d^3.

This equation is an oversimplification; it neglects the kinetics involved in detaching vacancies from grain-boundary sites and reattaching them again, which may be important under certain conditions. Such behavior can become important in alloys, particularly those containing a finely dispersed second phase.

4.1.2 Power Law Creep

The main focus in the investigation of creep behavior at high temperature is the understanding of the steady state or secondary creep state. Steady state creep data at intermediate stress levels are usually analyzed through the empirical power law relationship

$$\dot{\epsilon} = B\ \sigma^{n}\ (-Q_c/RT)$$

where the constant B combines all the stress and temperature independent terms from the previous equation and Q_c is the apparent activation energy for creep. ϵ and σ are strain rate and stress respectively. For simple systems Q_c is found to be equal to the self diffusion activation energy Q_{SD} [Sherby and Burke (1967), Weertman(1968), Mukherjee(1975)]. Accordingly evidence is strong for the creep of simple systems to be rate controlled by diffusional processes.

When creep data are fitted to power law, the typical value of the stress exponent n for fcc metals is 5 [Sherby and Burke (1967), Weertman(1968), Mukherjee (1975)]. For bcc and hcp metals, the measured values of n vary over a somewhat wider range from about 4 to 7 [Takeuchi and Argon (1976)]. For some solid solution alloys (called class I alloys) n decreses to a value of 3, while in other solid solution alloys (called class II alloys), n remains high at a value around 5.

In class I alloys, creep resistance is controlled by the solute drag forces on dislocations. Solute atmospheres develop around dislocations and deformation is controlled by the rate at which solutes can diffuse

along with the dislocation. Dislocation glide, not recovery, is the limiting step in the creep process. In a well annealed sample with a low dislocation density, the initial creep deformation rate is low. The creep gradually increases, as dislocations multiply, until steady state conditions are achieved. Configurations of multiple dislocations, in general, do not stabilize.

At high temperatures dislocations can climb as well as glide. If a gliding dislocation is held up by discrete obstacles, a little climb may release it, allowing it to glide to the next set of obstacles where the process is repeated. The glide step is responsible for almost all of the strain, although its average velocity is determined by the climb step. Mechanisms which are based on this climb-plus-glide sequence are called climb-controlled creep or dislocation creep or recovery creep and are used to describe the creep behavior of class II alloys and pure metals. In pure metals and class II alloys dislocation climb is much slower than glide. When two gliding dislocations interact, the resulting configuration is sufficiently stable that recovery will not usually occur before a third dislocation joins the configuration. Since the addition of a third dislocation stabilizes the configuration, the existing dislocation

network will increase in extent through subsequent dislocation interactions. In this way, an inhomogeneous distribution of dislocations or a subgrain network is developed [Nix (1986)]. The rate-controlling process for these mechanisms, at an atomic level, is the diffusive motion of single ions or vacancies to or from the climbing dislocations, rather than the activated glide of the dislocation itself.

4.1.3 High Temperature Plastic Deformation of NiAl

Even though a lot of work was done on high temperature plastic deformation of polycrystalline NiAl, most of it was using strain rates faster than $10^{-5}s^{-1}$. For example, Pascoe and Newey (1968) tested polycrystalline NiAl of various compositions in the temperature range of 77-1300°K with 10^{-4} s^{-1} strain rate. Vandervoort, Mukherjee and Dorn (1966) tested cast NiAl between 1073°K and 1748°K using strain rates of 10^{-3} to 10^{-5}. For the tests above 1448°K they observed a stress exponent of 3.3 to 3.7 and activation energies equal to those for diffusion. They have suggested Weertman's viscous glide mechanism as the dominant creep mechanism. This is rather surprising, since all the other work done on this material in the fast strain rate regime suggests

dislocation creep controlled by climb rather than viscous glide.

4.1.4 Creep of Polycrystalline NiAl

To qualify as creep, the deformation has to be at least slower than 10^{-5} s^{-1}. Yang and Dodd (1973) conducted constant load compression creep tests in pure argon atmosphere in the temperature range of 973°K to 1323°K. They observed n (stress exponent) values of 3.5 to 4.7 and Q (activation energy) values of 231 to 306 KJ/mole. They have attributed this variation in activation energy to the effect of stoichiometry. However, according to Whittenberger (1987a) for nickel-rich alloys this is just a statistical effect.

Jung et al (1986) have studied creep behavior of NiAl+Fe alloys. They found well-defined subgrains with 10 μm size in $(Ni_{.83}Fe_{.17})_{1.2}Al_{.8}$ alloy after slow compression test at 1173°K with a nominal strain rate of 10^{-7} s^{-1}. They also note a deviation of the observed creep from the power law of dislocation creep. They attribute it to an increased contribution of diffusion creep at slower strain rates.

The most recent and extensive work on creep of NiAl has been done by Whittenberger (1987a, 1987b, 1987c). He compression tested a series of small grain size, polycrystalline NiAl materials between 1200 and 1400°K and concluded that:

(i) Creep strength is independent of composition for Al/Ni≤1.03, and deformation can be adequetly described by a single stress exponent (5.75) and activation energy (314 KJ/mole).

(ii) For lower temperature, high strain rate conditions, creep is controlled by the formation of subgrains. Hence subgrain strengthening can be obtained for materials with grain size smaller than the predicted subgrain size.

(iii) For slower strain rates and higher temperature conditions diffusional creep mechanisms may be operative.

4.2 Experimental Procedure

4.2.1 Compression Creep

Figure 4.1 shows schematically the configuration of the test stage used for compressive creep testing. It was enclosed in a resistance heating furnace to carry out

creep tests in hot air. The load was transmitted to the specimen through SiC push bars. Pieces of tantalum foil, about 25 microns thick were inserted between the ends of the test specimens and push bars to prevent welding. It also reduced the friction between the specimen and the push bars. Temperatures were monitored through type R thermocouples wired to the top and the bottom of the test specimen. A third thermocouple recorded the nominal temperature in the furnace around the specimen. During testing, the temperature was maintained to within 1°K of the set point, and the difference between the three thermocouples never exceeded 2-3°K. Specimens were slowly heated to the set temperature over about 1.5 hour while a small stress (about 1.5-2.0 MPa) was applied by the weight of the upper push bar. This helped to maintain specimen alignment. After the specimen had reached the set temperature desired load was applied.

Constant load compression tests were performed at 1300°K in air. Since the value of total strain involved was very small (5% at the most for low stress region) we can assume the stress to be constant. Applied stress was thus calculated from applied load and the initial cross-sectional area of the specimen. Strain was calculated from displacement measured by a calibrated L.V.D.T. As

the specimen was compressed alumina rod #2 moved relative to rods 1 and 3 (see Figure 4.1). The relative motion was converted into electric current generated in a coil by induction. L.V.D.T. voltage was recorded on a strip chart recorder continuously. Tests were stopped after obtaining sufficient number of data points in the steady state creep regime. Steady state creep rate was calculated by fitting the strain readings vs time to a straight line. The value of the steady state creep rate (or the minimum creep rate) and the value of the initial applied stress was used in a composite log-log plot shown in a later section.

4.2.2 Slow Compression Test

Elevated temperature compression tests were conducted in air at 1200, 1300, and 1400°K. Testing was accomplished at constant crosshead velocities ranging from 2.12×10^{-2} to 2.12×10^{-5} mm s^{-1} in a universal testing machine. Arrangement of the test stage was similar to that for the creep test. Specimens were slowly heated to the set temperature over 2+ hours while a small stress (about 5 MPa) was applied by operating the test machine in the load cycle mode to retract the expanding push bars and to maintain specimen alignment.

Both stress and strain data were calculated from the load time charts. Strains were determined by subtracting the elastic region or directly from crosshead displacement when little elastic deformation could be seen. In general the calculated strain at the end of the test agreed well (+10%) with that determined by the measured change in length; however, for consistency, all calculated strains were normalized to the actual length change. The true stresses were computed on the basis of constancy of volume and uniform deformation. The value of the measured flow stress and the strain rate derived from these constant velosity tests were plotted on a log-log plot shown in a later section. Examples of typical curves used in both these tests is shown in Figure 4.2.

4.2.3 On the Equivalency of Compression Creep and Slow Compression Tests

Both, compression creep and slow compression tests give a stress value and a strain rate value. The results from both these tests are plotted on the same composite plot of strain rate vs stress. There has not been any systematic effort yet to test the equivalency of these two tests, even though, theoretically both should yield

the same values. Jensen and Tien (1985) have reported equivalency of the stress-strain and creep tests for the nickel based superalloy UDIMET 115 over a range of strain rates. In our experience, the results from both these tests are equivalent within a creep mechanism. The changes in mechanism, as indicated by the changes in slope of the composite curve, may occur at different points by using either of the two tests. Usually the tests in the faster strain rate regime were slow compression tests, where as the slower tests were compression creep tests.

4.3 Results

4.3.1 NiAl

There is no data in the literature on diffusion creep in NiAl. All the published work has been in the dislocation creep regime. In this study small grained (16 μm) NiAl was tested in compression at very low applied stresses. The results of these tests are presented in Table 4.1. Figure 4.3 shows a plot of shear strain rate vs shear stress on a log-log scale, for NiAl tested at 1300°K. Normal stress was converted to shear stress by dividing by $3^{\frac{1}{2}}$ and the normal strain rate was converted

to shear strain rate by multiplying by the same constant. The grain size after testing was 23 μm for the longest test. A stress exponent of ~2 was obtained. Figure 4.4 shows the Arrhenius plot for material tested at 5 MPa normal stress. The value of Q, the activation energy for diffusional flow obtained from the plot is 297 kJ/mole and compares well with 314 kJ/mole obtained by Whittenberger (1987) for dislocation creep.

4.3.2 NiAl+1at.%Ta and NiAl+1at.%Nb

Figures 3.7 and 4.6 show the microstructure of NiAl+1at.%Ta and NiAl+1at.%Nb alloys in the as extruded condition. The volume fraction of second phase particles is very low. Also the interparticle distance is large. Thus these two alloys can be termed as single phase alloys. Figure 4.6 shows the composite plot of minimum creep rate at 1300°K (~0.68 T_m) as a function of applied stress (or flow stress in the case of slow compression tests) for NiAl + Ta alloys. The corresponding data is presented in Table 4.2. All the data for NiAl above 10 MPa is from the work of Whittenberger (1987a). In this figure a few data points from tests at 1200°K and 1400°K have been converted to 1300°K by using the relation

$$\frac{\dot{\epsilon}_1}{\dot{\epsilon}_2} = \frac{\exp(-Q/RT)}{\exp(-Q/RT)}$$

At strain rates greater than 10^{-6} s^{-1}, the stress exponent n in the equation

$$\dot{\epsilon} = B\ \sigma^n\ \exp\ (-Q/RT)$$

was 4.6 for NiAl+1at.%Ta and 4.25 for NiAl+1at.%Nb (See Table 4.4 for the other parameters). Whittenberger (1987a) has observed a stress exponent of 5 to 6 in NiAl. He has explained the exponent of 5 in terms of the theory presented by Sherby et al. (1977). According to that theory the subgrain size, λ, can have a profound effect on steady state creep rate

$$\dot{\epsilon} \propto (\lambda/b)^3\ (\sigma/E)^8\ D_{eff}$$

where b = Burger's vector

E = Dynamic elastic modulus

D_{eff}= Effective diffusion coefficient

Because

$$\lambda \propto (E/\sigma)$$

$$\dot{\epsilon} \propto (\sigma/E)^5\ D_{eff}$$

Subgrains have been observed in NiAl at higher strain rates and lower temperture [Whittenberger (1987), Ball & Smallman (1966)]. However, Whittenberger did not observe any subgrains at slow strain rate (2 x 10-7s-1)

specimens tested at 1300 and 1400°K. In this study also no well defined subgrains were observed in a NiAl+1at.%Nb alloy tested at 1300°K with a stress of 60 MPa. So the behavior of the 1% alloys is similar to that of NiAl, however, no subgrains were observed due to the high temperature of testing and lower grain size of the 1% alloys. At high temperature the dislocations are more mobile and with smaller grain size the grain boundaries can act as dislocation sinks more effectively.

At higher stresses the alloys had higher creep strength compared to pure NiAl. However at slower strain rates diffusional creep mechanisms dominate and the smaller grained 1% alloys become weaker than NiAl. The stress exponent also gradually changes and moves towards 1, the stress exponent of diffusional creep.

The increase in the creep strength of NiAl at higher stresses could be due to strengthening obtained from solid solution alloying or increase in the modulus or both.

Figure 4.7 shows minimum creep rate at 1300°K vs stress behavior for NiAl+Nb alloys (Also see Table 4.3). It is similar to alloys containing tantalum, even though,

on a weaker side. However, one interesting feature ws observed in NiAl+1at.%Nb alloy. When it was given a heat treatment consisting of 2 hrs. at 1523°K and 10 hrs. at 1300°K (test temperature), its creep properties improved remarkably. Figure 4.8 shows the microstructure of the alloy after the heat treatment. The increase in strength could be linked with the precipitation observed. All the precipitates were niobium-rich and contained silicon as impurity. No such effect was observed for alloys containing 1% tantalum.

4.3.3 NiAl+2at.%Ta and NiAl+2at.%Nb

Figure 4.9 shows the TEM dark field image of NiAl+2at.%Nb alloy after the heat treatment. Alloys with 2 at.% addition were extruded from blended powders and hence were given a 100 hour homogenization anneal at 1623°K. The microstructure of NiAl+2at.%Ta after the same heat treatment is shown in Figure 4.10. From both these figures it is apparent that these alloys have a higher volume fraction of precipitates compared to alloys with 1at.% tantalum or niobium and the interparticle distance is very small too. However, since these alloys were prepared from blended powders the distribution of second phase was not uniform. The regions shown in Figures 4.9

and 4.10 are the regions with the highest density of second phase precipitates. Figures 4.6 and 4.7 show the creep behavior of these two alloys, which show remarkable improvement over binary NiAl and NiAl+1at.% alloys. Corresponding data is presented in Tables 4.5 and 4.6. Figure 4.11 shows the microstructure of NiAl+2at.%Ta alloy after slow compression testing at 1300°K with a nominal strain rate of 6 X 10^{-6} s^{-1}. Clear dislocation precipitate interaction can be seen. A similar microstructure was observed for tested NiAl+2at.%Nb alloy. Stress exponents of 2.59 and 3.46 were obtained for NiAl+2%Ta and NiAl+2at.%Nb alloys respectively.

4.3.4 NiAl+4.5at.%Ta

Figure 3.27 shows the back scattered electron image of a hot pressed alloy. The tantalum rich precipitates are distributed in the matrix and at the grain boundaries as well. Creep behavior of the alloy is shown in the composite plot of Figure 4.13 and the corresponding data is presented in Table 4.7. Again because of the second phase precipitates the creep strength relative to pure NiAl or NiAl+1at.%Ta alloy has improved.

4.3.5 Effect of Heat Treatment

In order to get improved creep properties it is important to get uniform distribution of fine second phase precipitates. One way of doing this is to dissolve the second phase precipitates by suitable solutionizing treatment and then to re-precipitate them by a lower temperature anneal. The various heat treatments given to this vacuum hot pressed alloy are listed in Table 4.8. The heat treatments were given in three steps. First, there was an 8 hour anneal to 50°K below the desired temperature to remove local segregation. Second, a 24 hour anneal at the desired tempreature. Third, an 8 hour anneal at the test temperature to get a stable microstructure during the test. Table 4.7 lists the creep rates obtained after the heat treatments. The only significant improvement was observed after the heat treatment #4 at 1673°K. Figure 4.14 shows the BSE image of the alloy after HT4, and comparison with Figure 4.12 clearly shows the difference in the distribution. Figure 4.15 shows a TEM bright field micrograph of the same alloy. Precipitation at the grain boundaries and in the matrix can be seen. Figure 4.16 shows the dislocations in the matrix of alloys. Even after extensive annealing the dislocations are being pinned by the precipitates.

This fact is again illustrated in Figure 4.17 which shows the microstructure of a heat treated alloy after testing. Dislocation arrays and newtorks stabilized by precipitates can be clearly seen. However they are not as continuous to be called subgrains.

4.3.6 NiAl+5at.%Ta Cast Alloy

This alloy was also given heat treatment #4 (HT4) before testing. After the heat treatment the interdendritic segregation, common to cast materials, disappeared. An uniform distribution of fine second phase precipitates was obtained, as can be seen in Figure 4.18. Of all the alloys tested this alloy showed the most remarkable improvement over pure NiAl. The results are presented in Table 4.9 and shown in Figure 4.13. A stress exponenent of 3.71 was obtained.

4.4 Discussion

In describing creep of NiAl Whittenberger (1987) has noted that although subgrain strengthening appears to be a major factor, due to the high test temperatures and small grain size of the materials, diffusional creep mechanisms could also be expected to contribute to the

observed deformation rate. Observations in this study support that. Our data for NiAl tested at 1300°K with stresses lower than 10 MPa does indicate a dominance of diffusional flow mechanism, even though it is not pure diffusional creep.

Alloys with 1 at.% tantalum or niobium, although strengthened by solid solution, are weaker than pure NiAl in the very low strain rate regime due to their smaller grain size (8-9 μm) compared to pure NiAl (16 μm). This is consistent with the diffusional flow. Also it is important to note that subgrains were not observed in alloys tested at 60 MPa and which showed a strain rate of 10^{-5} s^{-1}.

The inhibition of diffusional creep by the presence of a second phase has been clearly demonstrated by Harris et al. (1969), who creep-tested sintered Mg powder which contained dispersed particles of MgO. Reduction in power-law creep may be achieved by metallurgical control designed to slow both glide and climb [Ashby (1973)]. Solute and particle strengthening may reduce the former. Climb is slowed by alloying which lowers the diffusivity, lowers the stacking-fault energy and which introduces an internal or threshold stress. A grain-boundary

precipitate wil also have the effect of pegging the boundaries and thus suppressing grain-boundary sliding.

NiAl+2at.%Ta, NiAl+2at.%Nb and NiAl+4.5at.%Ta alloys which have significant amounts of second phase particles show substantial improvement over pure NiAl due to lowering of both diffusional and dislocation creep. Since both the mechanisms are operative the stress exponent does not show a value of 1 (characteristic of diffusional creep) or 5 (characteristic of dislocation creep); it rather shows a value in between. Such values of n have been observed in a two phase alloy with Ni_2AlTi matrix and NiAl precipitates [Polvani, Tzeng and Strutt (1976)].

The cast material, which has both higher grain size of 75 μm (good for diffusional creep and a distribution of fine second phase precipitates (good for both diffusional and dislocation creep) shows the best improvement over pure NiAl.

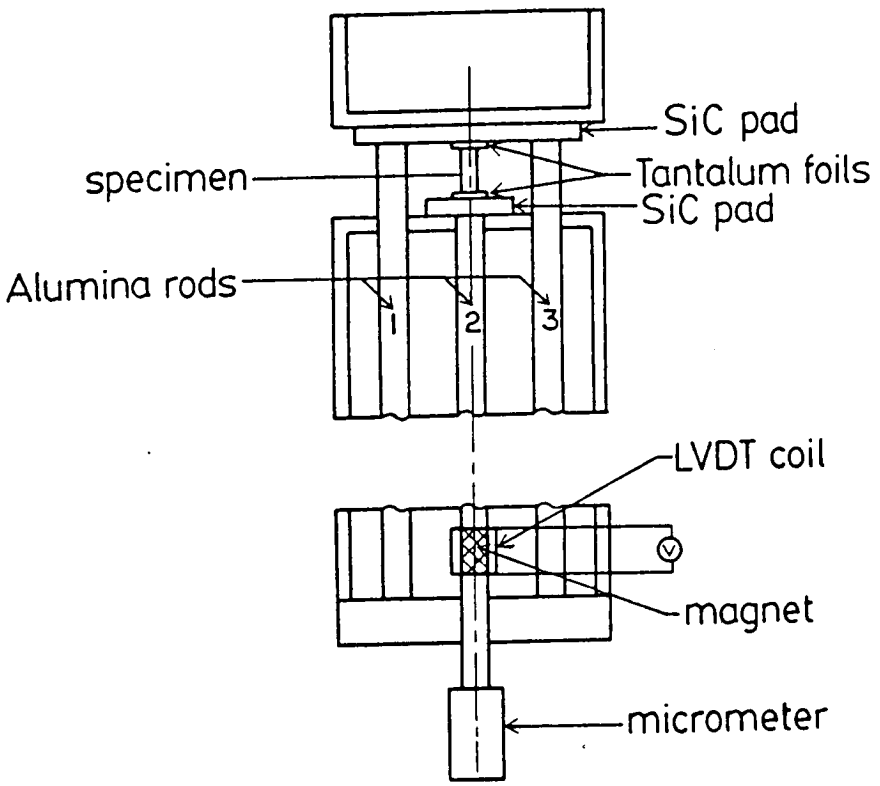

Figure 4.1 Configuration of the test stage used for compression creep.

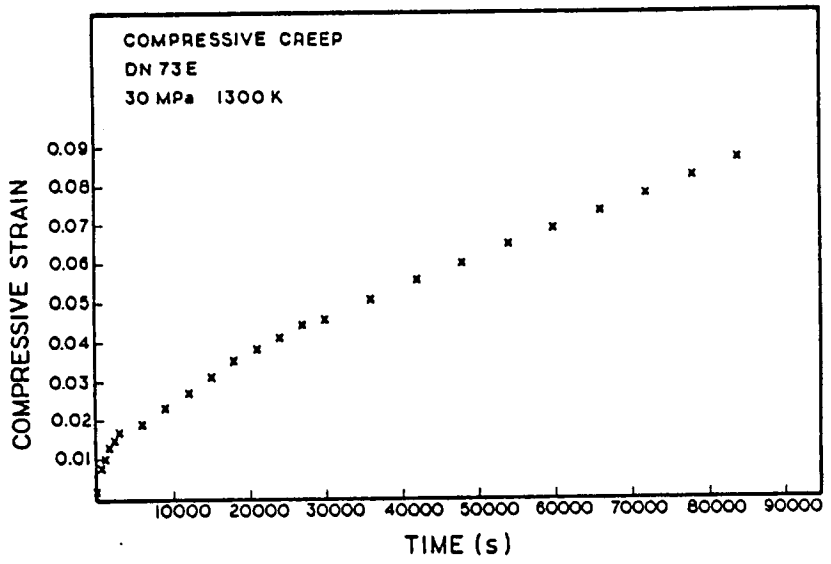

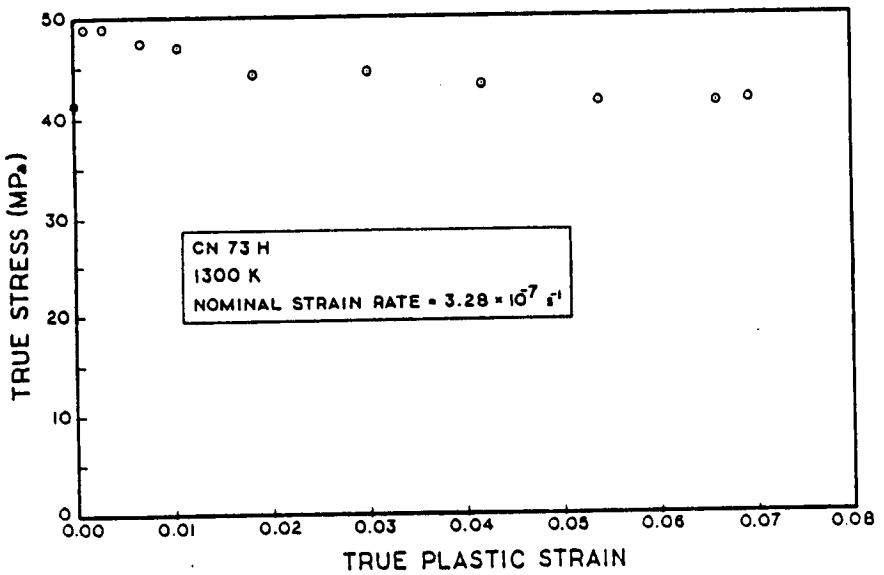

Figure 4.2 Typical curves obtained from the compression creep and the slow compression tests.

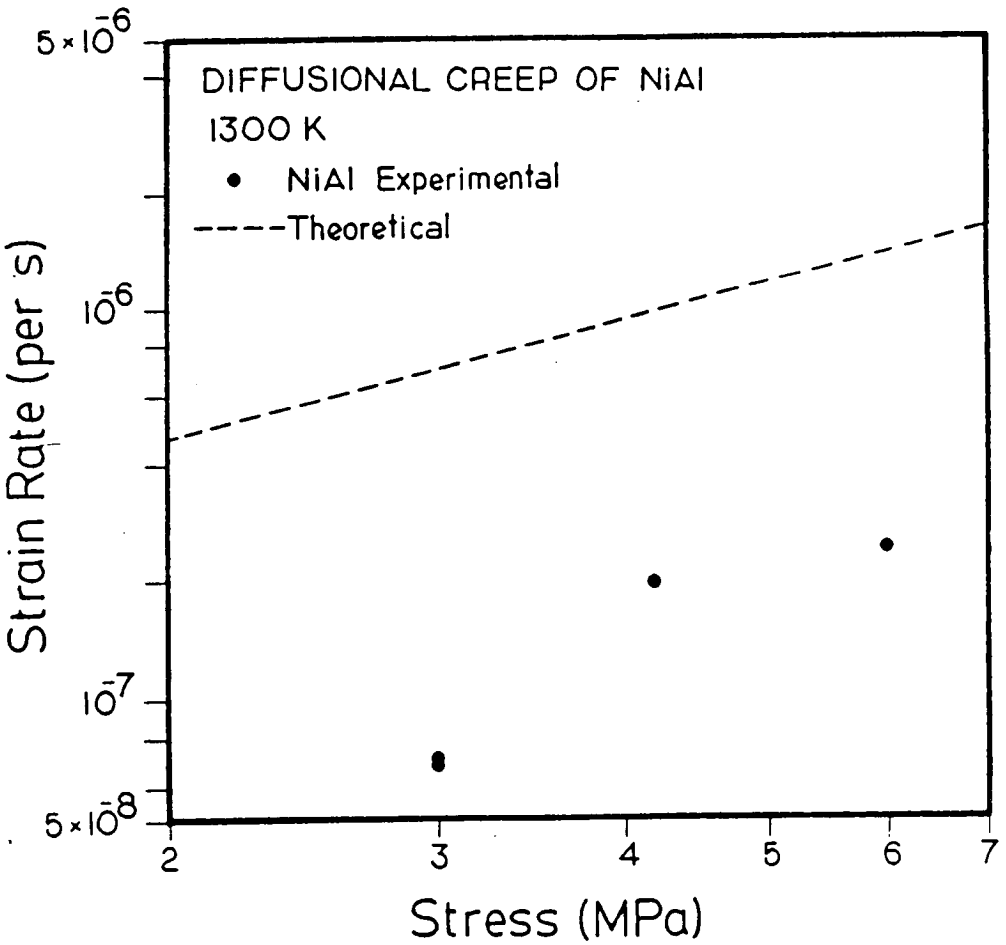

Figure 4.3 Compressive Creep of NiAl at 1300 ^{o}K

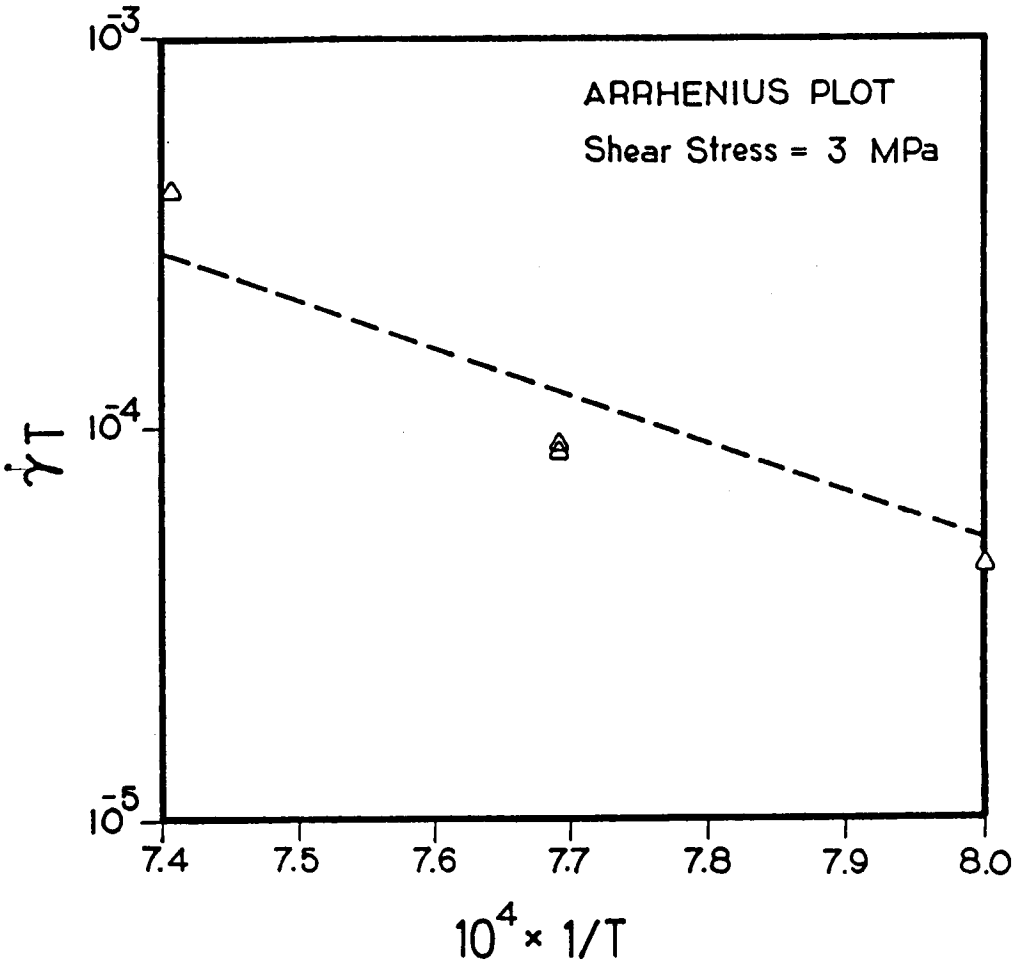

Figure 4.4 Arrhenius Plot for NiAl tested at 5 MPa normal stress.

ORIGINAL PAGE IS
OF POOR QUALITY

Figure 4.5 TEM bright field image of an as extruded NiAl+1at.% Nb alloy.

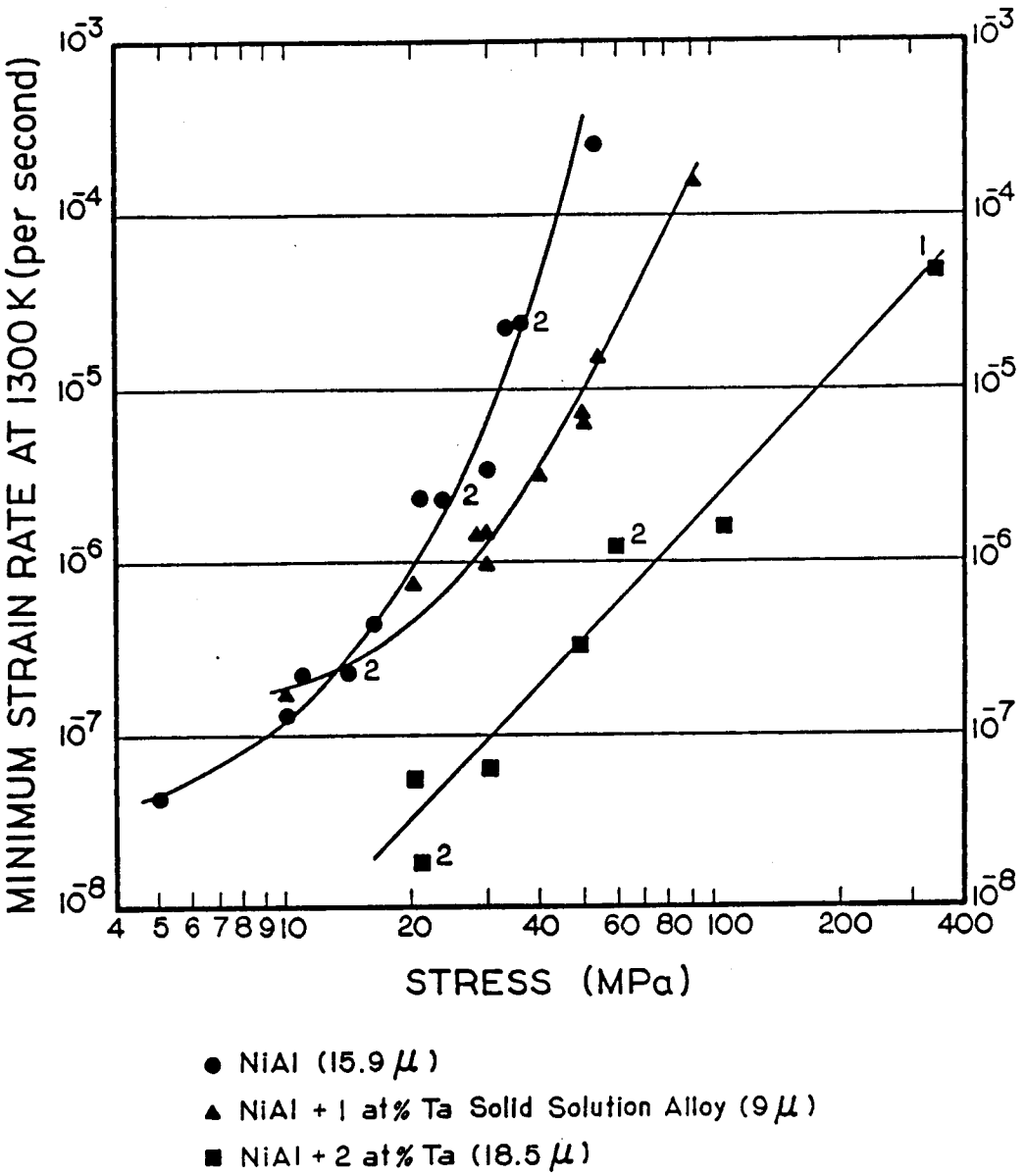

Figure 4.6 Creep of NiAl + Ta alloys at 1300 ^{o}K in compression.

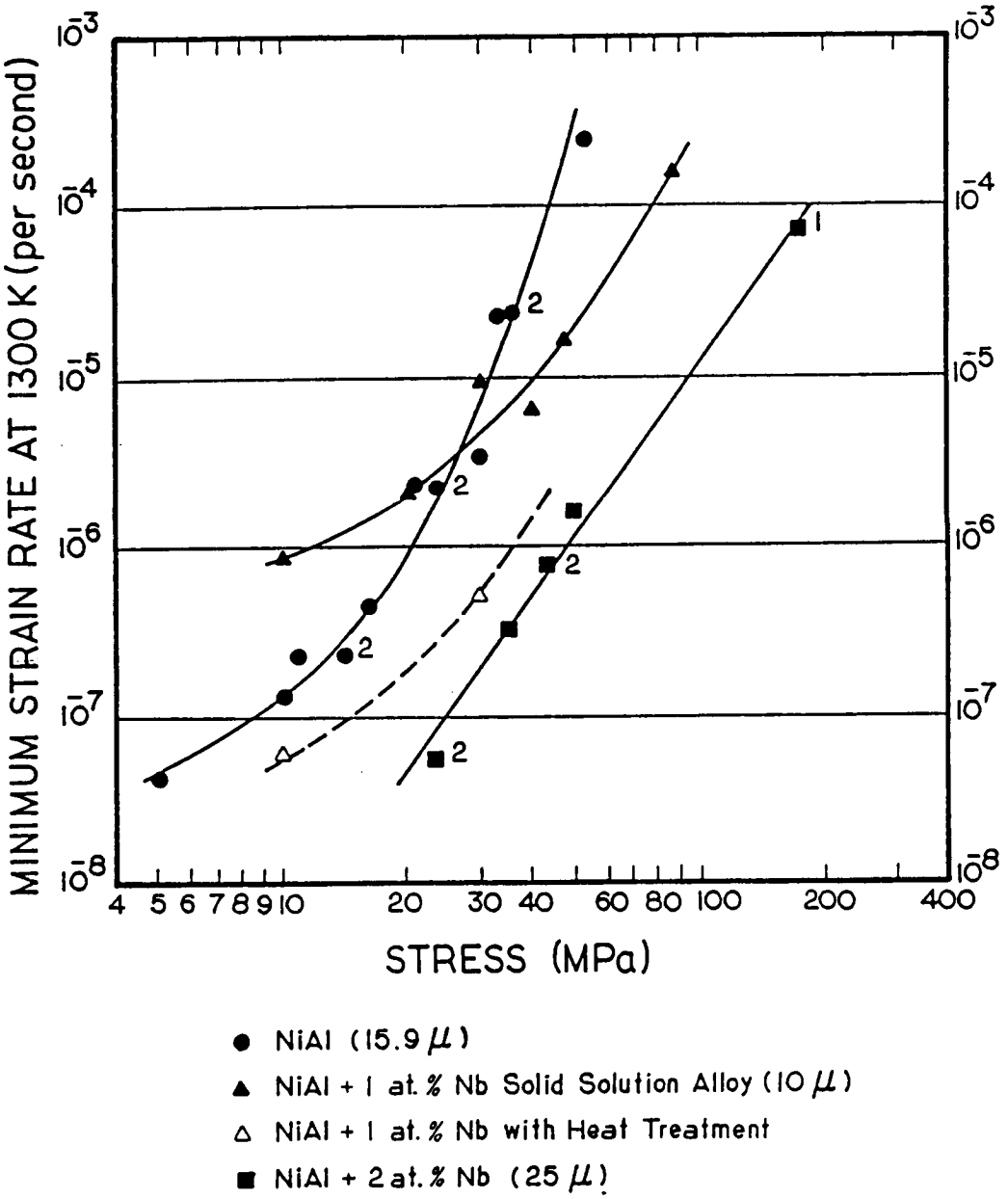
MINIMUM STRAIN RATE AT 1300 K (per second)
STRESS (MPa)
4 5 6 7 8 9 10 20 30 40 60 80 100 200 400
● NiAl (15.9 μ)
▲ NiAl + 1 at. % Nb Solid Solution Alloy (10 μ)
△ NiAl + 1 at. % Nb with Heat Treatment
■ NiAl + 2 at. % Nb (25 μ)

Figure 4.7 Creep of NiAl + Nb alloys at 1300 ^{o}K in compression.

ORIGINAL PAGE IS
OF POOR QUALITY

Figure 4.8 TEM brightfield micrograph of NiAl+1at.%Nb alloy heat treated at 1523 ^{o}K for 2 hrs. and 1300 ^{o}K for 10 hrs.

ORIGINAL PAGE IS
OF POOR QUALITY

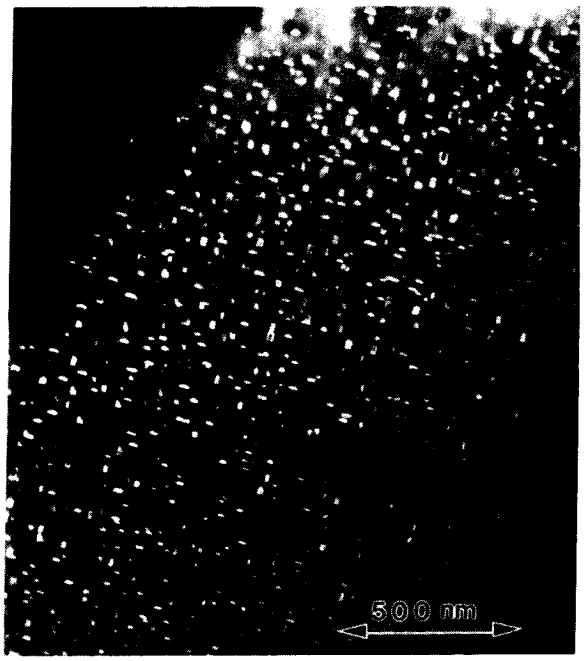

Figure 4.9 TEM dark field image of NiAl+2at.%Nb alloy after the heat treatment at 1623 ^{o}K for 100 hrs.

ORIGINAL PAGE IS
OF POOR QUALITY

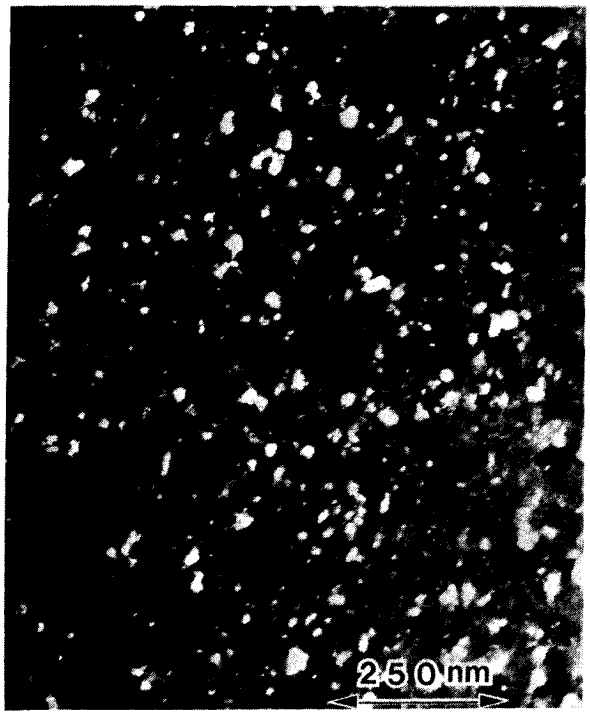

Figure 4.10 TEM dark field image of NiAl+2at.%Ta alloy after the heat treatment at 1623 ^{O}K for 100 hrs.

ORIGINAL PAGE IS
OF POOR QUALITY

Figure 4.11 TEM bright field microstructure of NiAl+2at.%Ta alloy after slow compression testing at 1300 ^{o}K with a nominal strain rate of 6 X 10^{-6} s^{-1}.

ORIGINAL PAGE IS
OF POOR QUALITY

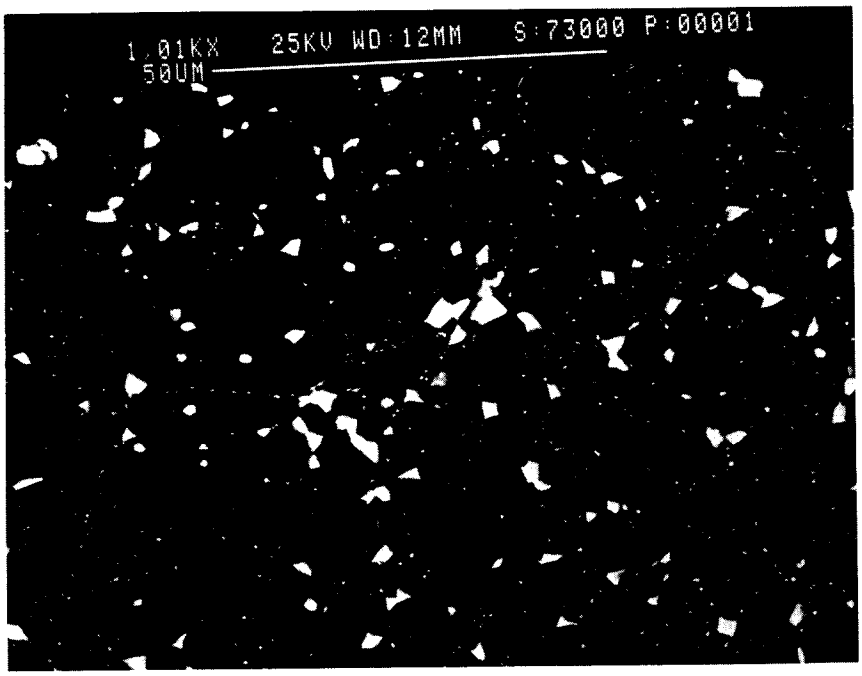

Figure 4.12 BSE image of a NiAl+4.5at.%Ta alloy vacuum hot pressed at 1723 ^{O}K for 6.5 hrs.

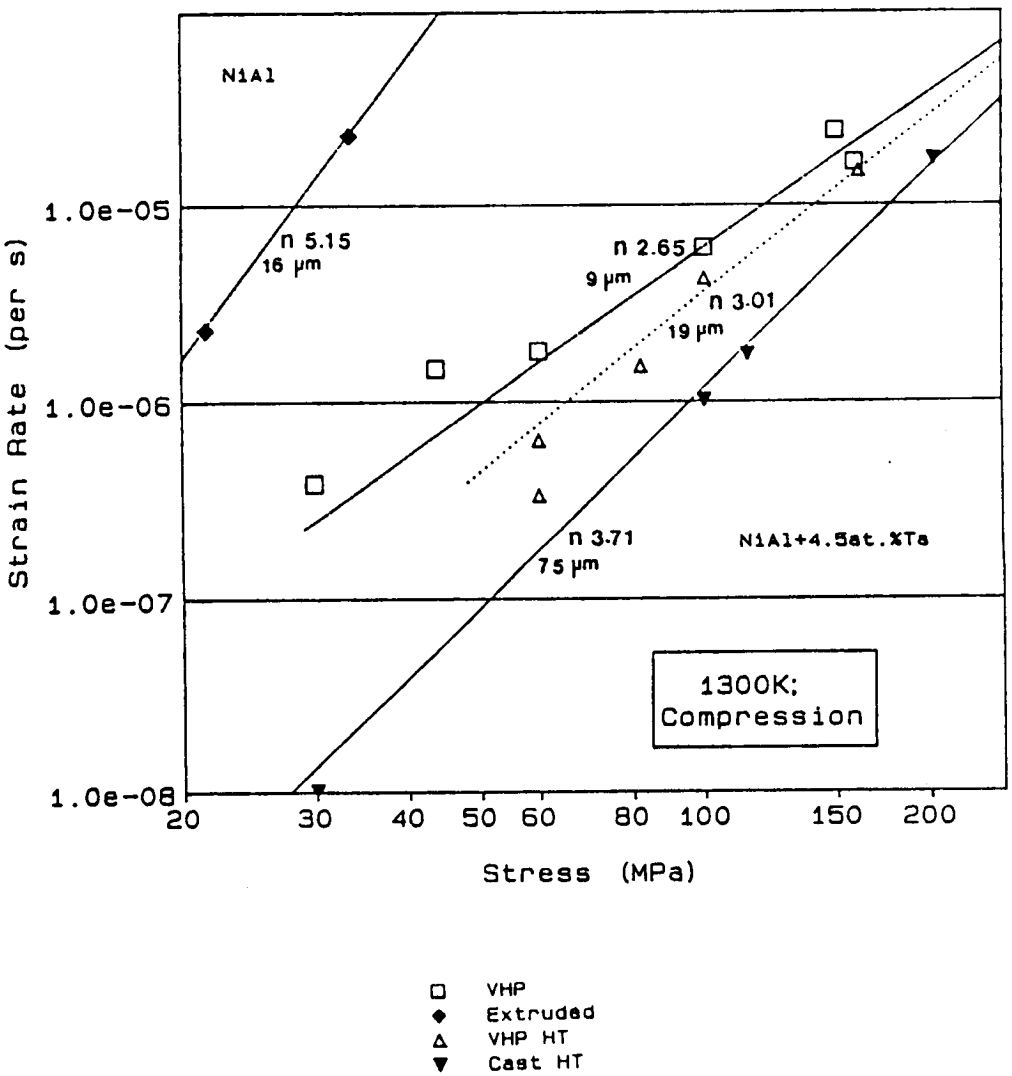

Figure 4.13 Creep of NiAl + Ta alloys tested in compression at 1300 ^{o}K.

ORIGINAL PAGE IS
OF POOR QUALITY

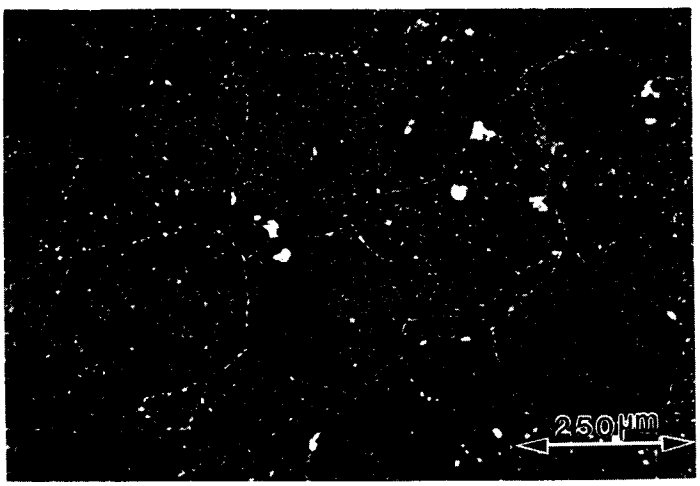

Figure 4.14 BSE image of a VHP NiAl+4.5at.%Ta alloy after heat treatment #4.

ORIGINAL PAGE IS
OF POOR QUALITY

Figure 4.15 TEM bright field micrograph of VHP NiAl+4.5at.%Ta alloy with heat treatment #4.

ORIGINAL PAGE IS
OF POOR QUALITY

Figure 4.16 Dislocations in VHP NiAl+4.5at.%Ta alloy after heat treatment #4. A TEM bright field micrograph.

Figure 4.17 TEM bright field microstructure of a heat treated NiAl+4.5at.%Ta alloy after testing at 1300 ^{o}K with 60 MPa stress.

ORIGINAL PAGE IS
OF POOR QUALITY

ORIGINAL PAGE IS
OF POOR QUALITY

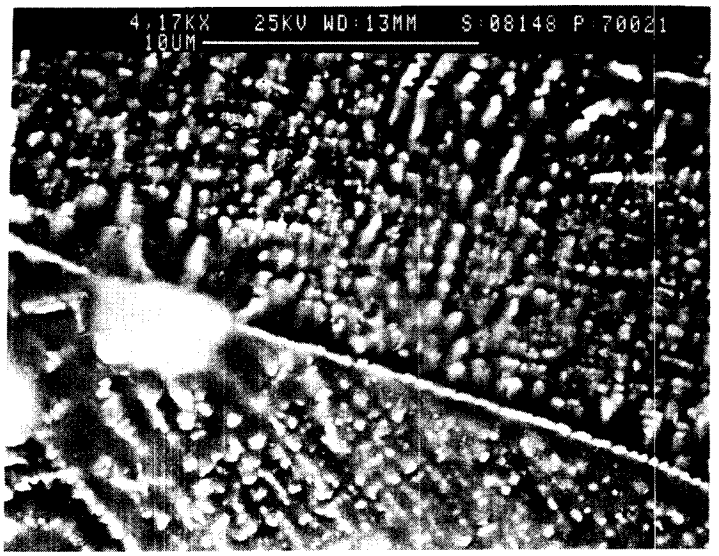

Figure 4.18 BSE image of a cast and heat treated NiAl+5at.%Ta alloy.

Table 4.1
Compressive Creep of NiAl (16 μm)
Diffusional Creep Regime

Temperature ^{o}K	Normal Stress MPa	Normal Strain Rate s^{-1}
1250	5	2.18×10^{-8}
1300	5	4.06×10^{-8}
1350	5	1.80×10^{-7}
1300	7	1.18×10^{-7}
1350	7	1.98×10^{-7}
1400	7	3.48×10^{-7}
1300	10	1.46×10^{-7}

Table 4.2
Creep of NiAl+1at.%Ta Alloy

Treatment (grain size)	Test	Temp. ^{o}K	True Stress (MPa)	True Strain Rate (s^{-1})
As extruded (9 μm)	CC	1300	10	1.75×10^{-7}
As extruded (9 μm)	CC	1300	20	7.68×10^{-7}
As extruded (9 μm)	SC	1300	29	1.68×10^{-6}
As extruded (9 μm)	CC	1300	30	1.36×10^{-6}
As extruded (9 μm)	CC	1300	40	3.18×10^{-6}
As extruded (9 μm)	CC	1300	50	6.42×10^{-6}
As extruded (9 μm)	SC	1300	54	1.68×10^{-5}
As extruded (9 μm)	CC	1300	90	4.05×10^{-5}
As extruded (9 μm)	CC	1300	100	1.68×10^{-4}
As extruded (9 μm)	CC	1400	30	1.41×10^{-5}
As extruded (9 μm)	CC	1400	50	1.10×10^{-4}
Annealed at 1523 ^{o}K for 2 hrs., 1300 ^{o}K for 10 hrs.	CC	1300	10	8.57×10^{-8}
Annealed at 1523 ^{o}K for 2 hrs., 1300 ^{o}K for 10 hrs.	CC	1300	30	8.28×10^{-7}

Table 4.2(continued)
Creep of NiAl+1at.%Ta Alloy

Treatment	Test	Temp. ^{o}K	True Stress (MPa)	True Strain Rate (s^{-1})
Annealed at 1623 ^{o}K for 2 hrs., 1300 ^{o}K for 10 hrs.	CC	1300	30	4.89×10^{-7}
Annealed at 1723 ^{o}K for 24 hrs. followed by furnace cooling.	CC	1300	30	1.87×10^{-6}
Annealed at 1400 ^{o}K for 24 hrs. followed by slow cooling.	CC	1300	30	1.73×10^{-6}

Table 4.3
Creep of NiAl+1at.%Nb Alloy

Treatment (grain size)	Test	Temp. ^{o}K	True Stress (MPa)	True Strain Rate (s^{-1})
As extruded (10 μm)	CC	1300	10	8.72×10^{-7}
As extruded (10 μm)	CC	1300	20	2.00×10^{-6}
As extruded (10 μm)	CC	1300	30	9.57×10^{-6}
As extruded (10 μm)	CC	1300	40	6.60×10^{-6}
As extruded (10 μm)	SC	1300	47	1.70×10^{-5}
As extruded (10 μm)	SC	1300	87	1.70×10^{-4}
Annealed at 1523 ^{o}K for 2 hrs., 1300 ^{o}K for 10 hrs.	CC	1300	10	5.93×10^{-8}
Annealed at 1523 ^{o}K for 2 hrs., 1300 ^{o}K for 10 hrs.	CC	1300	30	5.24×10^{-7}
Annealed at 1523 ^{o}K for 2 hrs., 1300 ^{o}K for 10 hrs.	CC	1300	60	2.07×10^{-5}

Table 4.4
Data Fitted to the Equation

$$\dot{\epsilon} = B\,\sigma^{n} \exp(-Q/RT)$$

Alloy	Treatment	Q(kJ/mole)	n	r^2
NiAl	As extruded	308	5.32	.99[1]
NiAl+1at.%Ta	As extruded	403±44	4.6±.4	.98
NiAl+1at.%Nb	As extruded	--	4.3±.4	.96
NiAl+2at.%Ta	Annealed at 1623 ^{o}K for 100 hrs.	438±88	2.6±.4	.89
NiAl+2at.%Nb	Annealed at 1623 ^{o}K for 100 hrs.	495±66	3.5±.5	.97
NiAl+4.5at.%Ta	As hot pressed	--	2.6±.4	.98
NiAl+4.5at.%Ta	VHP + HT4	--	3.5±.4	.92
NiAl+5at.%Ta	Cast + HT4	--	3.7±.4	.98

1 Whittenberger (1987a)

Table 4.5
Creep of NiAl+2at.%Ta Alloy (19 μm)

Treatment	Test	Temp. ^{o}K	True Stress (MPa)	True Strain Rate (s^{-1})
Annealed at 1623 ^{o}K, 100 hrs.	SC	1200	346	1.64×10^{-6}
Annealed at 1623 ^{o}K, 100 hrs.	CC	1300	30	6.22×10^{-8}
Annealed at 1623 ^{o}K, 100 hrs.	SC	1300	49	3.29×10^{-7}
Annealed at 1623 ^{o}K, 100 hrs.	CC	1300	60	1.90×10^{-6}
Annealed at 1623 ^{o}K, 100 hrs.	SC	1300	111	1.65×10^{-6}
Annealed at 1623 ^{o}K, 100 hrs.	SC	1400	21	3.37×10^{-7}
Annealed at 1623 ^{o}K, 100 hrs.	SC	1400	61	2.04×10^{-5}

Table 4.6
Creep of NiAl+2at.%Nb Alloy (25 μm)

Treatment	Test	Temp. ^{o}K	True Stress (MPa)	True Strain Rate (s^{-1})
Annealed at 1623 ^{o}K, 100 hrs.	SC	1200	176	1.65×10^{-6}
Annealed at 1623 ^{o}K, 100 hrs.	SC	1300	35	3.29×10^{-7}
Annealed at 1623 ^{o}K, 100 hrs.	SC	1300	50	1.66×10^{-6}
Annealed at 1623 ^{o}K, 100 hrs.	SC	1400	24	1.68×10^{-6}
Annealed at 1623 ^{o}K, 100 hrs.	SC	1400	43	2.02×10^{-5}

Table 4.7
Creep of VHP NiAl+4.5at.%Ta Alloy

Treatment	Test	Temp. ^{o}K	True Stress (MPa)	True Strain Rate (s^{-1})
As hot pressed (8 μm)	CC	1300	30	3.92×10^{-7}
As hot pressed (8 μm)	SC	1300	44	1.47×10^{-6}
As hot pressed (8 μm)	CC	1300	60	1.79×10^{-6}
As hot pressed (8 μm)	CC	1300	100	6.06×10^{-6}
As hot pressed (8 μm)	CC	1300	150	2.44×10^{-5}
As hot pressed (8 μm)	SC	1300	159	1.66×10^{-5}
As hot pressed (8 μm)	SC	1300	348	1.66×10^{-4}
Annealed at 1300 ^{o}K for 8 hrs. (HT1) (8 μm)	CC	1300	60	1.18×10^{-6}
Annealed at 1300 ^{o}K for 8 hrs. (HT1) (8 μm)	CC	1300	100	7.67×10^{-6}
Annealed at 1523 ^{o}K for 8 hrs., 1573 ^{o}K for 24 hrs. and 1300 ^{o}K for 8 hrs. in argon.(HT2) (9 μm)	CC	1300	60	4.81×10^{-6}
Annealed at 1523 ^{o}K for 8 hrs., 1573 ^{o}K for 24 hrs. and 1300 ^{o}K for 8 hrs. in argon.(HT2) (9 μm)	CC	1300	100	1.81×10^{-5}

Table 4.7(continued)
Creep of VHP NiAl+4.5at.%Ta Alloy

Treatment	Test	Temp. ^{o}K	True Stress (MPa)	True Strain Rate (s^{-1})
Annealed at 1573 ^{o}K for 8 hrs., 1623 ^{o}K for 24 hrs. and 1300 ^{o}K for 8 hrs. in argon.(HT3) (11 μm)	CC	1300	60	9.86×10^{-7}
Annealed at 1573 ^{o}K for 8 hrs., 1623 ^{o}K for 24 hrs. and 1300 ^{o}K for 8 hrs. in argon.(HT3) (11 μm)	CC	1300	100	5.95×10^{-6}
Annealed at 1623 ^{o}K for 8 hrs., 1673 ^{o}K for 24 hrs. and 1300 ^{o}K for 8 hrs. in argon.(HT4) (19 μm)	CC	1300	60	3.41×10^{-7}
Annealed at 1623 ^{o}K for 8 hrs., 1673 ^{o}K for 24 hrs. and 1300 ^{o}K for 8 hrs. in argon.(HT4) (19 μm)	CC	1300	100	4.21×10^{-6}
Annealed at 1623 ^{o}K for 8 hrs., 1673 ^{o}K for 72 hrs. and 1300 ^{o}K for 8 hrs. in argon.(HT4L)	CC	1300	60	6.38×10^{-7}
Annealed at 1623 ^{o}K for 8 hrs., 1673 ^{o}K for 72 hrs. and 1300 ^{o}K for 8 hrs. in argon.(HT4L)	SC	1300	82	1.50×10^{-6}
Annealed at 1623 ^{o}K for 8 hrs., 1673 ^{o}K for 72 hrs. and 1300 ^{o}K for 8 hrs. in argon.(HT4L)	CC	1300	161	1.50×10^{-5}

Table 4.8
Heat Treatments for NiAl+4.5at.%Ta Alloy

Heat Treatment	8 hours	24 hours	8 hours
HT1	1473 ^{o}K	1523 ^{o}K	1300 ^{o}K
HT2	1523 ^{o}K	1573 ^{o}K	1300 ^{o}K
HT3	1573 ^{o}K	1623 ^{o}K	1300 ^{o}K
HT4	1623 ^{o}K	1673 ^{o}K	1300 ^{o}K
HT5	--	--	1300 ^{o}K

Table 4.9
Creep of Cast NiAl+5at.%Ta Alloy (75 μm)

Treatment	Test	Temp. ^{o}K	True Stress (MPa)	True Strain Rate (s^{-1})
Annealed at 1623 ^{o}K for 8 hrs., 1673 ^{o}K for 24 hrs. and 1300 ^{o}K for 8 hrs. in argon.(HT4)	CC	1300	30	1.02×10^{-8}
Annealed at 1623 ^{o}K for 8 hrs., 1673 ^{o}K for 24 hrs. and 1300 ^{o}K for 8 hrs. in argon.(HT4)	CC	1300	100	1.02×10^{-6}
Annealed at 1623 ^{o}K for 8 hrs., 1673 ^{o}K for 24 hrs. and 1300 ^{o}K for 8 hrs. in argon.(HT4)	SC	1300	114	1.73×10^{-6}
Annealed at 1623 ^{o}K for 8 hrs., 1673 ^{o}K for 24 hrs. and 1300 ^{o}K for 8 hrs. in argon.(HT4)	SC	1300	203	1.74×10^{-5}

5. Conclusions

5.1 Processing

(i) It is possible to hot extrude prealloyed NiAl+1at.%Ta and NiAl+1at.%Nb powders with 16:1 area reduction ratio at 1400°K. Extruded microstructure has equiaxed recrystallized grains which are almost free of any second phase precipitates.

(ii) Blended NiAl+2at.%Ta and NiAl+2at.%Nb powders can be hot extruded at 1400°K with 16:1 reduction ratio. Extrusion is achieved by flow of NiAl around tantalum or niobium rich areas.

(iii) Prealloyed NiAl+4.5at.%Ta powder could not be hot extruded by using upto 1379 MPa (200 ksi) pressure at temperatures upto 1450°K.

(iv) Prealloyed NiAl+4.5at.%Ta powder can be vacuum hot pressed by applying 21 MPa pressure for 6.5 hours at 1723°K.

5.2 Physical Metallurgy

(i) Extruded NiAl+1at.%Ta and NiAl+1at.%Nb alloys show no phase transformation upto melting. Abnormal grain growth is observed between 1373°K to 1473°K and is affected by particle size distribution in the original powders.

(ii) Extruded and homogenized NiAl+2at.%Ta and NiAl+2at.%Nb alloys have a distribution of fine precipitates of NiAlTa and NiAlNb respectively which are stable at 1300°K. Hexagonal NiAlTa precipitates bear an orientation relationship with the matrix in which the prism planes of the precipitates are parallel to the closest packed planes of the NiAl matrix.

(iii) Prealloyed NiAl+4.5at.%Ta powder is multiphase and contains Ni_2AlTa and NiAlTa as second phases. NiAlTa disappears upon any heat treatment below 1700°K and a previously unreported ordered fcc phase with approximate composition $Ta_5Ni_3Al_2$ appears. Ni_2AlTa is always present but transforms at about 1700°K.

(iv) Cast and heat treated alloy shows a uniform distribution of fine Ni_2AlTa and NiAlTa precipitates in the matrix.

5.3 Creep

(i) Compressive creep behavior of small grained NiAl at 1300°K with very low applied stress indicates dominance of diffusional creep mechanism.

(ii) NiAl+1at.%Ta and NiAl+1at.%Nb alloys show improvement over binary NiAl in the high stress regime due to solid solution strengthening. However, in the low stress region diffusional creep dominates and NiAl, which had a larger grain size (16 μm) than these alloys (9-10 μm) has higher strength.

(iii) NiAl+2at.%Ta, NiAl+2at.%Nb and NiAl+4.5at.%Ta alloys which have significant amounts of second phase precipitates show substantial improvement over binary NiAl due to lowering of both diffusion creep and dislocation creep. Dislocation arrays stabilized by precipitates can be seen in tested

alloys.

(iv) The cast NiAl+5at.%Ta alloy, which has both larger grain size (good for diffusion creep) and a distribution of fine second phase precipitates (good for both diffusion and dislocation creep) shows the best improvement over pure NiAl.

6. References

Ashby, M.F., 1973, The Microstructure and Design of Alloys: Proceedings of the 3rd International Conference on the Strength of Metals and Alloys (Cambridge) vol.2, (The Inst. of Metals), p. 8.

Baker, I., and E.M. Schulson, 1984, *Met Trans. A* **15A**, 1129.

Ball, A., and R.E. Smallman, 1966, *Acta Metall.* **14**, 1349.

Benjamin, J.S., B.C. Giessen, and N.J. Grant , 1966, *Trans. AIME* **236**, 224.

Burke, J.E., and D. Turnbull, 1952, *Prog. Met. Phys.* **3**, 220.

Cahn, R.W., 1983, Physical Metallurgy II, (North-Holland Physics Pub., N.Y.), p. 1658.

Coble, R.L., 1963, *J. Appl. Phys.* **34**, 1679.

Cullity, B.D., 1978, Elements of X-ray Diffraction, (Addison-Wesley Pub. Co., Reading, MA), p. 327.

Frost H.J., and Ashby, M.F., 1982, Deformation Mechanism Maps (Pergamon Press, Oxford).

Gibbs, G.B., 1965, *Mem. Sci. Rev. Met.* **62**, 781.

Giessen, B.C., and Grant, N.J., 1965, *Acta. Cryst.* **18**, 1080.

Giessen, B.C., and R. Ray, 1971, *J. Less-Common Met.* **23**, 95.

Harris, J.E., R.B. Jones, G.W. Greenwood, and M.J. Ward, 1969, *J. Australian Inst. Metals.* **14**, 154.

Heine, W., and Zwicker, U., 1962, *Naturewiss* **49**, 391.

Herring, C., 1950, *J. Appl. Phys.* **21**, 437.

Jung, I., M. Rudy, and G. Sauthoff, 1986, in:High Temperature Ordered Intermetallics II 81, Eds. N.S. Stoloff, C.C. Koch, C.T. Liu, O. Izumi (MRS, Pittsburgh), 263.

Kornilov, I.I., R.S. Mints, L.N. Guseva, Yu.S. Malkov, 1965, *Russian Metallurgy* **6**, 93.

Kusma, J.B., and H. Nowotny, 1964, *Montash Chem.* **95**, 428.

Leslie, W.C., J.T. Michalak, and F.W. Aul, 1963,in: Iron and Its Dilute Solid Solutions (Interscience, New York)

Lifshift, L.M., 1963, *Soviet Phys. JETP* **17**, 909.

Lloyd, C.H., and M.H. Loretto, 1971, *Phys. Stat. Sol.* **23**, 1311.

Markiv, V.Ja., Ju.V. Vorosilov, P.I. Kripjakevic and E.E. Cerkasin, 1964, *Kristallografija SSR* **9**, 737.

Markiv, V.Ya., N.F. Matushevskaya, and Yu.B. Kuzma, 1966, *Russ. Met.* **6**, 72.

Mukherjee, A.K., 1975, in: Treaties on Materials Science and Technology **6**, eds. R.J. Arsenault, (Academic Press, N.Y.), p. 164-224.

Nabarro, F.R.N., 1948, Report on a Conference on the Strength of Metals (Phys. Soc. London)

Nash, P., and D.R.F. West, 1979, *Metal Science* **13**, 670.

Nash, P., F.P.L. Kavishe, and D.R.F. West, 1980, *Metal Sc.* **14**, 147.

Nix, W.D., 1986, Final Technical Report NASA Grant NAG 3-248.

Pascoe, R.T., and C.W.A. Newey, 1968, *Phys. Stat. Sol.* **29**, 357.

Pathare, V.M., K.M. Vedula, and R.H. Titran, 1985, in: Modern Developments in Powder Metallurgy **16**, eds. E.N. Aqua and C.I. Whitman (MPIF, Princeton), pp. 695 - 704.

Polvani, R.S., W.S. Tzeng and P.R. Strutt, 1976, *Met. Trans. A* **7A**, 33.

Raj, R., and M.F. Ashby, 1971, *Met. Trans.* **2**, 1113.

Raman, A., and K. Schbert, 1965, *Z. Metallkd.* **56**, 99.

Sherby, O.D., and P.M. Burke, 1967, *Prog. Mat. Sci.* **13**, 325.

Sherman, M., and K.M. Vedula, 1986, *J. of Matls. Sc.* **21**, 1974.

Singolton, M.F.,J.L. Murray, and P. Nash, 1986, in: Binary Alloy Phase Diagrams **I**, eds. T.B. Mussalski,

(ASM, Metals Park), p. 142.

Smith, C.S., 1948, *Trans. AIME* **175**, 151.

Stephenes, J.R., 1985,in: High Temperature Ordered Intermetallic Alloys **39**, eds. C.C. Koch, C.T. Liu and N.S. Stoloff (MRS, Pittsburgh), p 381.

Taceuchi, S., and A.S. Argon, 1976, *J. Mat. Sci.* **11**, 1542.

Vandervoort, R.R., A.K. Mukherjee, and J.E. Dorn, 1966, *Trans. ASM* **59**, 930.

Vedula, K.M., V.M. Pathare, I. Aslanidis and R.H. Titran, 1985, in: High Temperature Ordered Intermetallic Alloys **39**, eds. C.C. Koch, C.T. Liu and N.S. Stoloff (MRS, Pittsburgh), p 411.

Wasilewski, R.J., S.R.Butler, and J.E. Hanlon, 1967, *Trans. AIME* **239**, 1357.

Weertman, J., 1956, *J. Mech. Phys. Solids* **4**,230.

Weertman, J., 1960, *Trans. AIME* **218**, 207.

Weertman, J., 1963, *Trans. AIME* **227**, 1475.

Whittenberger, J.D., 1987a, *J. of Mat. Sc.* **22**, 394 - 402.

Whittenberger, J.D., 1987b, accepted for publication in J. Matls. Sc.

Whittenberger, J.D., 1987c, accepted for publication in the Proceedings of the Conference of NE Region of AIME and MRS at the Stevens Inst. of Tech., NJ.

Williams, D.B., 1984, Practical Analytical Electron Microscopy in Materials Science, (Philips Electronics Instruments, Mahwah, NJ), p. 128.

Yang, W.J., and R.A. Dodd, 1973, *Metal Sc. Jr.* **7**, 41.

7. Appendix I

Differential Thermal Analysis Traces

Netzsch Simultaneous Thermal Analyzer STA 429

NASA Lewis Research Center, Cleveland, Ohio

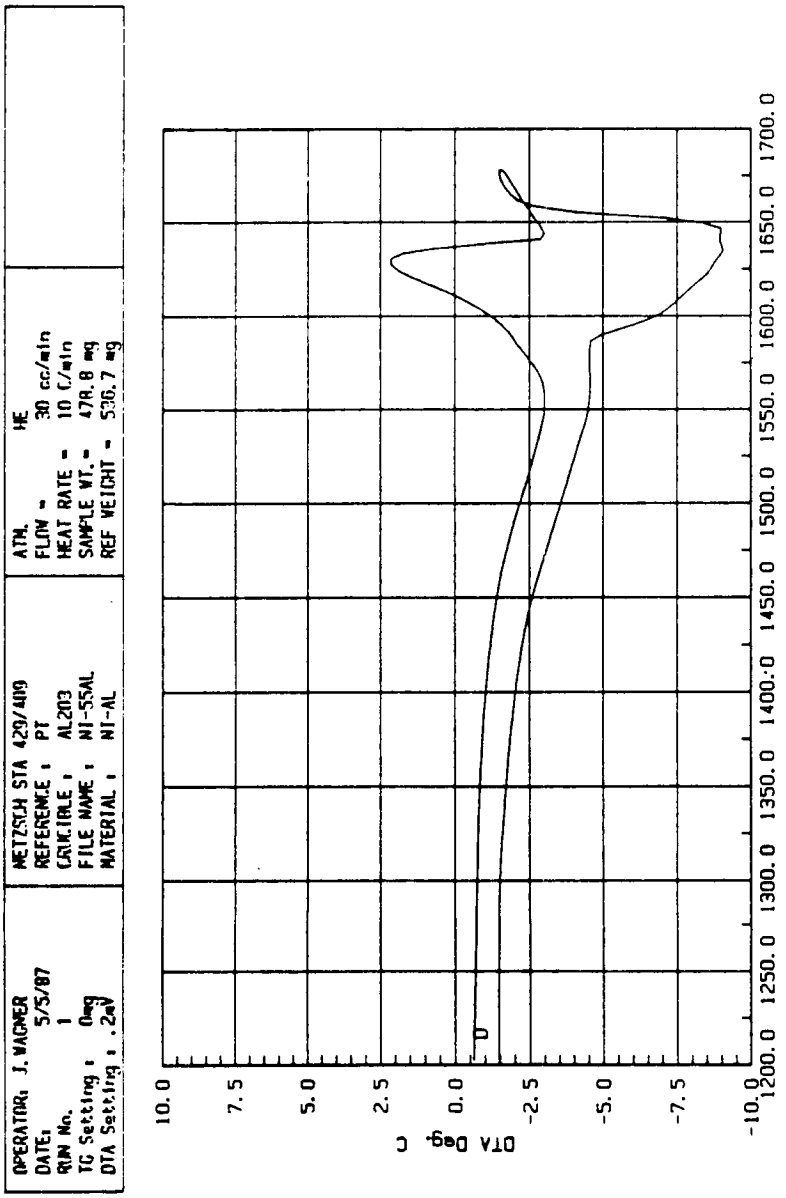

Figure 7.1 DTA trace of as received NiAl powder

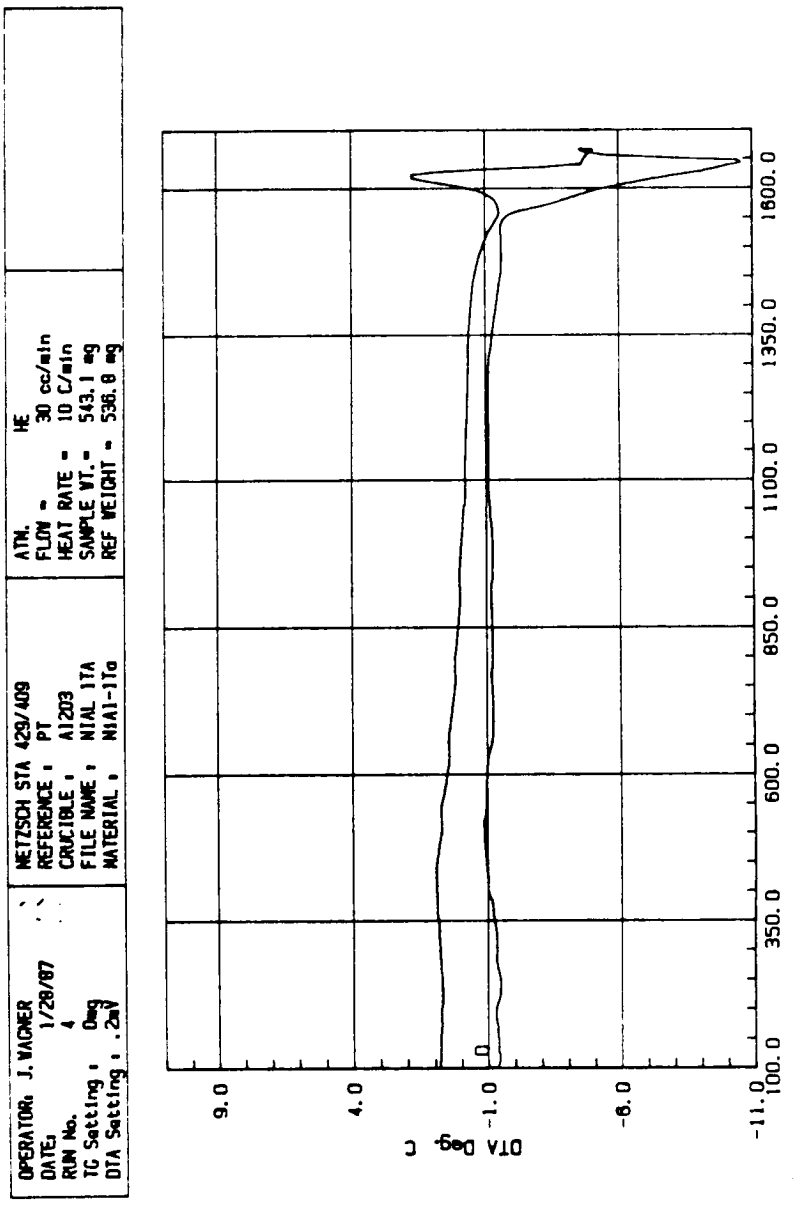

Figure 7.2 DTA trace of as received NiAl+1at.%Ta powder

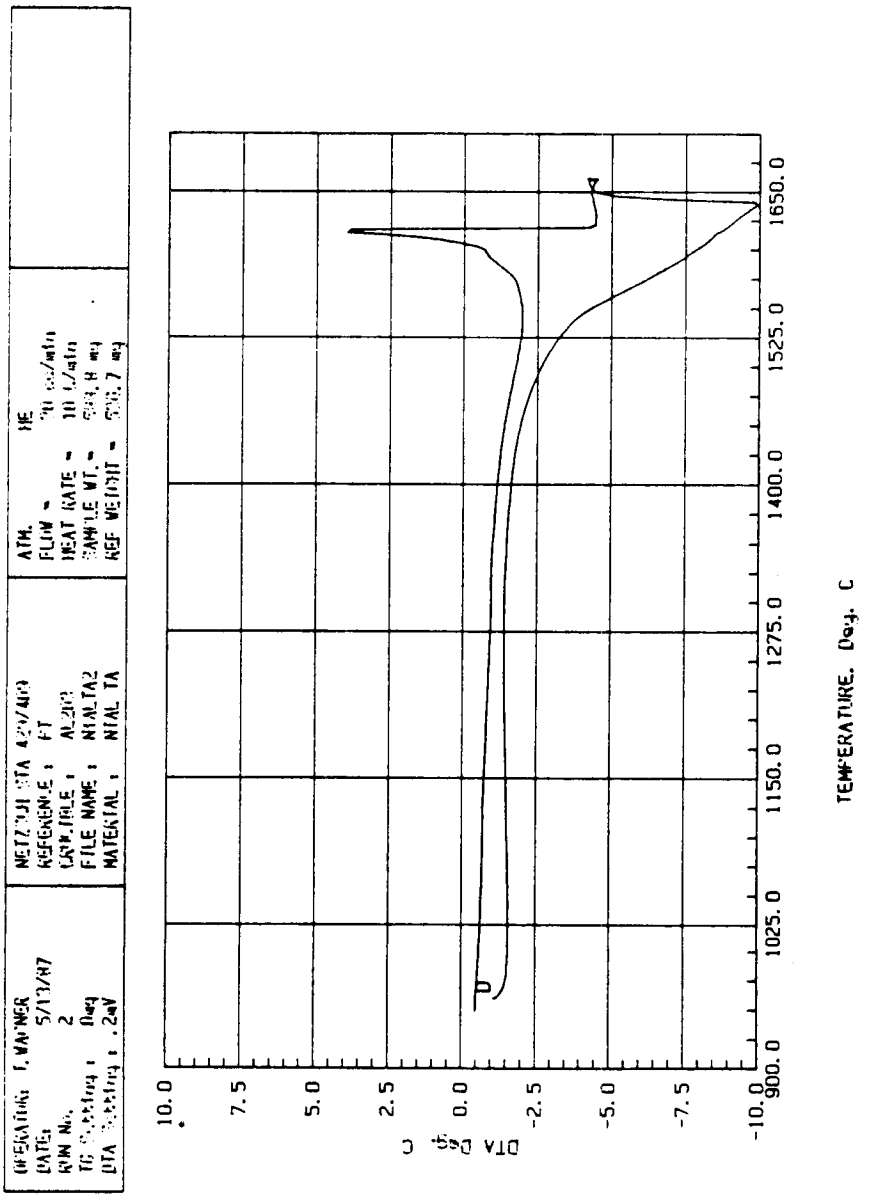

Figure 7.3 DTA trace of NiAl+1at.%Ta powder annealed at 1223 ^{o}K for 2 hours.

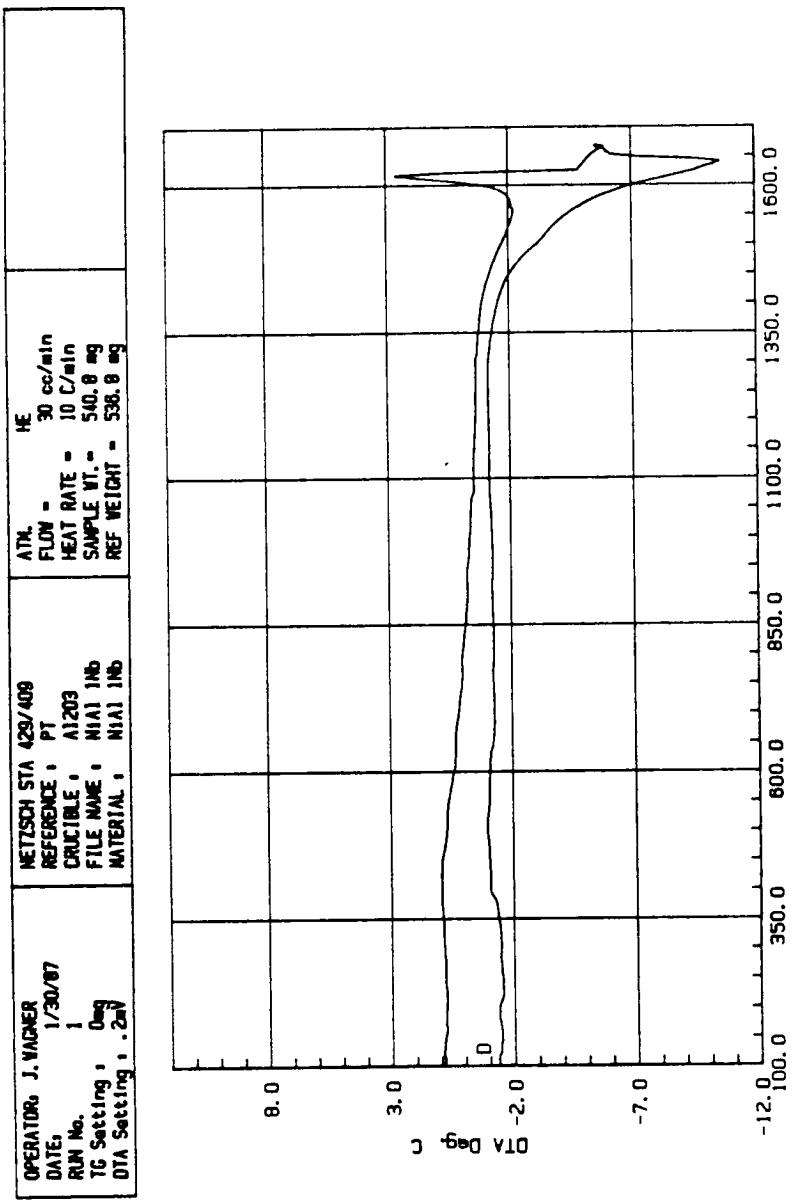

Figure 7.4 DTA trace of as received NiAl+1at.%Nb powder.

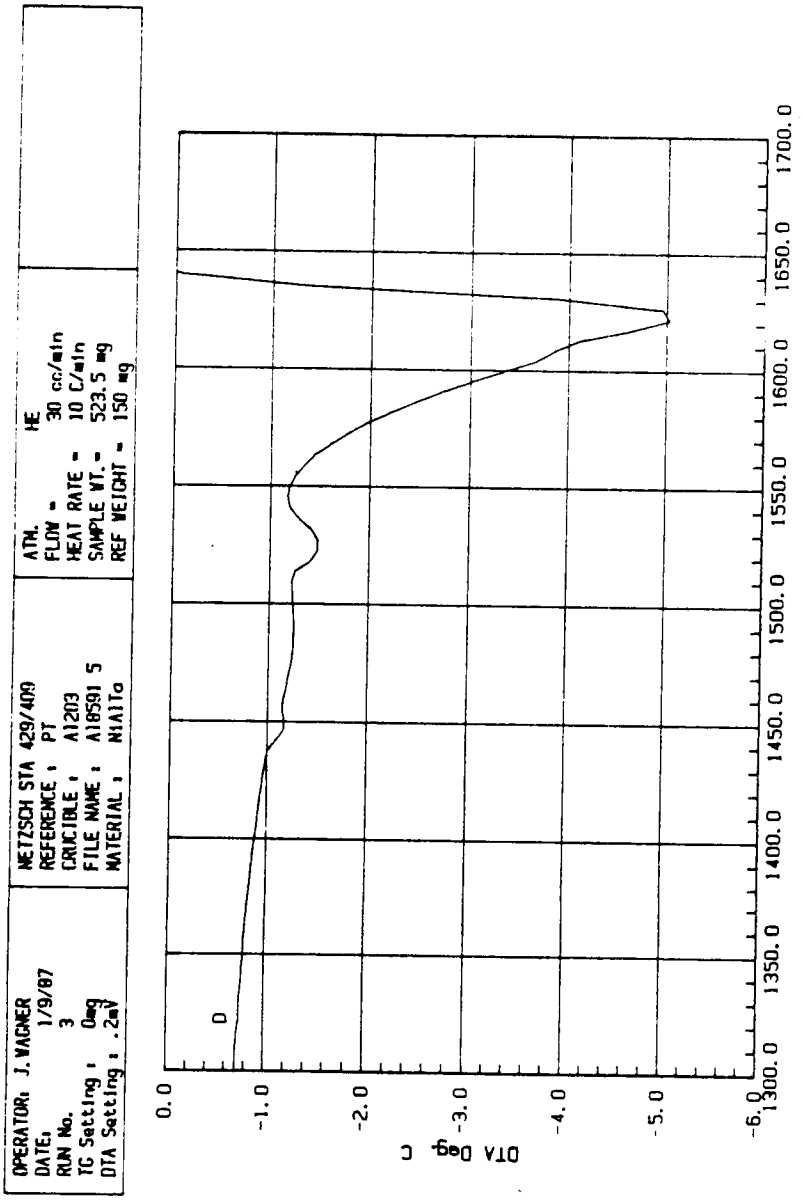

Figure 7.5 DTA trace of as received NiAl+4.5at.%Ta powder (heating).

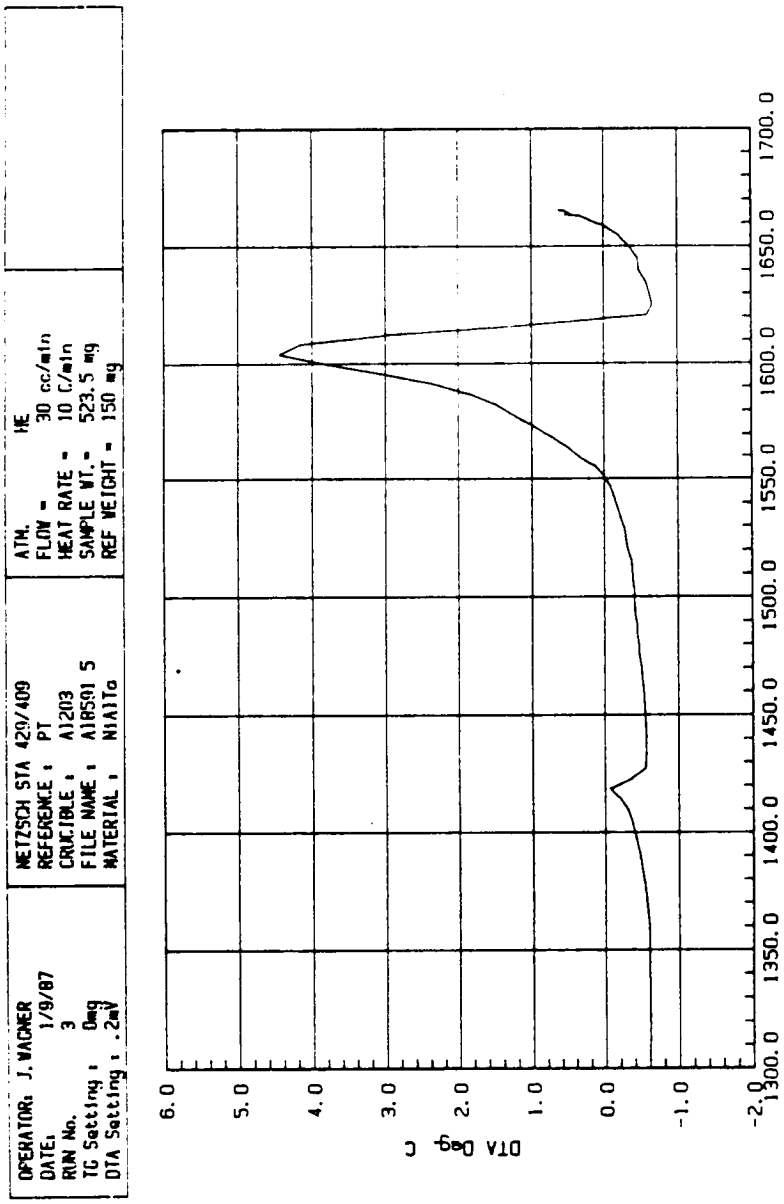

Figure 7.6 DTA trace of as received NiAl+4.5at.%Ta powder (cooling).

ORIGINAL PAGE IS
OF POOR QUALITY

ORIGINAL PAGE IS
OF POOR QUALITY

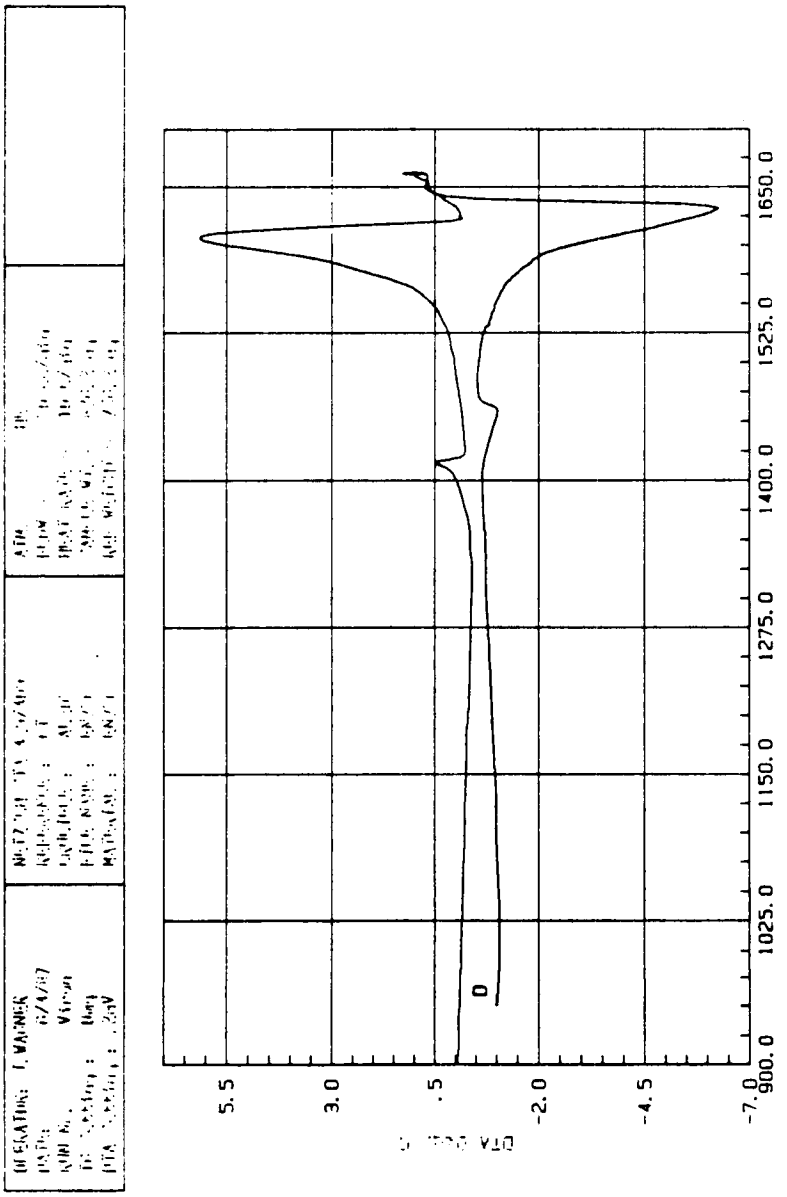

Figure 7.7 DTA trace of NiAl+4.5at.%Ta powder annealed at 1223 °K for 2 hours.

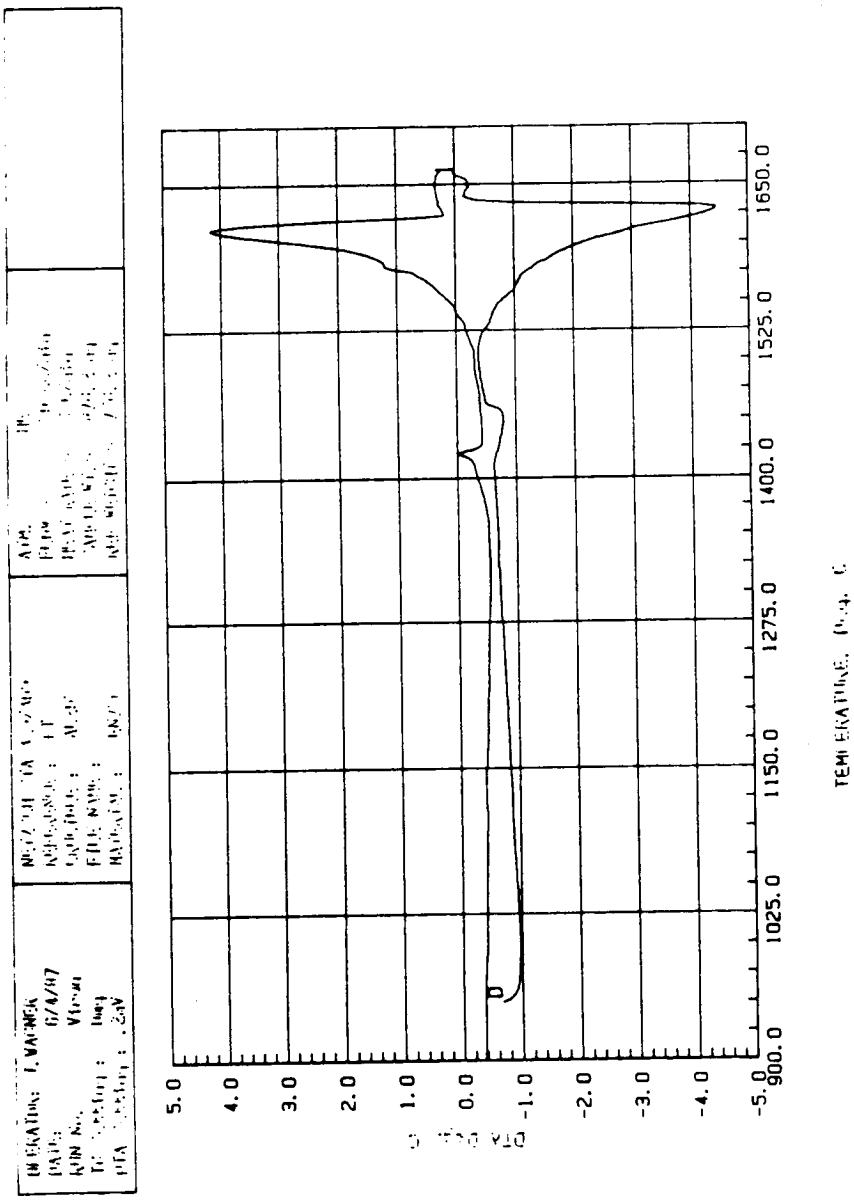

ORIGINAL PAGE IS
OF POOR QUALITY

Figure 7.8 DTA trace of NiAl+4.5at.%Ta powder annealed at 1223 ^{o}K for 2 hours. Rate of heating/cooling = 5 ^{o}K/min.

8. Appendix II

X-ray Diffractometer Scans

Philips Auto-Diffractometer

Step scan from 25 to 85 2

Step 0.05

Time interval 10 s at each step

Cu K 0.15418 nm

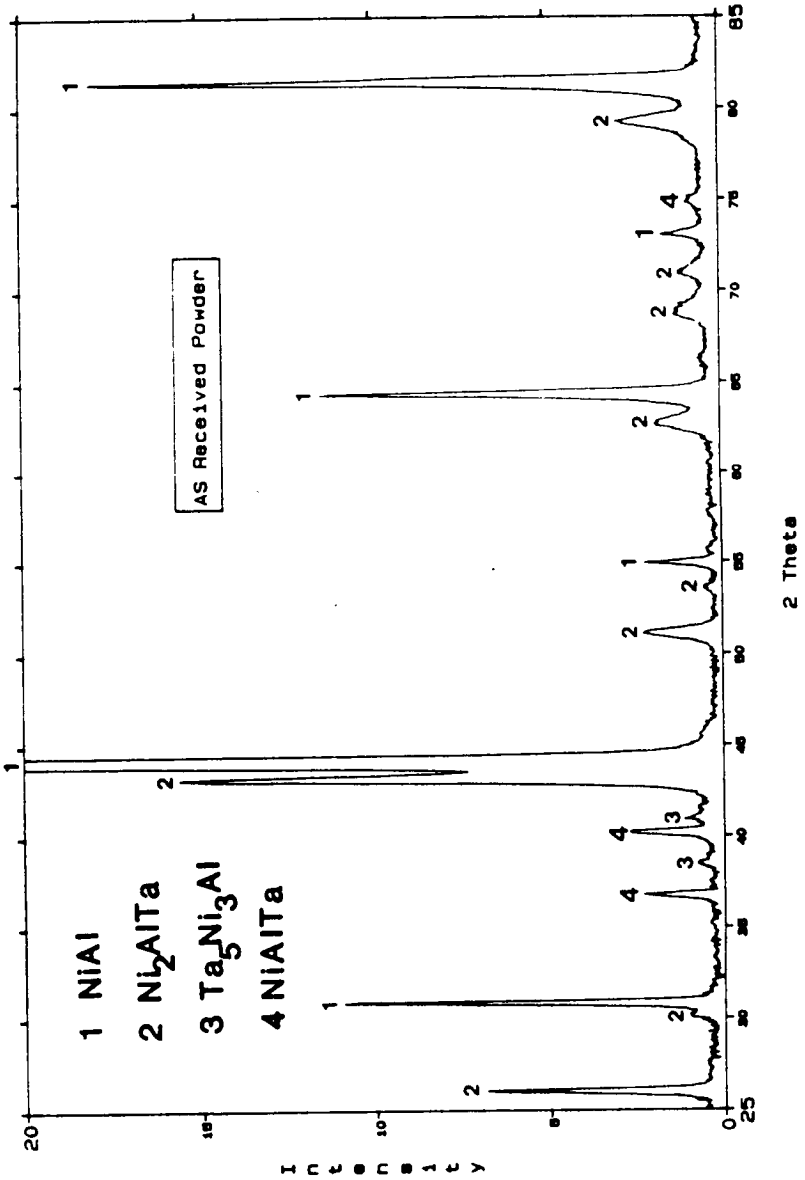

Figure 8.1 NiAl+4.5at.%Ta: As received prealloyed powder. 1 = NiAl, 2 = Ni_2AlTa, 3 = $Ta_5Ni_3Al_2$, 4 = NiAlTa.

ORIGINAL PAGE IS
OE POOR QUALITY

ORIGINAL PAGE IS
OF POOR QUALITY

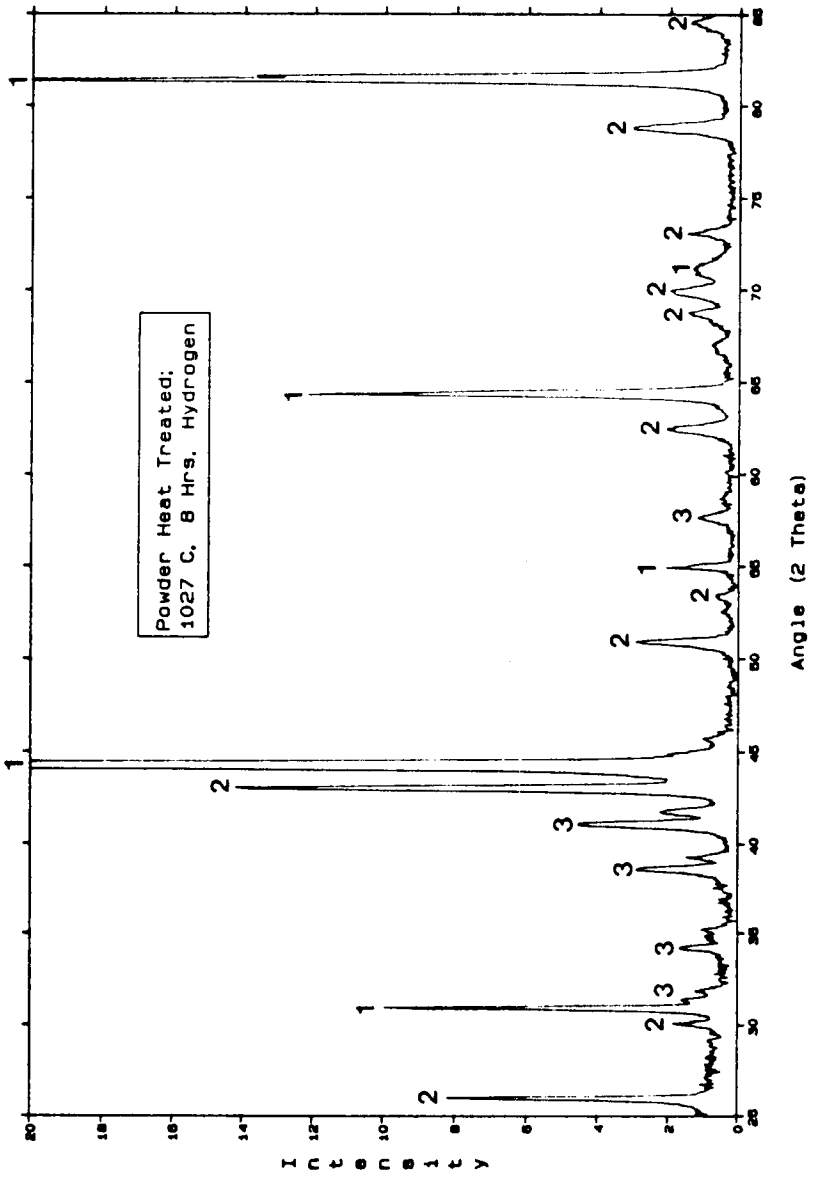

Figure 8.2 NiAl+4.5at.%Ta: Powder annealed at 1300°K for 8 hrs. in hydrogen. 1 = NiAl, 2 = Ni_2AlTa, 3 = $Ta_5Ni_3Al_2$, 4 = NiAlTa.

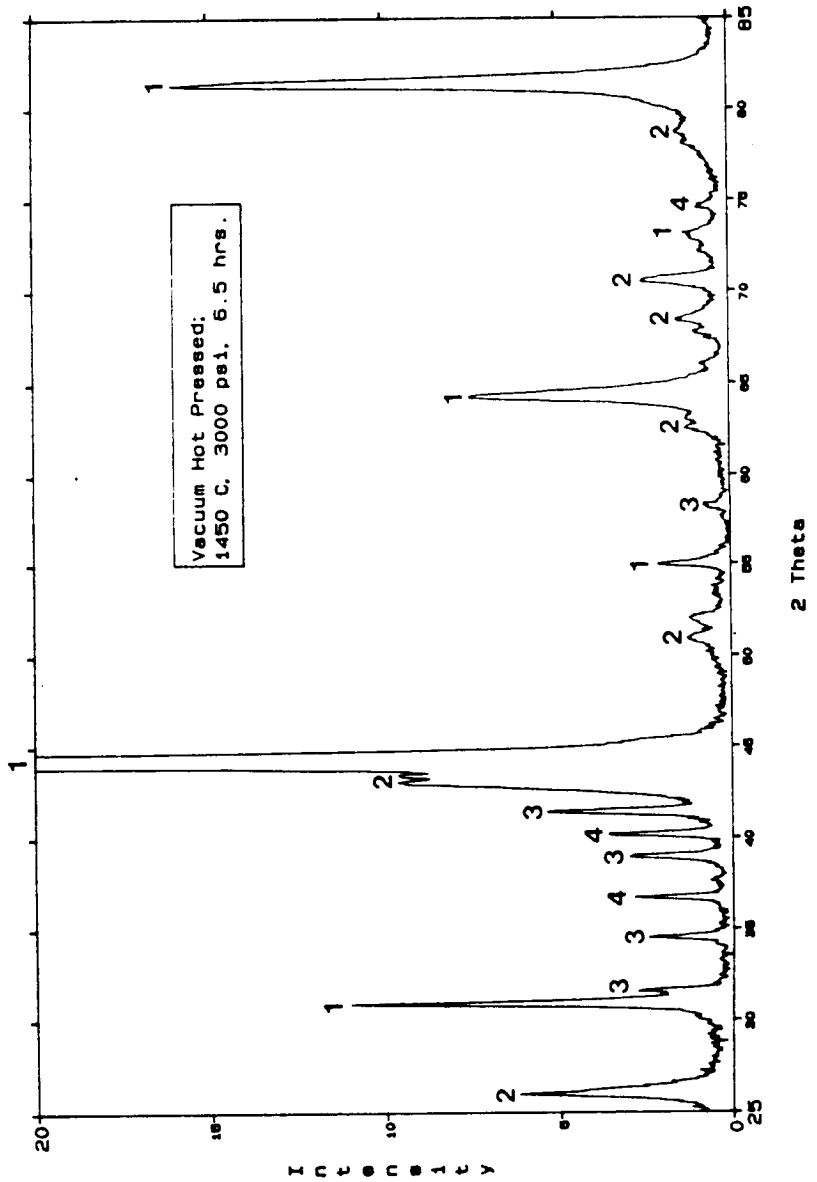

Figure 8.3 NiAl+4.5at.%Ta: Vacuum hot pressed (VHP) at 1723°K, 21 MPa, 6.5 hrs. 1 = NiAl, 2 = Ni_2AlTa, 3 = $Ta_5Ni_3Al_2$, 4 = NiAlTa.

ORIGINAL PAGE IS
OF POOR QUALITY

ORIGINAL PAGE IS
OF POOR QUALITY

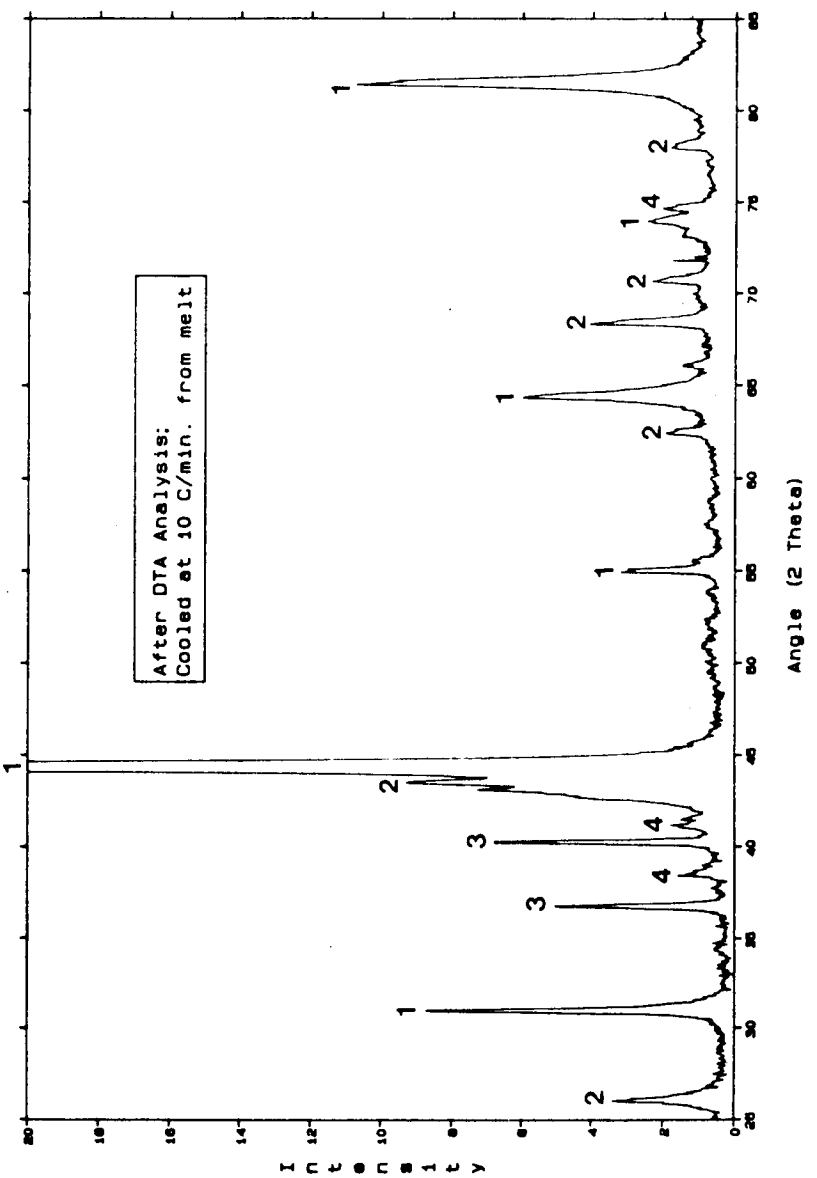

Figure 8.4 NiAl+4.5at.%Ta: VHP and then remelted. 1 = NiAl, 2 = Ni_2AlTa, 3 = $Ta_5Ni_3Al_2$, 4 = NiAlTa.

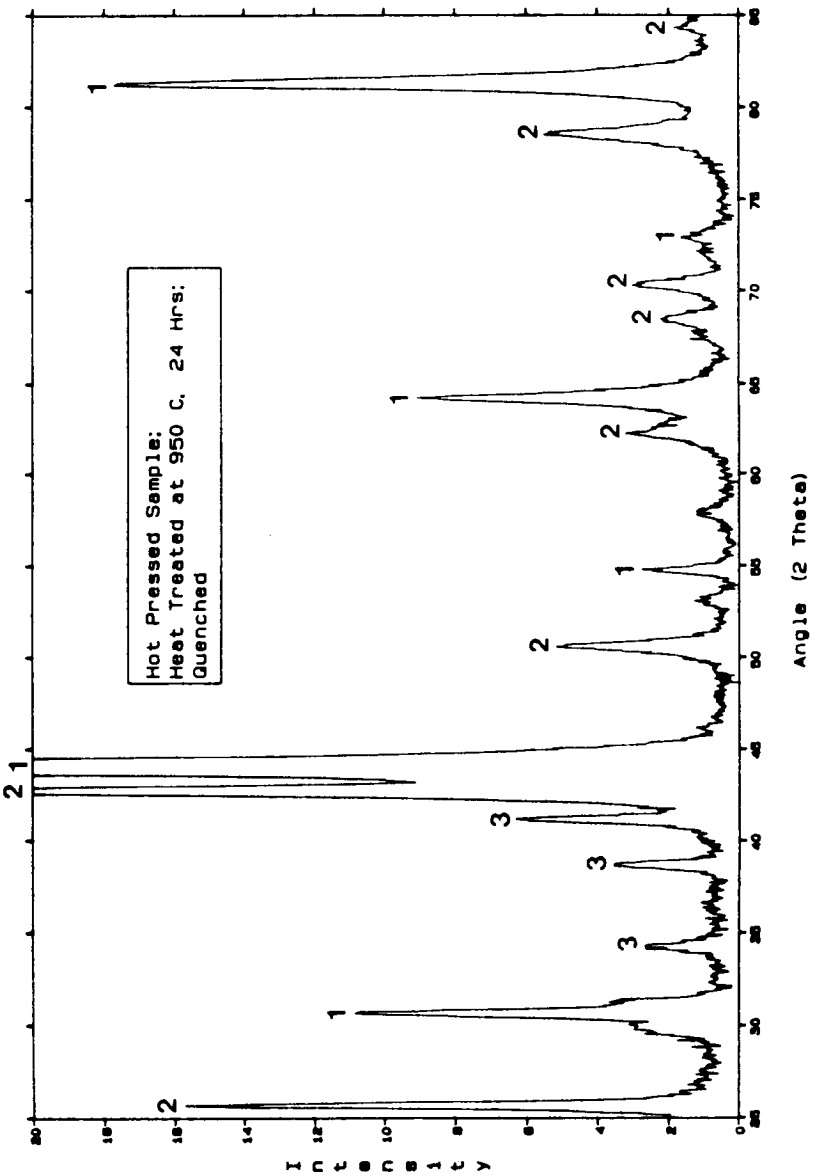

Figure 8.5 NiAl+4.5at.%Ta: VHP and annealed at $1223^{O}K$ for 24 hrs., quenched. 1 = NiAl, 2 = Ni_2AlTa, 3 = $Ta_5Ni_3Al_2$, 4 = NiAlTa.

ORIGINAL PAGE IS
OF POOR QUALITY

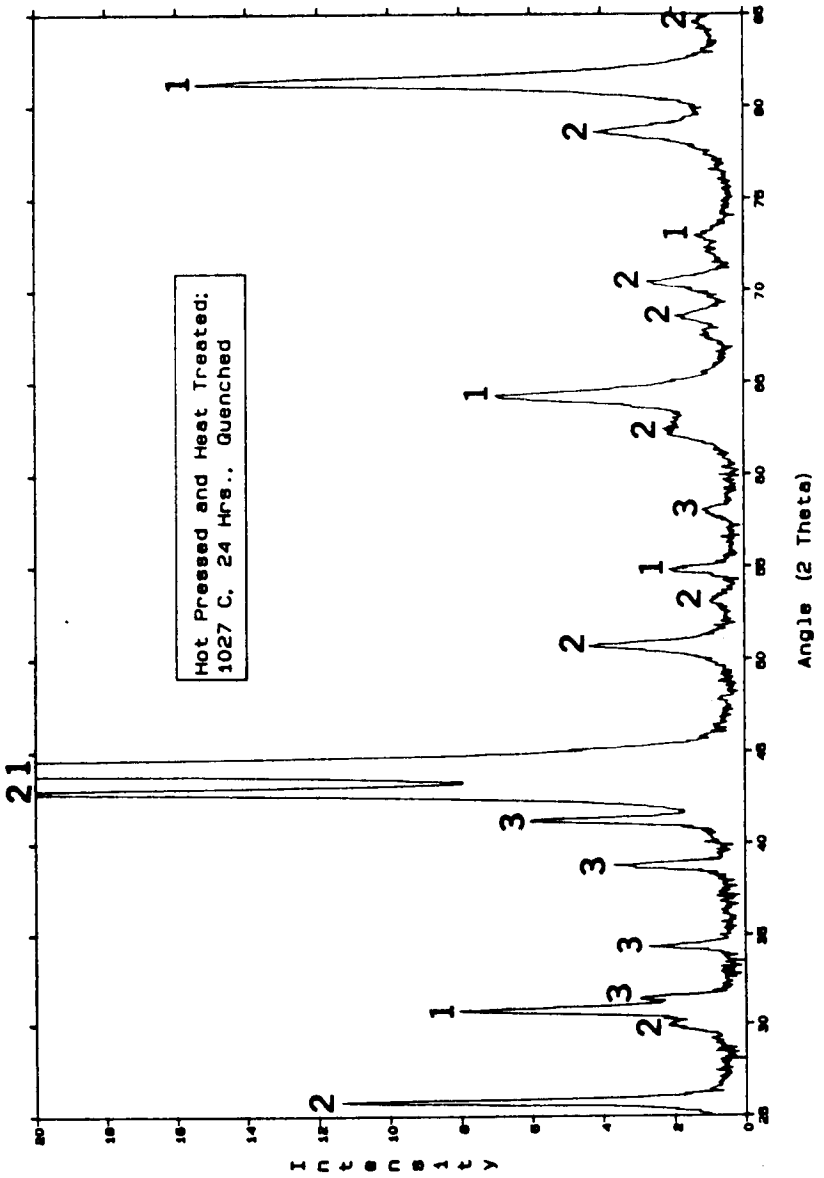

Figure 8.6 NiAl+4.5at.%Ta: VHP and annealed at 1300°K for 24 hrs., quenched. 1 = NiAl, 2 = Ni_2AlTa, 3 = $Ta_5Ni_3Al_2$, 4 = NiAlTa.

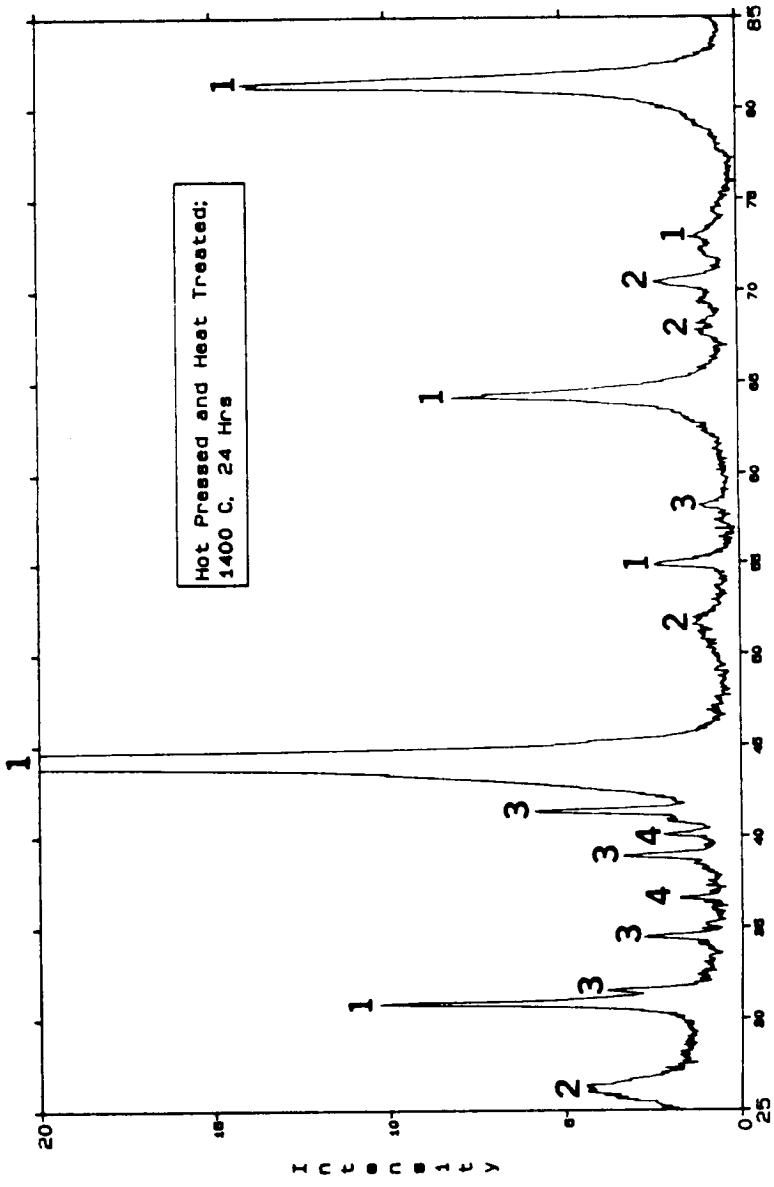

Figure 8.7 NiAl+4.5at.%Ta: VHP and annealed at $1673^{O}K$ for 24 hrs., quenched. 1 = NiAl, 2 = Ni_2AlTa, 3 = $Ta_5Ni_3Al_2$, 4 = NiAlTa.

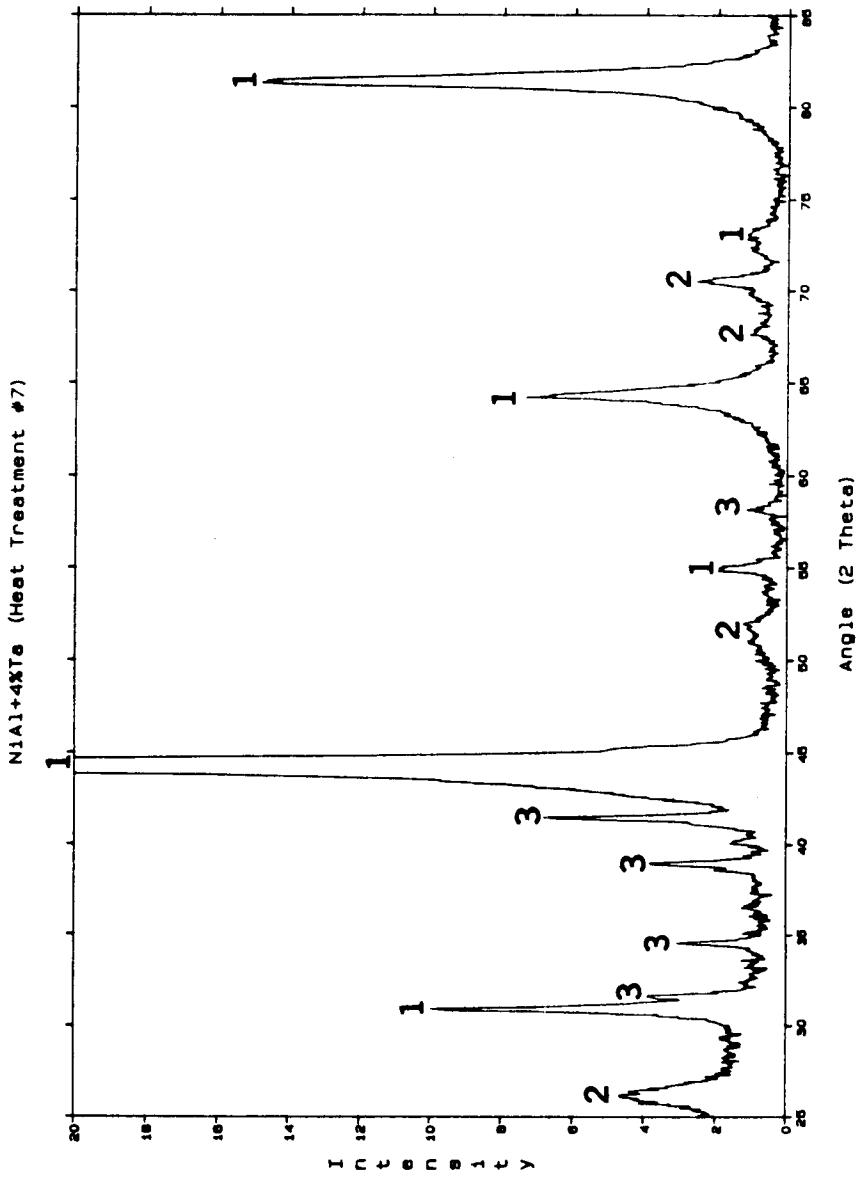

Figure 8.8 NiAl+4.5at.%Ta: VHP and annealed at 1703°K for 24 hrs., quenched. 1 = NiAl, 2 = Ni_2AlTa, 3 = $Ta_5Ni_3Al_2$, 4 = NiAlTa.

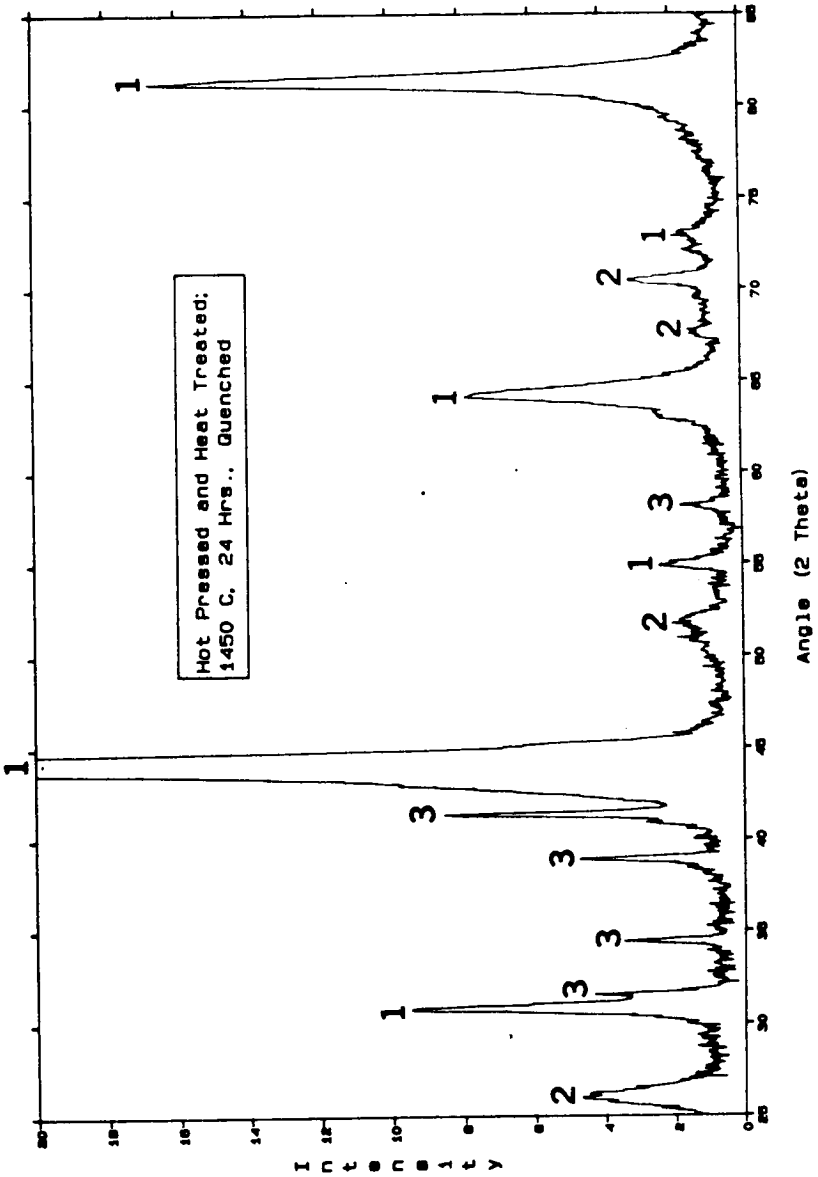

Figure 8.9 NiAl+4.5at.%Ta: VHP and annealed at 1723°K for 24 hrs., quenched. 1 = NiAl, 2 = Ni_2AlTa, 3 = $Ta_5Ni_3Al_2$, 4 = NiAlTa.

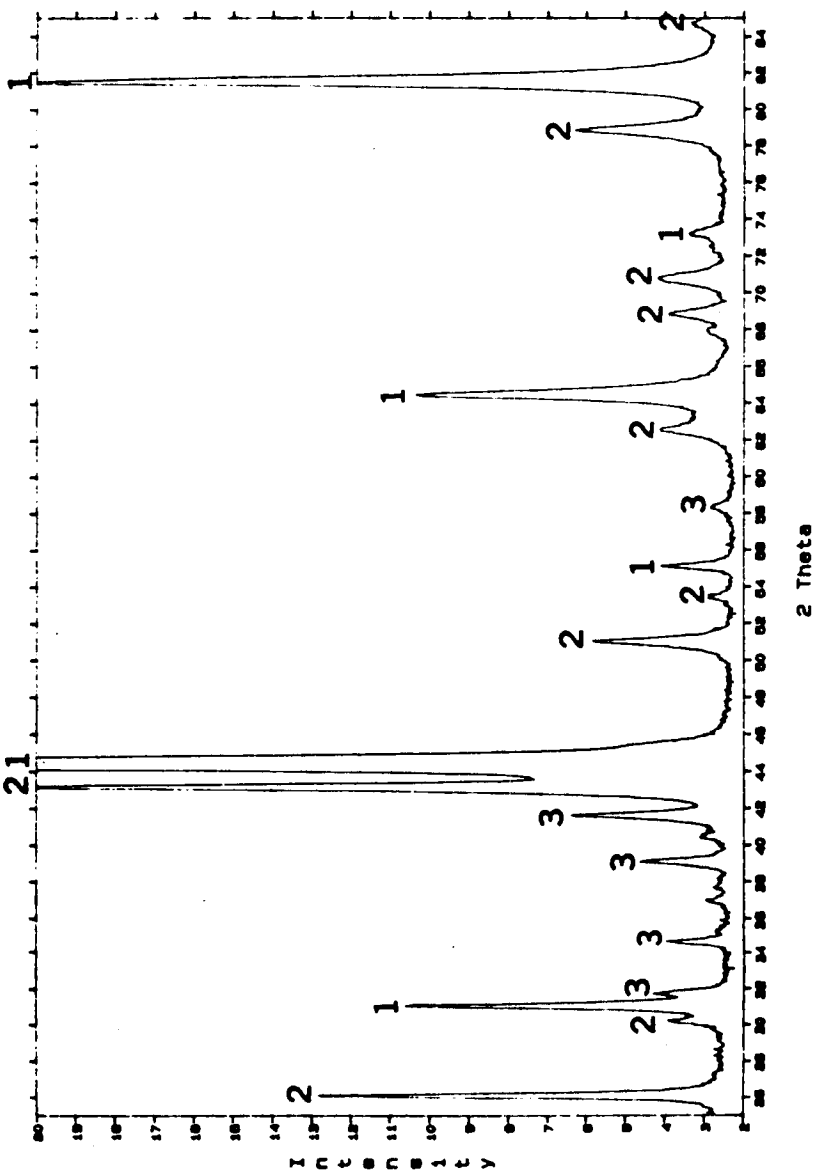

Figure 8.10 NiAl+4.5at.%Ta: VHP; annealed at 1473°K, 8 hrs., 1523°K, 24 hrs.; 1300°K, 8 hrs. 1 = NiAl, 2 = Ni_2AlTa, 3 = $Ta_5Ni_3Al_2$, 4 = NiAlTa.

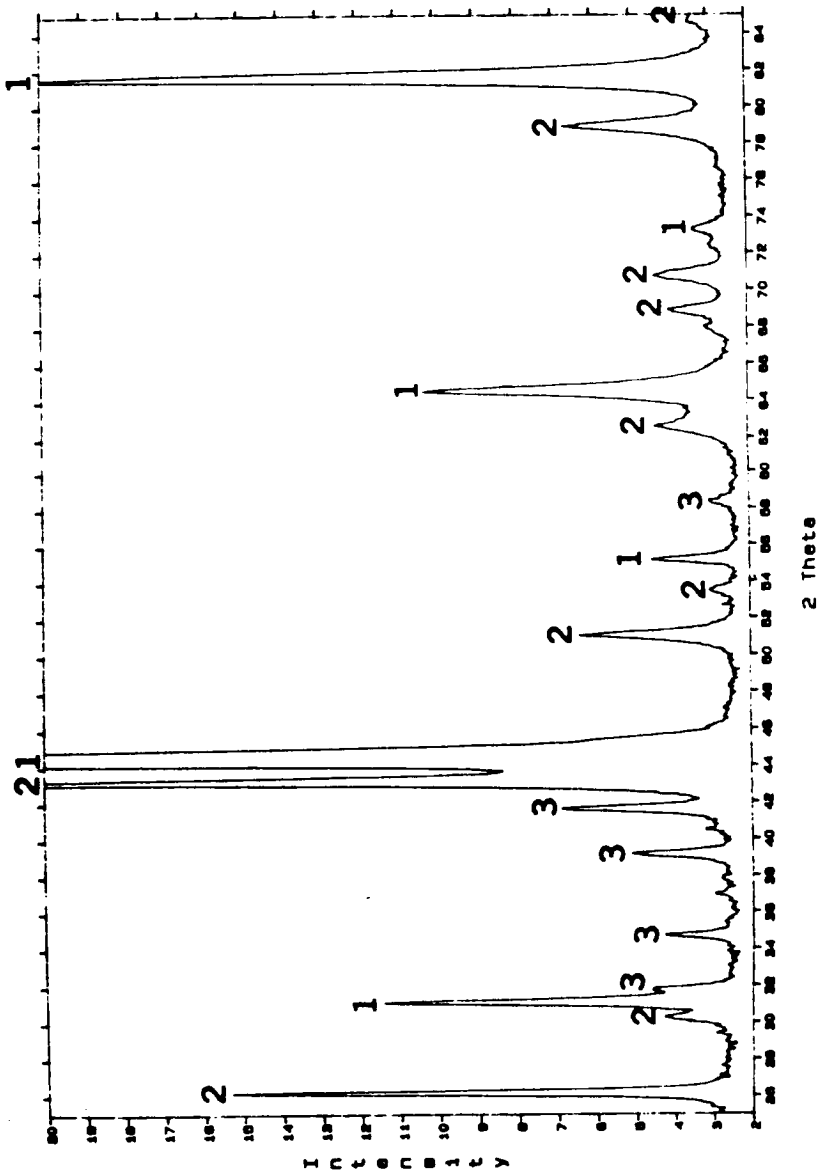

Figure 8.11 NiAl+4.5at.%Ta: VHP; annealed at 1523°K, 8 hrs., 1573°K, 24 hrs.; 1300°K, 8 hrs. 1 = NiAl, 2 = Ni_2AlTa, 3 = $Ta_5Ni_3Al_2$, 4 = NiAlTa.

ORIGINAL PAGE IS
OF POOR QUALITY

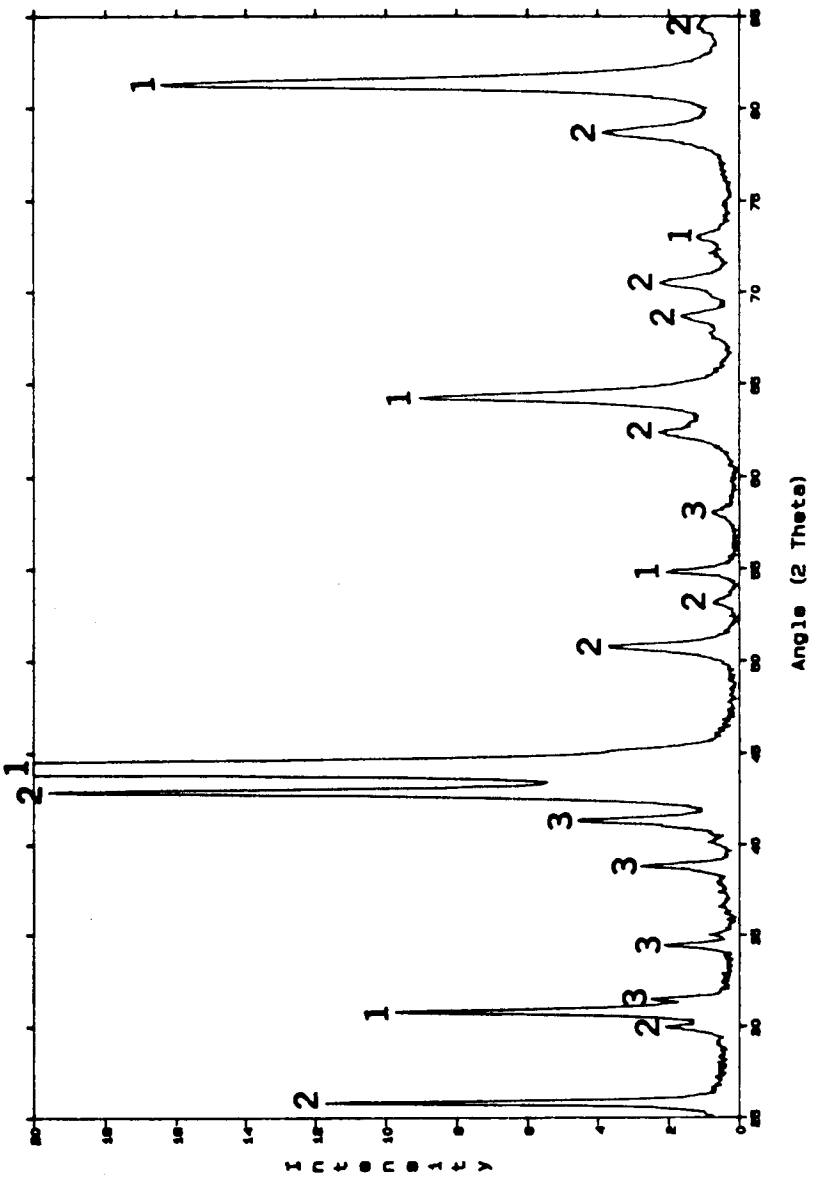

Figure 8.12 NiAl+4.5at.%Ta: VHP; annealed at $1573^{O}K$, 8 hrs., $1623^{O}K$, 24 hrs.; $1300^{O}K$, 8 hrs. 1 = NiAl, 2 = Ni_2AlTa, 3 = $Ta_5Ni_3Al_2$, 4 = NiAlTa.

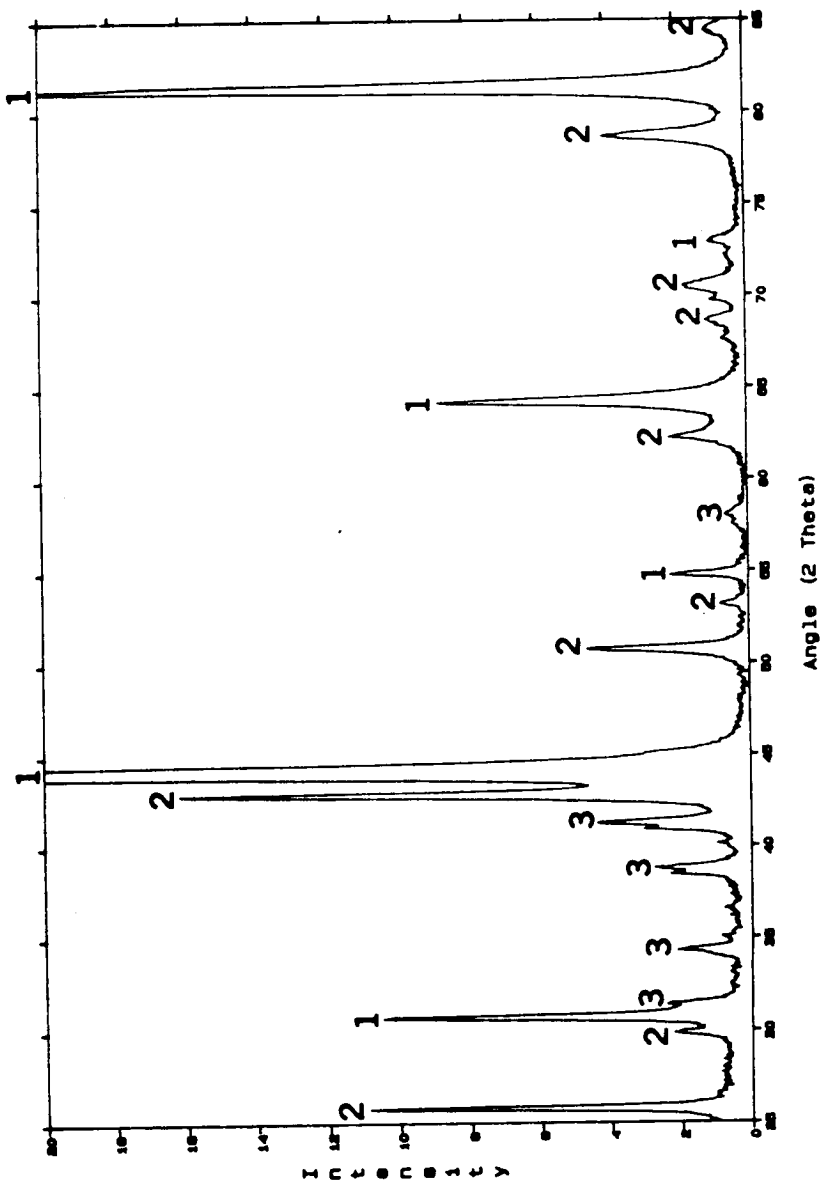

Figure 8.13 NiAl+4.5at.%Ta: VHP; annealed at $1623^{O}K$, 8 hrs.,$1673^{O}K$, 24 hrs.; $1300^{O}K$, 8 hrs. 1 = NiAl, 2 = Ni_2AlTa, 3 = $Ta_5Ni_3Al_2$, 4 = NiAlTa.

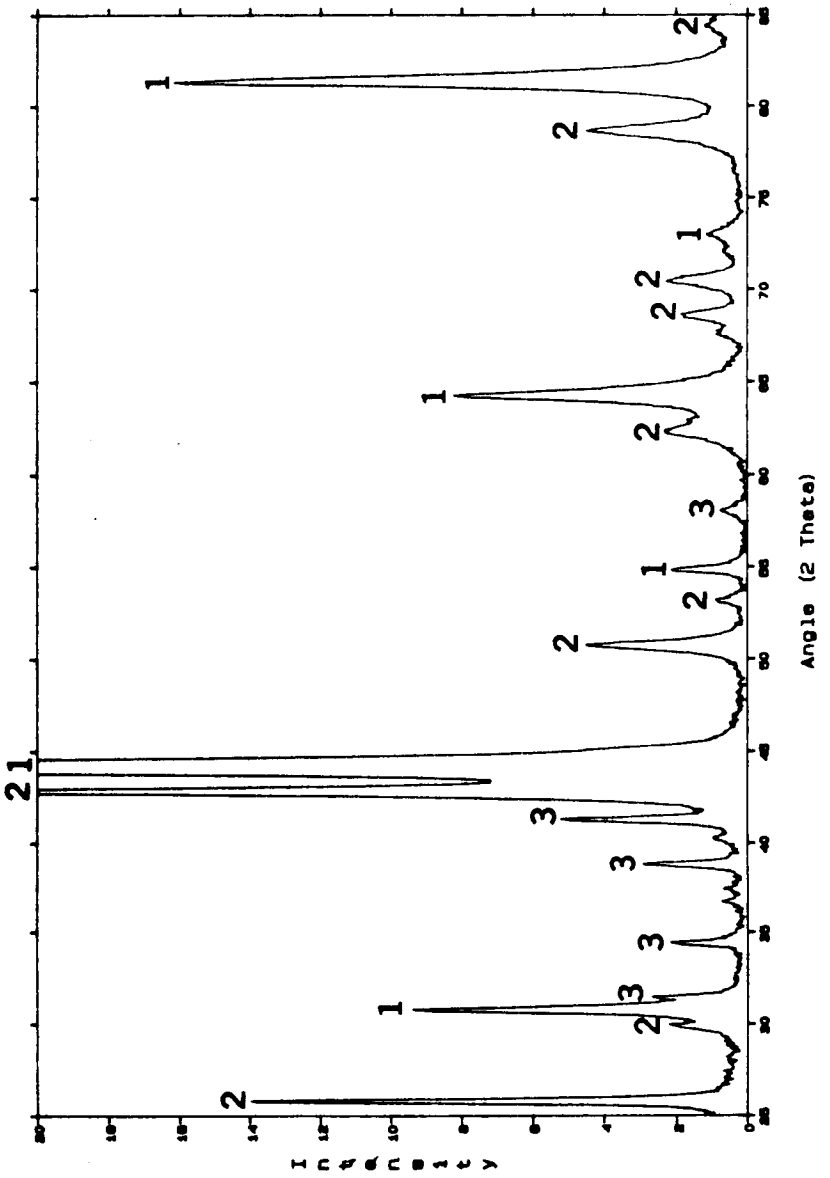

Figure 8.14 NiAl+4.5at.%Ta: VHP; annealed at 1300°K for 8 hours. 1 = NiAl, 2 = Ni_2AlTa, 3 = $Ta_5Ni_3Al_2$, 4 = NiAlTa.

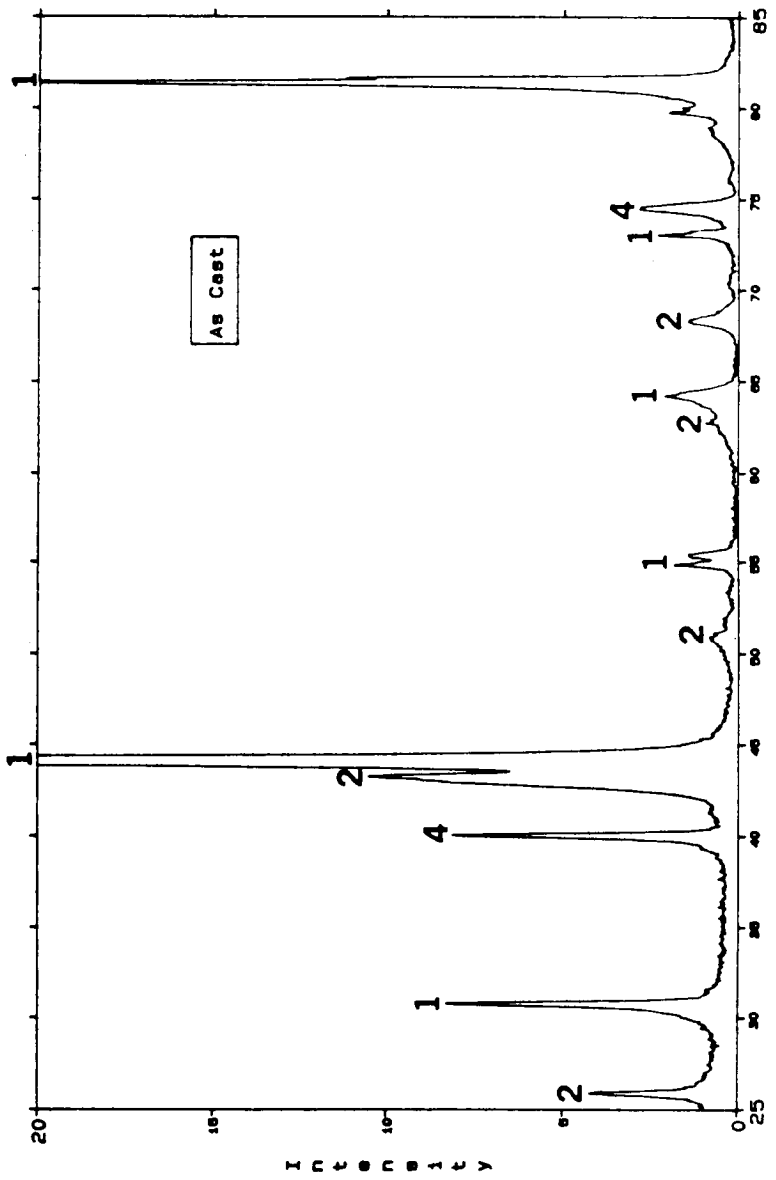

Figure 8.15 NiAl+5at.%Ta: As cast. 1 = NiAl, 2 = Ni_2AlTa, 3 = $Ta_5Ni_3Al_2$, 4 = NiAlTa.

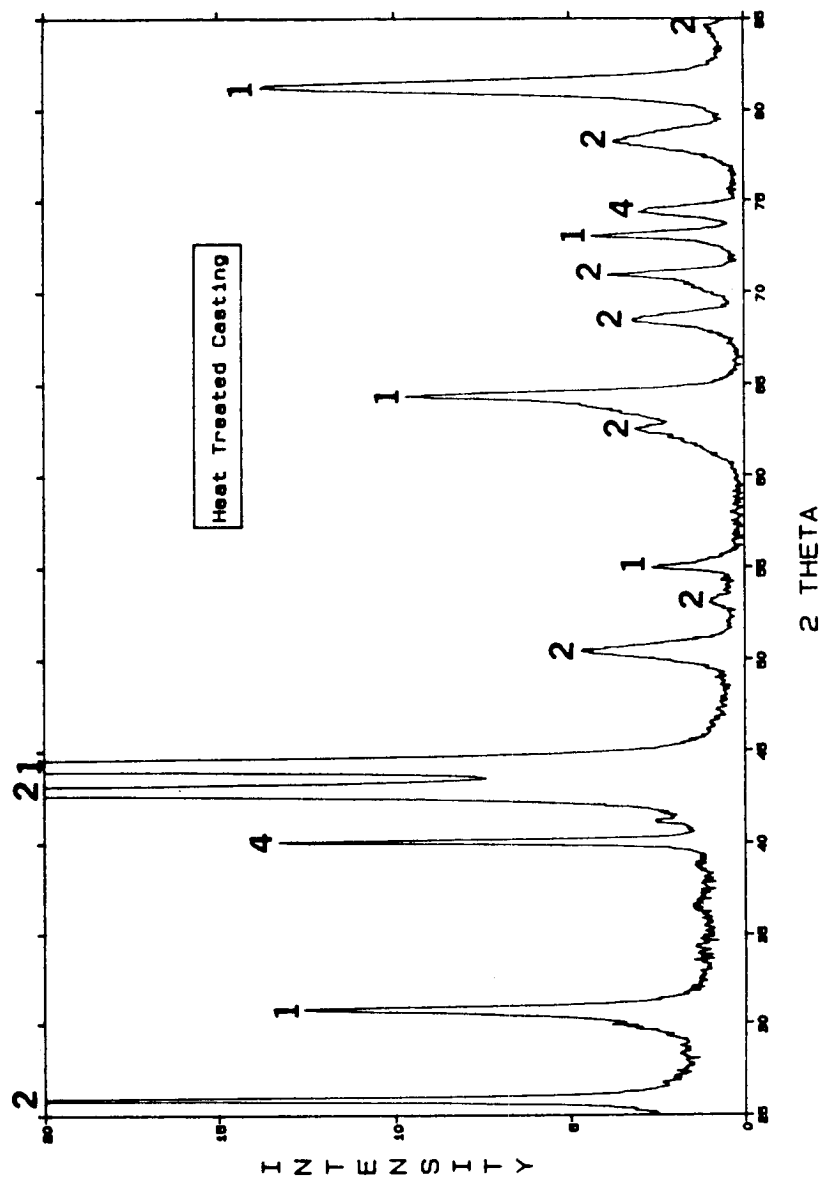

Figure 8.16 NiAl+5at.%Ta: Cast and annealed at 1623°K, 8 hrs.; 1673°K, 24 hrs.; 1300°K, 8 hrs. 1 = NiAl, 2 = Ni_2AlTa, 3 = $Ta_5Ni_3Al_2$, 4 = NiAlTa.

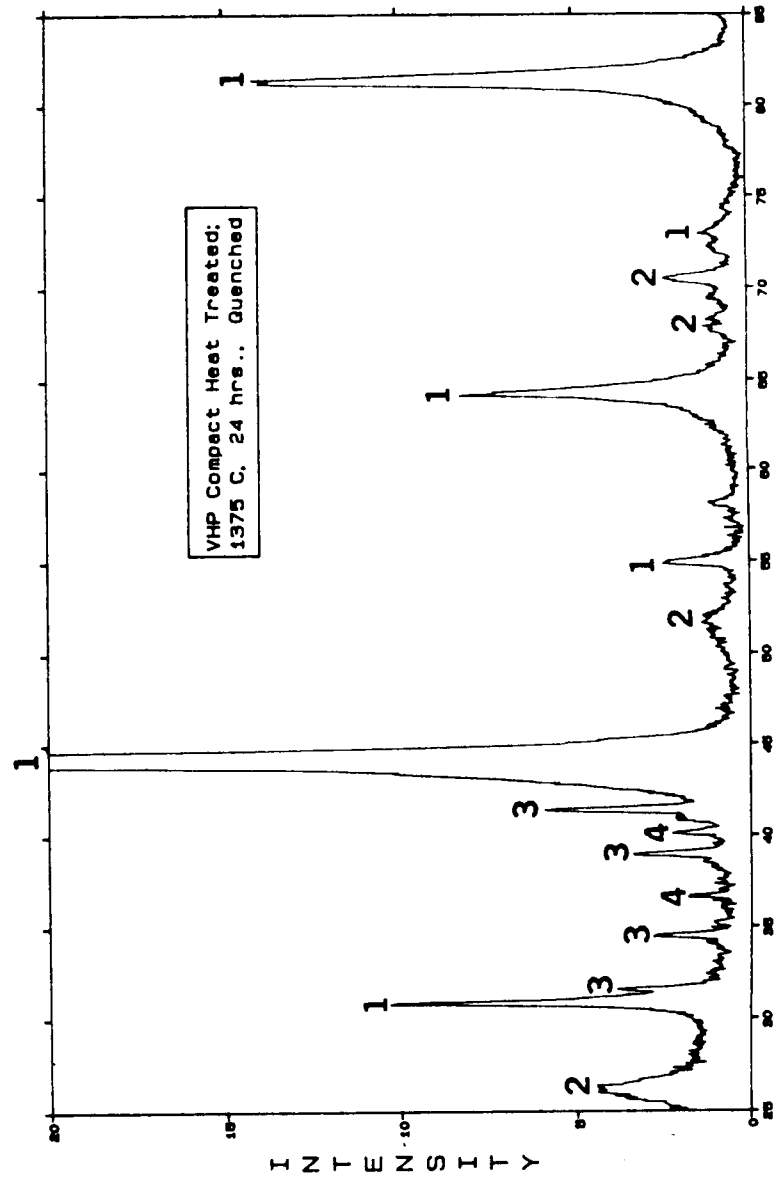

Figure 8.17 NiAl+4.5at.%Ta: VHP and annealed at $1648^{O}K$ for 24 hrs., quenched.
1 = NiAl, 2 = Ni_2AlTa, 3 = $Ta_5Ni_3Al_2$, 4 = NiAlTa.

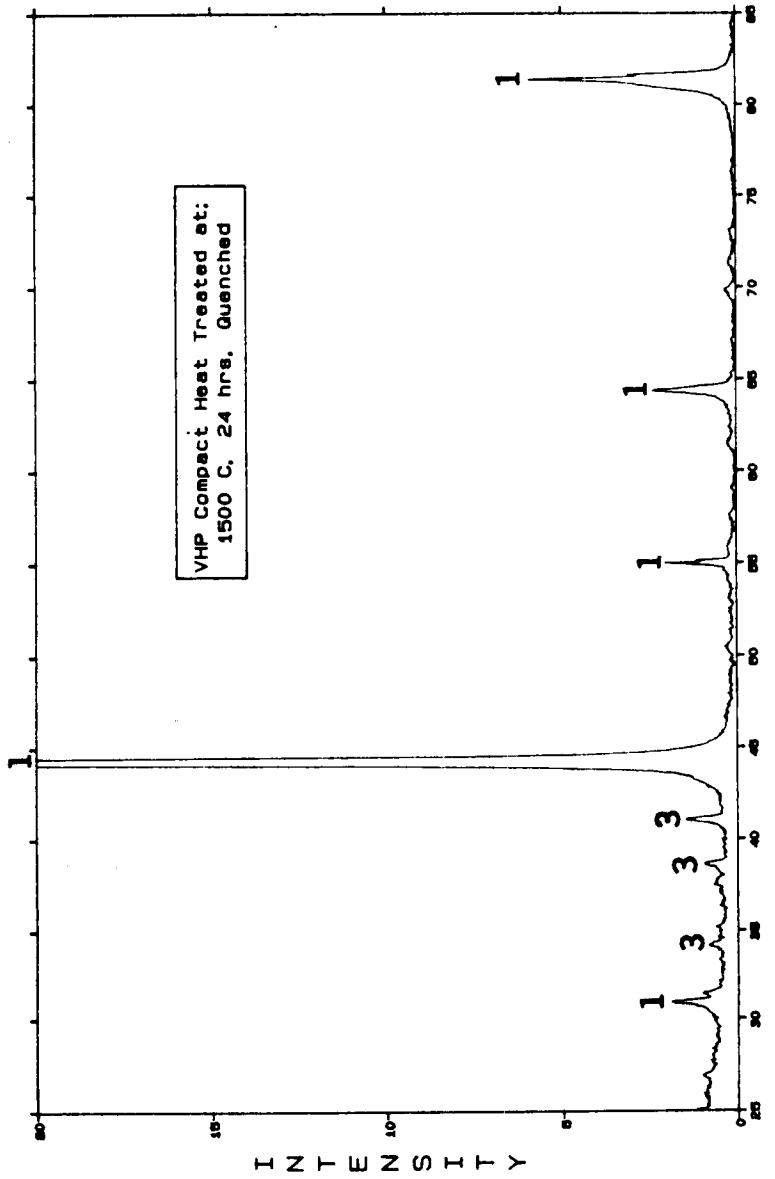

Figure 8.18 NiAl+4.5at.%Ta: VHP and annealed at 1773°K for 24 hrs., quenched.
1 = NiAl, 2 = Ni_2AlTa, 3 = $Ta_5Ni_3Al_2$, 4 = NiAlTa.

NASA
National Aeronautics and Space Administration

Report Documentation Page

1. Report No.	2. Government Accession No.	3. Recipient's Catalog No.
NASA CR-182113		

4. Title and Subtitle	5. Report Date
Processing, Physical Metallurgy and Creep of NiAl + Ta and NiAl + Nb Alloys	April 1988
	6. Performing Organization Code

7. Author(s)	8. Performing Organization Report No.
Viren M. Pathare	None
	10. Work Unit No.
	535-07-01

9. Performing Organization Name and Address	11. Contract or Grant No.
Case Western Reserve University Dept. of Materials Science and Engineering Cleveland, Ohio 44106	NAG3-387
	13. Type of Report and Period Covered Contractor Report Final

12. Sponsoring Agency Name and Address	14. Sponsoring Agency Code
National Aeronautics and Space Administration Lewis Research Center Cleveland, Ohio 44135-3191	

15. Supplementary Notes

Project Manager, Michael V. Nathal, Materials Division, NASA Lewis Research Center. This report was a thesis submitted in partial fulfillment of the requirements for the Degree of Doctor of Philosophy to Case Western Reserve University in January 1988.

16. Abstract

Powder processed NiAl + Ta alloys containing 1, 2, and 4.5 at % tantalum and NiAl + Nb alloys containing 1 and 2 at % niobium were developed for improved creep properties. In addition, a cast alloy with 5 at % tantalum was also studied. Hot extrusion parameters for processing alloys with 1 and 2 at % of tantalum or niobium were designed. NiAl + 4.5 at % Ta alloy could be vacuum hot pressed successfully, even though it could not be extruded. All the phases in the multiphase alloys were identified and the phase transformations studied. Ni_2AlTa in NiAl + 4.5 at % Ta alloy transforms into a liquid phase above 1700 K. Solutionizing and annealing below this temperature gives rise to a uniform distribution of fine second phase precipitates. Compressive creep properties were evaluated at 1300 K using constant load and constant velosity tests. In the higher strain rate region single phase NiAl + 1 at % Ta and NiAl + 1 at % Nb alloys exhibit a stress exponent of 5 characteristic of climb controlled dislocation creep. In slower strain rate regime diffusional creep becomes important. The two phase alloys containing 2 to 5 at % Ta and 2 at % Nb show considerable improvement over binary NiAl and single phase alloys. Loose dislocation networks and tangles stabilized by the precipitates were found in the as crept microstructure. The cast alloy which has larger grains and a distribution of fine precipitates shows the maximum improvement over binary NiAl.

17. Key Words (Suggested by Author(s))	18. Distribution Statement
Creep; Intermetallics; Nickel-aluminide; Powder metallurgy; Processing; Electron microscopy	Unclassified - Unlimited Subject Category 26

19. Security Classif. (of this report)	20. Security Classif. (of this page)	21. No of pages	22. Price*
Unclassified	Unclassified	189	A09

*For sale by the National Technical Information Service, Springfield, Virginia 22161